# STRESS CORROSION CRACK INITIATION OF ALLOY 600 IN SIMULATED PWR PRIMARY WATER

**Technical Milestone Report: M2LW-17OR0402034**
**September 2017**

Z. Zhai, M. B. Toloczko, M. J. Olszta, D. K. Schreiber and S. M. Bruemmer
Pacific Northwest National Laboratory

Research Project:
**Stress Corrosion Crack Initiation of**
**Nickel-Base Alloys in LWR Environments**
Project Manager:  S. M. Bruemmer
Pacific Northwest National Laboratory

Conducted for:
**Office of Nuclear Energy, U.S. Department of Energy**
**Light Water Reactor Sustainability Program**
**Materials Aging and Degradation Pathway**
Pathway Manager:  K. J. Leonard
Oak Ridge National Laboratory

**Table of Contents**

**Project Background**

*Objective*

This research project addresses one of the least understood aspects of stress corrosion cracking (SCC) for light-water reactor (LWR) pressure boundary components - crack initiation. The focus of the work is to investigate important material (composition, processing, microstructure, strength) and environmental (temperature, water chemistry, electrochemical potential, stress) effects on the SCC susceptibility of corrosion-resistant, nickel-base alloys. The primary objectives are to identify mechanisms controlling crack nucleation, investigate the transition from short to long crack growth in these alloys under realistic LWR conditions and help establish the framework to effectively model and mitigate SCC initiation processes.

*Approach*

Alloy 600 materials were selected for the first phase of SCC initiation experimentation followed by testing on the more resistant alloy 690 materials. For both alloys, material variants known to influence SCC response are being examined including cold/warm work (forged, rolled and tensile strained), banded/inhomogeneous microstructures (plate versus extruded tubing), grain boundary precipitation (heat-to-heat variations, mill-annealed, solution annealing and changes due to thermal treatments) and surface grinding (various damage depths, surface roughness and nanocrystalline layers). Materials and material conditions have been identified and obtained from ongoing research projects where stress-corrosion crack growth has been characterized, thus creating an important link between SCC initiation and propagation behavior. Detailed examinations have been performed using optical and electron microscopy to establish key bulk and surface microstructural features that may act as initiation precursors. Dedicated test systems with continuous in-situ detection of crack formation were designed and constructed enabling SCC initiation experimentation of a range of alloy 600 and 690 materials. After SCC testing in high temperature autoclave systems, surface and near-surface characterizations were conducted to document nano-to-microscale initiation precursors leading to macroscopic stress corrosion cracks. The fundamental understanding of how the near-surface microstructure is degraded during high-temperature water exposure is essential to an improved predictive methodology for SCC initiation.

*Focus of Current Report*

This report reviews recent SCC initiation testing on cold-worked (CW) alloy 600 specimens from several different heats in high-temperature, simulated PWR primary water. It follows earlier milestone reports [1-5] that described our previous SCC initiation tests and corrosion-structure characterizations on alloy 600 and alloy 690 materials. While previous work on alloy

4

600 has established baseline responses for as-received and CW specimens at constant load and elucidate the fidelity of in-situ direct current potential drop (DCPD) detection capability, the current report provides new insights on the effect of microstructure and temperature on SCC initiation response of alloy 600 materials. Unexpected short SCC initiation times were obtained for a solution-annealed (SA) plate heat with high B and low C contents in the bulk and significant B segregation at grain boundaries. Large scatter in measured SCC initiation times was observed for one of our baseline plate heats in the mill-annealed (MA) condition. Twelve specimens with similar cold work levels were tested at constant load to evaluate this behavior and only three showed much shorter SCC initiation times (<400 hours) than the nine others (>1200 hours). Post-test examinations revealed that the inhomogeneous, banded microstructure in this material appears to promote differences in SCC initiation response. Early crack initiation was found to preferentially occur at sporadic large elongated grains in the banded plate especially when protruded deep into the specimen gauge. In addition, testing in simulated PWR primary water was performed at several temperatures on two CW alloy 600 materials to determine the thermal activation energy for SCC initiation. These results enable more effective lab-to-lab comparisons to be made and will lead to improved predictions of behavior in PWR primary water systems. In order to put the new alloy 600 research in perspective, the experimental approach used at PNNL is briefly reviewed along with key prior SCC measurements on alloy 600 materials.

**SCC Initiation Test Systems and Testing Approach**

*Specimens*

Specimen Design

A key goal for this program is to correlate SCC initiation time to various aspects of materials processing including bulk microstructure, near surface microstructure, surface texture, existence of surface defects and applied stress level. Prior experience with alloys 600 and 690 has shown that their SCC crack growth resistance is extremely sensitive to the degree of plastic deformation, and therefore accurate characterization in the test specimen was an important factor in the specimen design. Several different specimen types were considered for the crack initiation testing including U-bend, bent beam, tensile, and blunt-notch compact tension (CT) geometries.

Ultimately, a tensile specimen geometry was the most attractive because it has none of the shortcomings associated with U-bend, bent beam and blunt-notch specimens. This design produces a uniaxial stress state, the gauge region is accessible allowing control over the surface microstructure, various types of micro/macroscopic defects can be generated and there are several ways to produce specimens with well-known amounts of uniform plastic strain. In addition, prior work at KAPL [6] has shown that DCPD can be effectively used to detect crack initiation. Several factors played into the specific design of the tensile specimens employed for SCC initiation testing [3], the most important was maximizing the ability of DCPD to detect crack initiation. The DCPD signal is affected not only by crack growth, but also by elastic and plastic strains including creep. Initiation tests are typically conducted at or near the yield stress where small amounts of creep occur at PWR primary water temperatures. To reduce the magnitude of the creep contribution to the DCPD signal, the gauge length was kept as short as possible while allowing a sufficient number of grain boundaries to be exposed. The short gauge length also played favorably for the desire to be able to fully survey the specimen gauge surface for cracks by scanning electron microscopy (SEM) in a reasonable length of time. This characterization is critically important to assess precursors to large crack formation and the transitions from intergranular attack (IGA) to micro-crack nucleation to short crack growth mechanisms. In addition, one practical issue was the desire to have an initiation specimen size that fit within the dimensions of a 0.5T CT specimen such that any material prepared for SCC crack growth studies could also be used for SCC crack initiation studies. The final tensile design was refined to the point that a crack initiation specimen could be cut from an SCC-tested 0.5T CT specimen as long the crack length to width ratio (a/W) in the CT specimen did not exceed 0.7. This a/W is below the range of typical crack lengths in SCC studies conducted by PNNL allowing routine extraction of crack initiation specimens as desired. Other factors for the design were the need to electrically isolate the specimen and eliminate any significant stress risers.

The effect of resistivity change on the DCPD signal for nickel-base alloys exposed to PWR relevant temperatures was measured and subtracted from the gauge signal. This was accomplished by monitoring a larger diameter region of the specimen where the stress is approximately 15% of the gauge stress (depending on gauge diameter). For this low stress region, neither crack initiation nor any substantial amount of creep will occur and the inherent resistivity change of the material can be measured. The specimen dimensions along with a photo of the specimen are shown in Figure 1. After taking into account all design considerations, a 30.5 mm tall tensile specimen with a 4.0 mm gauge length was selected.
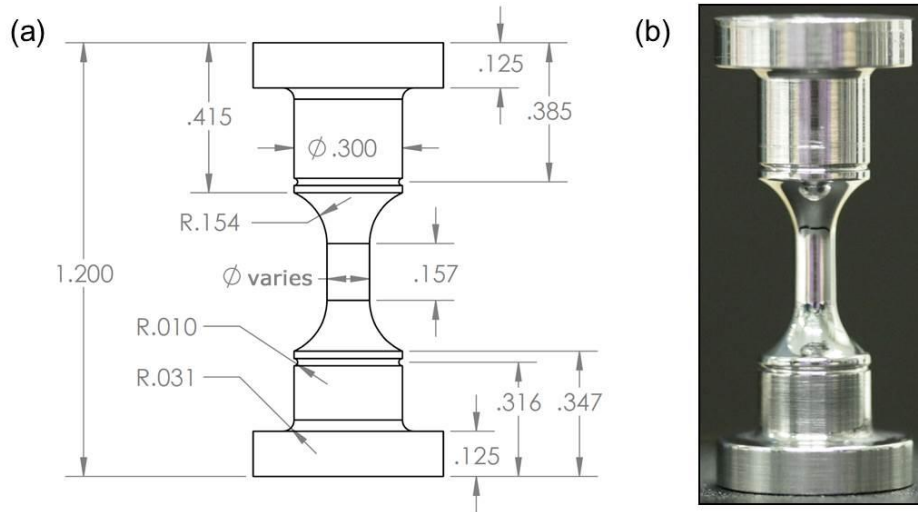


Figure 1. PNNL initiation specimen design. Gauge diameter is selected based on material strength and can be varied from 2.75-4.5 mm and the gauge length is 4.0 mm. Overall height is 30.5 mm (1.2 inches).

Specimen Preparation

Materials were tested in either the as-received (AR) or a CW condition. Cold working was achieved either by cold tensile straining (CTS), cold rolling (CR) or cold forging (CF). Cold rolling performed on the plate material was done such that the rolling direction was the same direction as the original plate processing direction. Specimens taken from CRDM tubing were cut with the gauge axis parallel to the CRDM tubing axis. The gauge axis of specimens cut from the plate material was parallel to the "S" direction relative to the plate processing. Prior to insertion of the specimens into the autoclave, the gauge section either was polished to a 1 μm finish or was rough ground. A "C" finish used for some of the specimens attempts to emulate the surface damage layer created by typical service component grinding operations [7]. Application of the surface damage was achieved by applying various grinding tools to the gauge section while rotating the specimens in a lathe. Grinding tools that have been used include wood-backed sandpaper of various grits and a rotary tool with different roughness grinding disks. In order to obtain the 1 μm finish, pieces of gradually finer SiC paper (400 to 600 grit) was used followed

by polishing cloth (on which 6 μm then 1 μm diamond paste was evenly spread) with a width a little wider than specimen gauge length was firmly adhered to a wooden stick.  This tool was then moved systematically with a controlled load applied by hand across the gauge section with the specimen spinning at 200 revolutions per minute on a lathe.  Each grinding or polishing step normally lasted 30 s to 2 min while lubricant oil was dripped onto the tool whenever necessary.  After each step, the specimen was rinsed in dish soap water and then the gauge surface was checked using an optical stereoscope.  Upon completion, the specimen was sonicated twice in dish soap water, once in 2% ethanol and then dried.  SEM surface and cross-section observations of the 1-μm finish and the 60-grit finish applied to a CW material are shown in Figures 2 and 3, respectively.
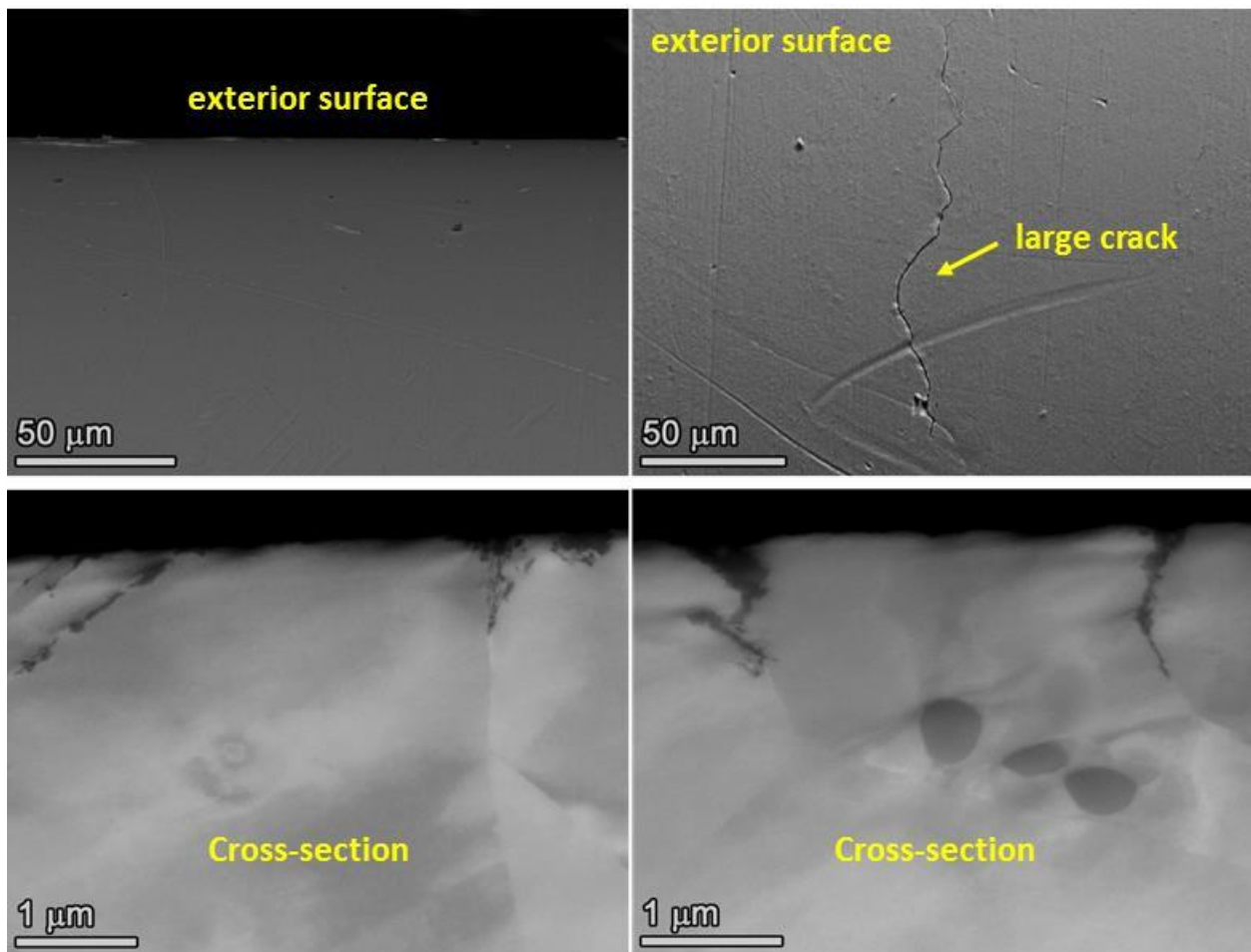


Figure 2.  SEM-SE images showing the surface (upper) and BSE images showing the cross-section (lower) of a 1 μm finish plate specimen after exposure.
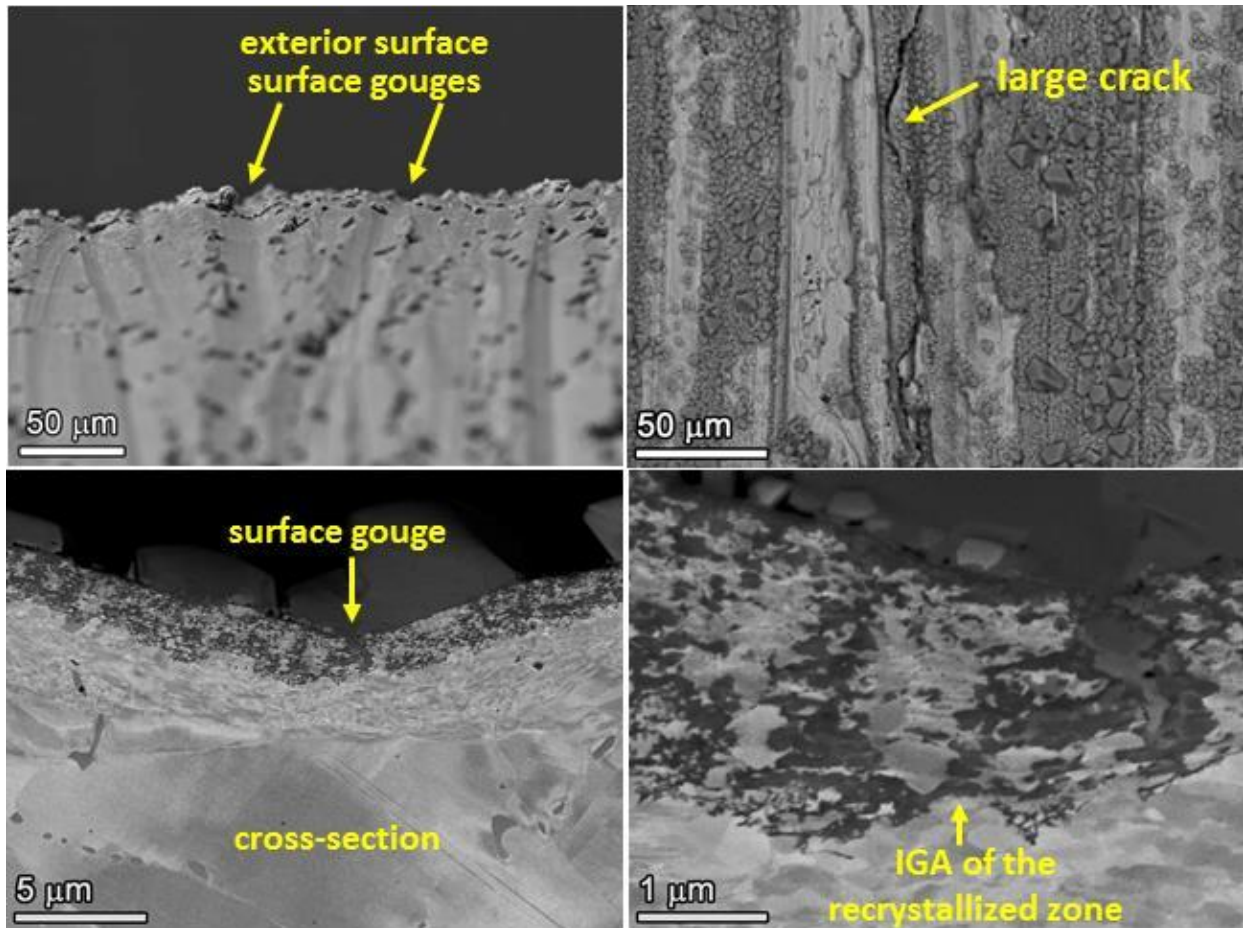
Figure 3. SEM-SE (upper) and BSE (lower) images showing the surface and cross-section of a 60 grit finish plate specimen after exposure.

Generally, aggressive grinding produces a nanocrystalline layer (Figure 3) that promotes corrosion across the entire surface and delays water access to bulk grain boundaries. This has been found to have a small effect on initiation times as will be discussed later. In comparison, a highly polished surface ensures that all grain boundaries reaching the surface are immediately exposed to water. From a testing perspective, a ground surface impairs observation of surface cracks due to the rough surface and microscale fold-overs that often have a crack-like appearance. A polished surface eliminates these complicating factors and enables a better optical and SEM assessment of IGA and crack nucleation as a function of the material, environment and test conditions.

*SCC Initiation Test Systems*

Test systems have been built to allow in-situ monitoring of crack initiation in an environment that provides a high degree of control over load (stress), water temperature and water chemistry including B/Li content, dissolved gas content and impurity content. These test systems are very

similar in design to systems built at PNNL to measure SCC crack growth of LWR pressure boundary component materials [8, 9].

The key components of these test systems are: (1) a servo-electric load control system capable of maintaining a stable constant load for very long periods of time and capable of providing a wide range of cyclic loading conditions, (2) a recirculating water system that that is used to control water chemistry, (3) an autoclave for specimen exposure at high temperatures and pressures, (4) a DCPD system for in-situ monitoring of crack initiation, and (5) a continuous data acquisition system. Careful consideration went into design and equipment selection to optimize control of all system variables. Some of the most important optimizations were to: (1) use wetted components that release no contamination into the water, (2) have a sufficiently high water flow rate through the autoclave to maintain the target chemistry, (3) maintain uniform temperature and pressure at the specimens, (4) obtain highly accurate measurements of the test environment (temperature, conductivity, pH, load, dissolved gas content), and (5) create a sensitive DCPD-based crack initiation detection system. Each of the subsystems will be discussed in further detail below.

The water flow system is comprised of low- and high-pressure loops as shown in Figure 4. The purpose of the low-pressure loop is to control dissolved gas content and impurity level by flowing water through a column where selected gases and ionic impurities are dissolved or injected into the water. A side stream of this mixing loop feeds the high-pressure loop. The large pressure pulses and flow surges created by the piston pump are dampened with pulsation dampers at the inlet and outlet of the pump. The high-pressure water flows into a regenerative heat exchanger where hot water leaving the autoclave preheats the incoming water. Just prior to entering the autoclave, the incoming partially heated water is brought up to test temperature using a preheater. After the water flows through the heated autoclave, it travels back through the regenerative heat exchanger and then through a water cooler that brings the water back down to room temperature. The cooled water then passes through a back-pressure regulator and emerges at ~0.07 MPa (10 psi) of pressure. The water runs through a flow meter, a conductivity sensor, a mixed resin bed demineralizer, and is dumped back into the low-pressure mixing loop.

B and Li levels for PWR primary water testing are controlled by pre-saturating the mixed resin bed demineralizer with boric acid and Li hydroxide to specific levels that will result in tailored, near-constant B and Li content. Some drift in the Li level in the water is expected because it is singly ionized and is easily displaced from the demineralizer by more highly positively ionized species (e.g., chromate) coming off the autoclave. To account for this, displaced Li is removed by periodic partial replacement of water in the mixing loop with water having little or no Li (and some B). Levels for B and Li in the mixing loop are determined from measurements of water conductivity, pH and temperature. Water flow through the autoclave is maintained at ~125 cc/min to provide a consistent chemistry environment.
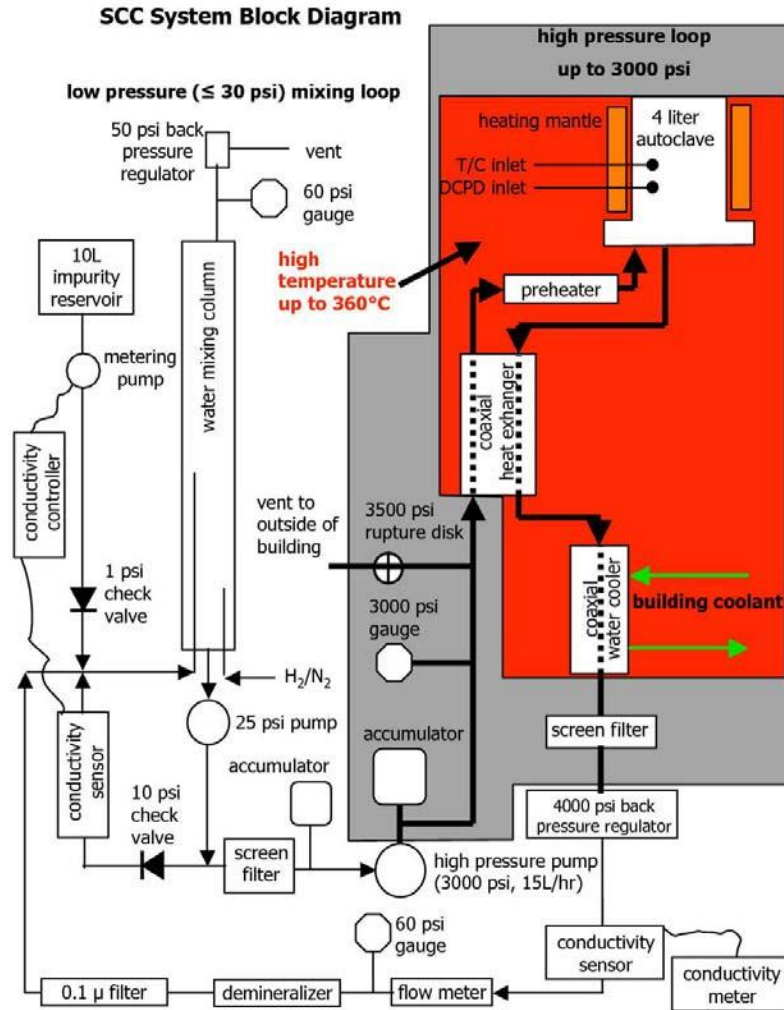
10

Figure 4.  General water flow diagram for PNNL SCC crack-growth and initiation test systems.

Figure 5 shows the load train and DCPD instrumentation for the typical SCC initiation specimen set up at PNNL.  Currently two small SCC initiation systems and one large SCC initiation system are being used under the scope of LWRS.  The two small SCC initiation systems have been converted to test up to 6 fully instrumented specimens during the past year, and the large SCC initiation system allows 36 specimens be tested simultaneously with up to 12 specimens instrumented.  The load frame in both types of systems are designed to sustain the load even when certain specimens fractured during the test to allow the test to continue for the other specimens loaded in the same string.  To make this possible, the controlling software is programed to partially unload the system when a sharp strain increase in an individual specimen is detected by DCPD.  The load decrease (typically to ~80% of the starting value) enables the SCC-initiated tensile specimen to fail safely without significantly impacting the entire system. After the failure of the specimen is confirmed (usually by losing DCPD signal), the load is brought back to yield stress again while monitoring stress versus strain curve using DCPD for every specimen.
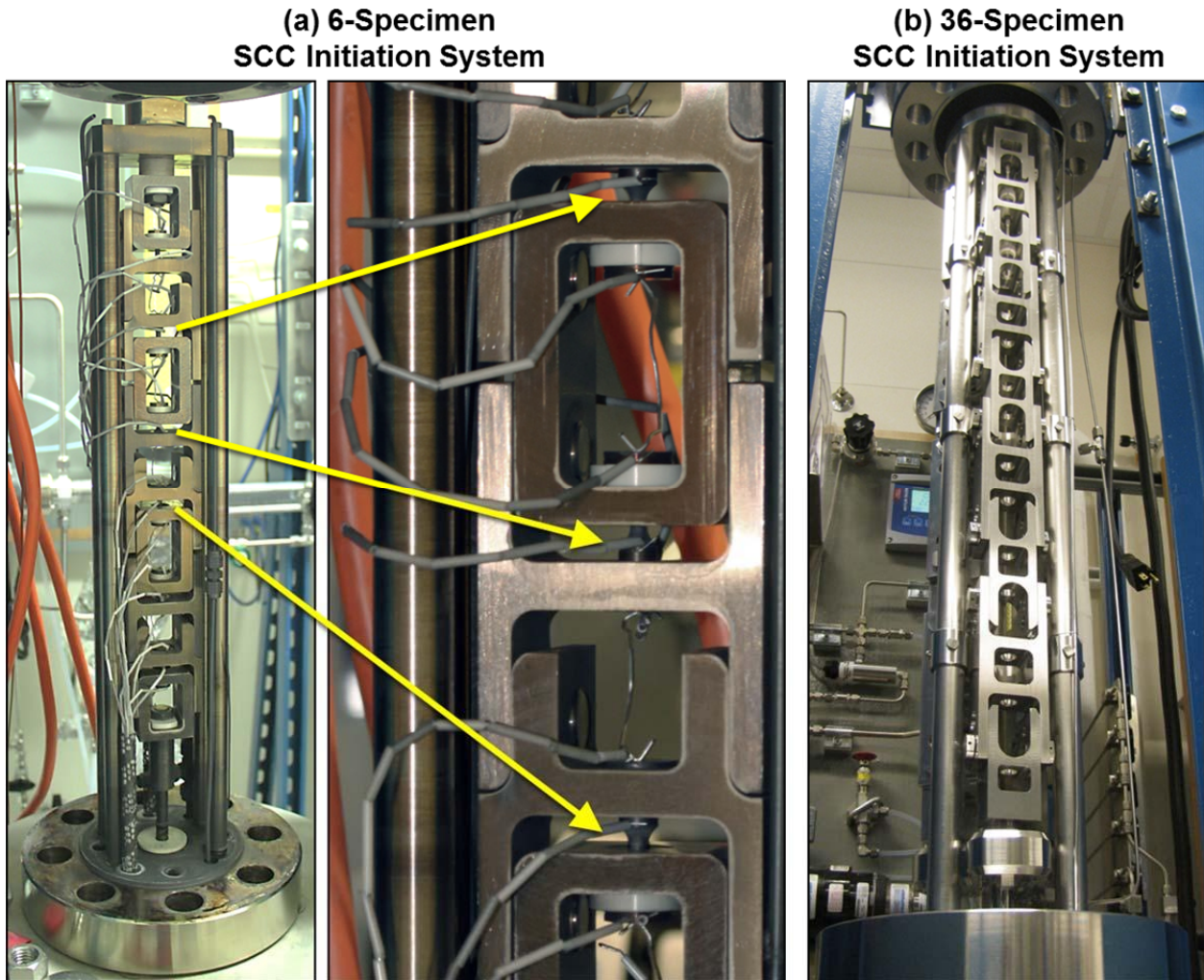
Figure 5. Crack initiation test system load train at PNNL in the (a) small SCC initiation test system with capacity of testing up to 6 fully instrumented specimens and the (b) large SCC initiation test system with capacity of testing up to 24 instrumented specimens and up to 36 specimens in total.

*In-situ DCPD measurement*

PNNL uses a reversing DCPD system developed by Peter Andresen formally with General Electric (GE) Global Research. As with all DCPD measurement systems, a constant current is run through the sample. However, by using a solid-state polarity-reversing switch built into the current path, potential drop is measured in both a forward and reverse current flow condition. By measuring the average of the voltage in the forward and reverse current conditions, contact voltages are eliminated from the measurement. Finite element modeling (FEM) was used to visualize the voltage distribution in the interior of the specimen and on the surface. Wire attachment positions were selected at regions where voltage was relatively uniform on the surface, thus making it relatively easy to remove and reinsert specimens for testing without

significantly changing the DCPD voltage values. Figure 6 shows the ideal voltage measurement points on the specimen. As noted in the figure, voltage is monitored across both the gauge region and a reference region with a larger diameter where stresses are much lower. The gauge voltage is sensitive to multiple phenomena including cracking, elastic and plastic strain, and resistivity evolution of the material while the voltage across the reference region will be primarily sensitive to resistivity evolution and a smaller amount of creep. This reference measurement is used to subtract out resistivity drift from the gauge voltage signal, leaving only cracking and some creep strain as contributions to the measured specimen response. While cracking and creep are both likely to be simultaneously contributing to the gauge DCPD response, the data here are presented as creep strains because it is thought that up to the point of SCC initiation, the DCPD signal will be predominantly affected by creep and any strong deviation in response from the creep strain trajectory will likely be due to crack initiation and growth.
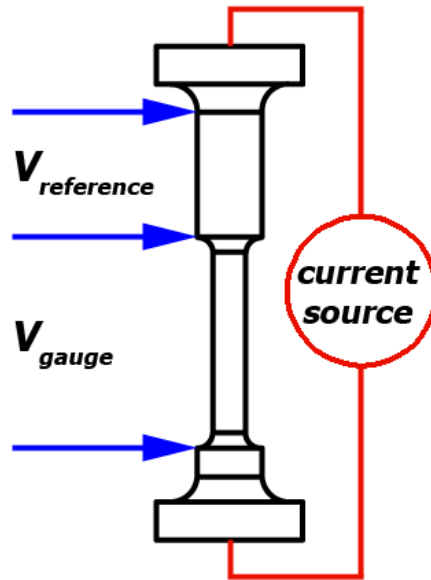


Figure 6. Sketch of the tensile specimen showing desired DCPD measurement points.

A formula for strain as a function of voltage starts first with the dependence of voltage on gauge dimensions:

$$V = \rho(L/A) \cdot I \qquad (1)$$

$V$ is the measured voltage, $\rho$ is the material resistivity, $L$ is the distance between measurement points, and A is the cross-sectional area and $I$ is the applied current. Because plastic strain (including creep) is volume conservative, the relationship can be rewritten as:

$$V = (\rho/v)L^2 \cdot I \qquad (2)$$

where $v$ is the volume of material between the voltage measurement points.  By rearranging this equation to solve for $L$ and inserting it into the equation for true strain ($\varepsilon = \ln(L/L_o)$), strain is obtained as a function of voltage from the following formula:

$$\varepsilon_{\text{referenced}} = \frac{1}{2}\left[\ln\left(\frac{V_{\text{gauge}}}{V_{\text{gauge}_0}}\right) - \ln\left(\frac{V_{\text{ref}}}{V_{\text{ref}_0}}\right)\right] \qquad (3)$$

where $\varepsilon_{\text{referenced}}$ is the resistivity corrected creep strain, and "gauge" and "ref" are measurements across the gauge section and reference region, respectively.

Due to the difficulty of spot-welding the wires for DCPD at the idealized voltage measurement points, the actual voltage pickup points were at slightly different locations as shown in Figure 7. The deviation in voltage from idealized pickup points was assessed using FEM, and a correction factor as a function of gauge diameter was determined.  Further details on the development of this DCPD measurement method can be found in Ref. [3].
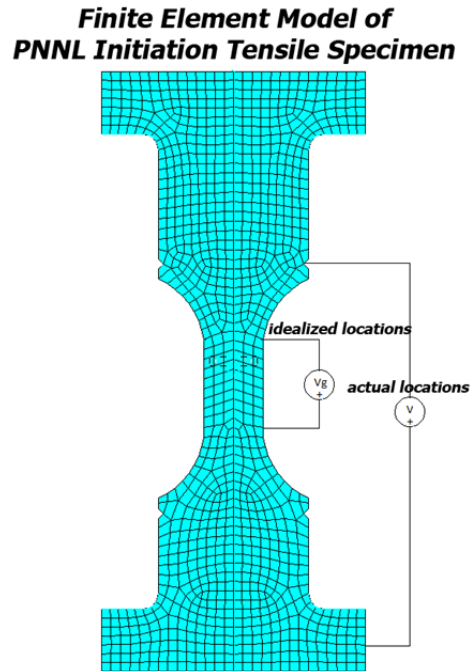


Figure 7.  2D representation of the axisymmetric FEM.  Actual gauge spot-weld locations versus idealized gauge spot weld locations are shown.

*SCC Initiation Test Method*

Most SCC initiation tests were conducted in an environment that simulates the PWR primary water (1000 ppm B, 2 ppm Li) at 360°C and 20.4 MPa with a dissolved hydrogen content of 25 cc/kg to maintain a corrosion potential at the Ni/NiO stability line.  The initial material and loading condition of all specimens are listed in Table 4.  All specimens were tested at or just

14

slightly above their as-prepared yield stress under constant load. Full load was applied to the specimens within 1-2 days of reaching full temperature enabling specimens to be pre-oxidized before loading. At the start of a test, the target load (the load at ~0.2% plastic strain) was achieved over a period of ~1 hour at a constant strain rate of ~$10^{-5}$ mm/s. This rate was chosen to load specimens to their yield stress sufficiently fast to reduce the risk for SCC formation during the initial loading. It also allows DCPD to monitor the stress-strain evolution with a sufficiently low noise level during this loading step. As shown in Figure 8, one specimen would sometimes yield slightly earlier than the others in a multi-specimen load train system due to intrinsic difference in yield strength and/or gauge diameter. In this case, small amounts of plastic strain up to ~1.5% were allowed in order to achieve yield in the other specimens. The specimens were then held at actively controlled constant load until crack initiation. All relevant environmental parameters and DCPD data were monitored and continuously written to a file. If a test was interrupted for surface examinations of precursor damage, or if a specimen had exhibited crack initiation, the remaining specimens were taken back to their original load upon restart of the test, again while monitoring stress versus strain during loading. Figure 9 shows the evolution of both non-referenced and referenced strains throughout exposure of a plate specimen. As mentioned in the previous section, by subtracting the reference voltage from the gauge voltage, the contribution of resistivity drift is eliminated in the referenced strain response. While creep and cracking are both likely to be simultaneously contributing to the measured response, the SCC initiation time is determined as any obvious increase in strain rate. Tests were stopped after clear confirmation of DCPD-based initiation to allow detailed characterizations of the specimen just after the onset of initiation as well as any accompanying specimens that had not yet initiated.

**IN045-47 - A600MA CRDM 93150**
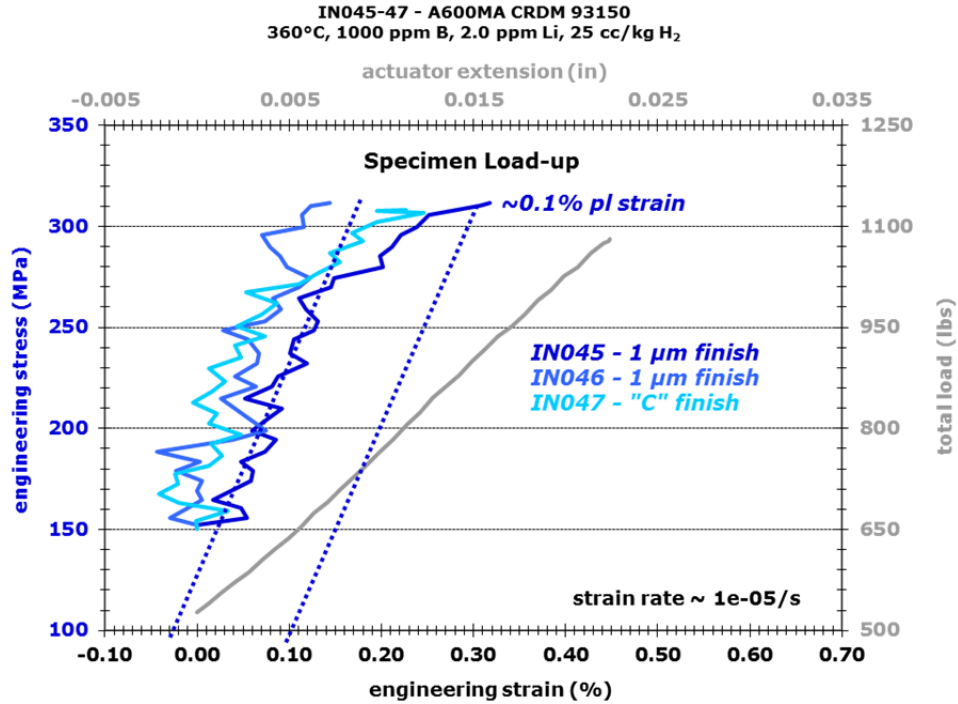**360°C, 1000 ppm B, 2.0 ppm Li, 25 cc/kg H₂**

Figure 8.  Example of stress versus strain plot during initial loading of tensile specimens for SCC initiation testing.  The displacement in actuator and the total load is plotted in the secondary x (upper) and y (right) axis, respectively.
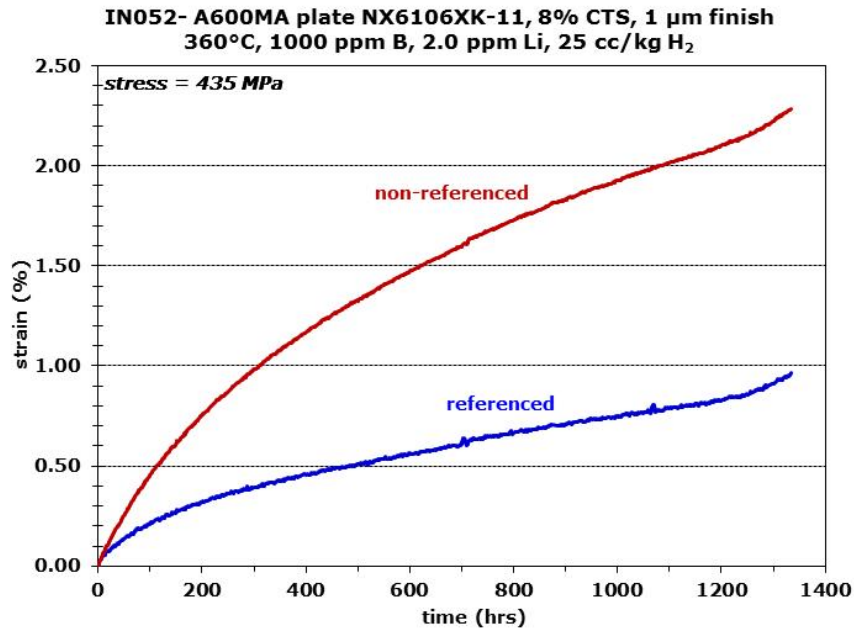


**IN052- A600MA plate NX6106XK-11, 8% CTS, 1 µm finish**
**360°C, 1000 ppm B, 2.0 ppm Li, 25 cc/kg H₂**

Figure 9.  Non-referenced and referenced DCPD strain response for IN052, a 8%CTS specimen from Alloy 600MA plate heat NX6106XK-11.

16

*Microstructural Characterizations*

Quantitative characterizations of IGA and shallow cracks in AR specimens without cold work were reported in detail previously [4, 10-12]. This time the microstructural examinations focus on the cracking morphologies in the 15%CF specimens after detection of SCC initiation. Inspections were conducted using a JEOL 7600 SEM. Oxford Aztec software was used to automate stage movement such that the entire gauge surface could quickly be mapped enabling montages to be created. For the specimens initiated but not failed, the entire gauge surface was examined. In order to achieve this, four fiducial scribe marks (90° to one another) were made at the button ends of each specimen to keep track of the specimen orientation. Each of the four orientations was then mapped using high-keV backscatter electron (BSE) montage imaging so that features covered by thin surface oxides can be revealed. For the failed specimens, the fractured surface was montaged under both high-keV secondary electron (SE) and low-keV BSE modes after ultrasonic cleaning to remove excessive boric acid residue. In addition, electron backscatter diffraction (EBSD) was performed selected specimen cross sections after surface examination revealed that the SCC initiation was associated with an elongated grain. A total area of 200×600 μm was typically scanned at 20 keV at a step size of ~10 μm.

*Material Selection*

The SCC initiation tests first started with two MA alloy 600 control rod drive mechanism (CRDM) nozzle heats M3935 and 93510, and one MA plate heat NX6106XK-11 at various cold work levels including AR (no CW), ~8%CW and ~20%CW. The detailed material condition and microstructures were summarized in an earlier milestone report [4]. A brief summary of the SCC initiation and characterization results on these materials will be provided in the next section along with new data obtained on these heats.

Since late 2015, PNNL has co-organized and participated in a round robin sponsored by the International Cooperative Group on Environment-Assisted Cracking (ICG-EAC) to investigate SCC initiation behavior in CW alloy 600 and to analyze lab-to-lab differences. Three heats were selected for this program: the MA PNNL plate heat NX6106XK-11, a SA alloy 600 heat 31907 provided by GE/EPRI, and a SA alloy 600 heat 11415 provided by Rolls Royce. The bulk compositions of these three heats along with the two previous CRDM heats are summarized in Table 1. The specimens for ICG-EAC round robin were all tested at 15%CF condition. The current report focuses on the new SCC initiation data obtained on these specimens. Data collected on six additional 15%CF alloy 600 NX6106XK-11 specimens tested in collaboration with a NRC/EPRI initiation program is also included for comparison.

Table 1.  Bulk compositions of alloy 600 materials selected for SCC initiation research (wt%).

| Product | Heat | Ni | Cr | Fe | Mn | C | Si | Cu | P | S | B, appm* |
|---|---|---|---|---|---|---|---|---|---|---|---|
| Service CRDM | M3935 | 77.9 | 15.6 | 6.3 | 0.27 | 0.028 | 0.37 | 0.01 | 0.004 | 0.002 | 69 |
| CRDM Tube | 93510 | 74.4 | 15.4 | 8.9 | 0.23 | 0.047 | 0.30 | 0.01 | 0.005 | 0.002 | 17 |
| Plate | NX6106XK-11 | 74.0 | 16.4 | 8.5 | 0.23 | 0.060 | 0.22 | 0.01 | 0.004 | 0.001 | 83 |
| Plate | 11415 | 75.6 | 15.6 | 8.36 | 0.19 | 0.04 | 0.20 | 0.03 | 0.003 | 0.001 | 1.7 |
| Plate | 31907 | 75.8 | 15.6 | 7.92 | 0.46 | 0.01 | 0.22 | 0.01 | 0.005 | 0.0002 | 46 |

*The B content is measured by glow discharge mass spectrometry (GDMS).

As part of the ICG-EAC round robin activities, examinations are being performed to document the grain boundary composition and precipitate structures in three alloy 600 materials with results detailed below.

Alloy 600 Plate Heat NX6106XK-11

The plate heat NX6106XK-11 was received in the form of a 5.08 mm (2 in) thick plate and in the MA condition reported as 927°C for 3.5 hours followed by a water quench.  As reported earlier [10], this material features an average grain size of 65 μm with transgranular (TG) carbides on ghost grain boundaries and a non-uniform distribution of IG carbides (Figure 10).  Optical examinations on the etched cross-sections of this material revealed bands of larger and smaller grains along the processing direction (Figure 11).  Some of the large "balloon" grains were highly elongated exceeding 1 mm in length.  As shown in Figure 12, part of the plate material was cut into 3.81 mm (1.5 in) long × 4.06 mm (1.6 in) × 5.08 mm (2 in) tall blocks and were cold forged to 15% reduction in thickness at GE Global Research for the new tests.  The forging direction was set to be coincident with the plate processing and banding planes.  Nine standard, 30.5 mm (1.2 in) tall uniaxial tensile specimens were tested at 15%CF levels.  All the specimens were tested in the same orientation with a 1 μm finish on the gauge section to facilitate identification of precursors and cracks on the surface.
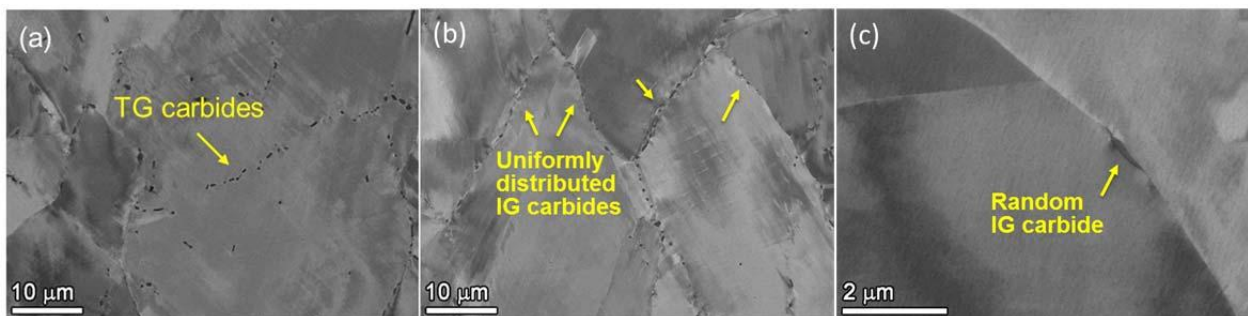


Figure 10.  SEM-BSE images of carbide distribution in the as-received MA alloy 600 plate heat NX6106XK-11 material: (a) most grains show primarily TG carbides, (b) few grains show higher density of IG carbides, and (c) more typical grain boundaries exhibiting low density of IG carbides.
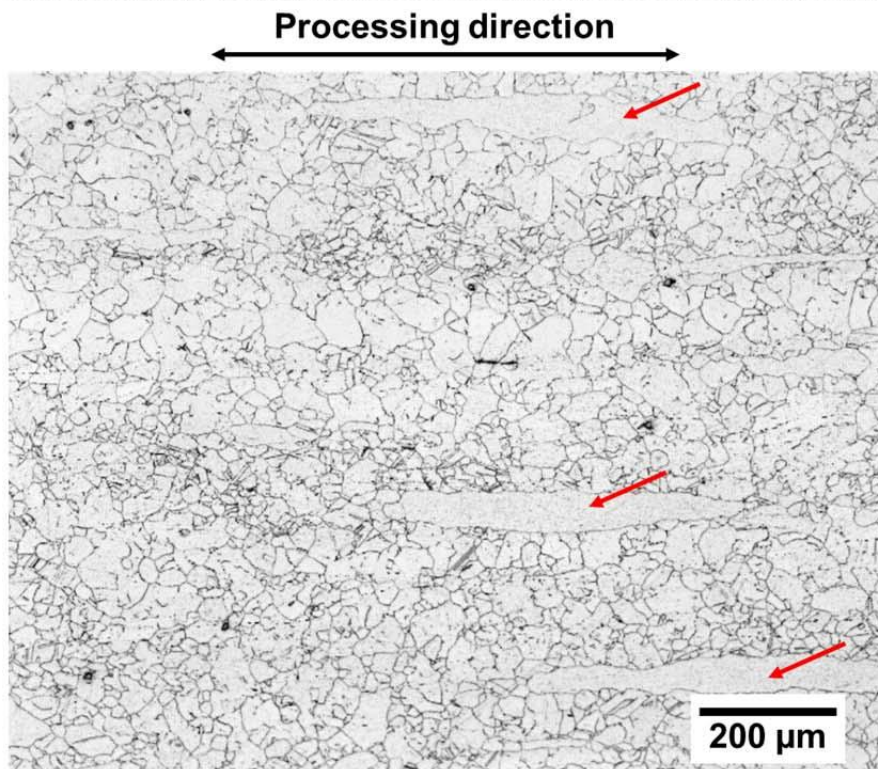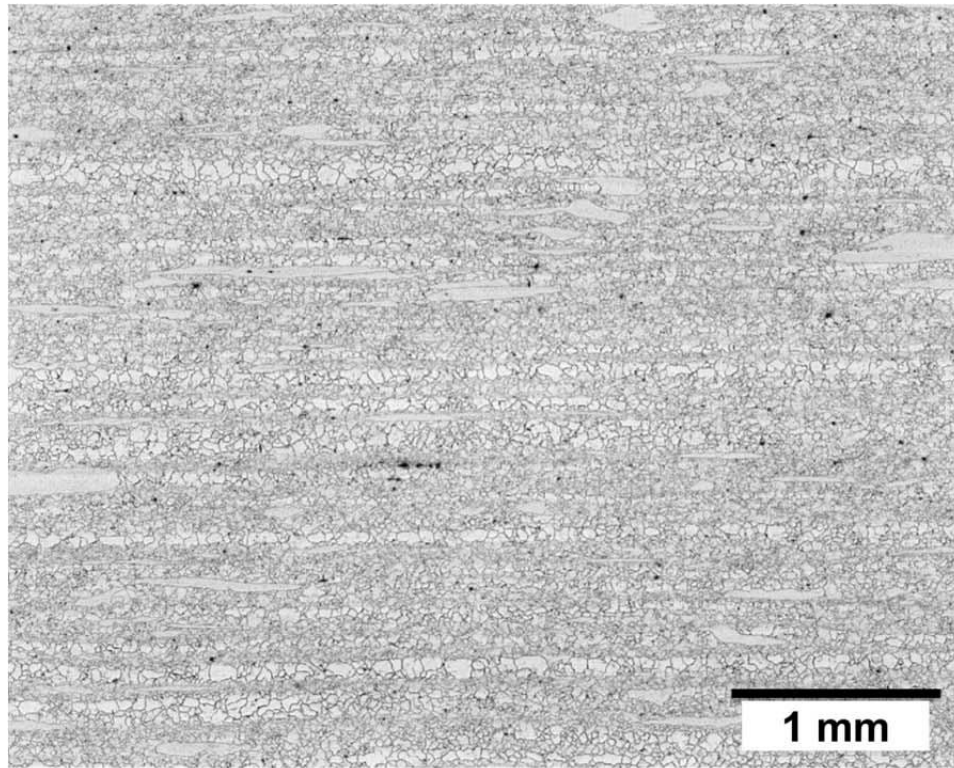
**Processing direction**



Figure 11. Optical image of the etched MA alloy 600 plate heat NX6106XK-11 material showing the inhomogeneous microstructure with large elongated grains highlighted by arrows.
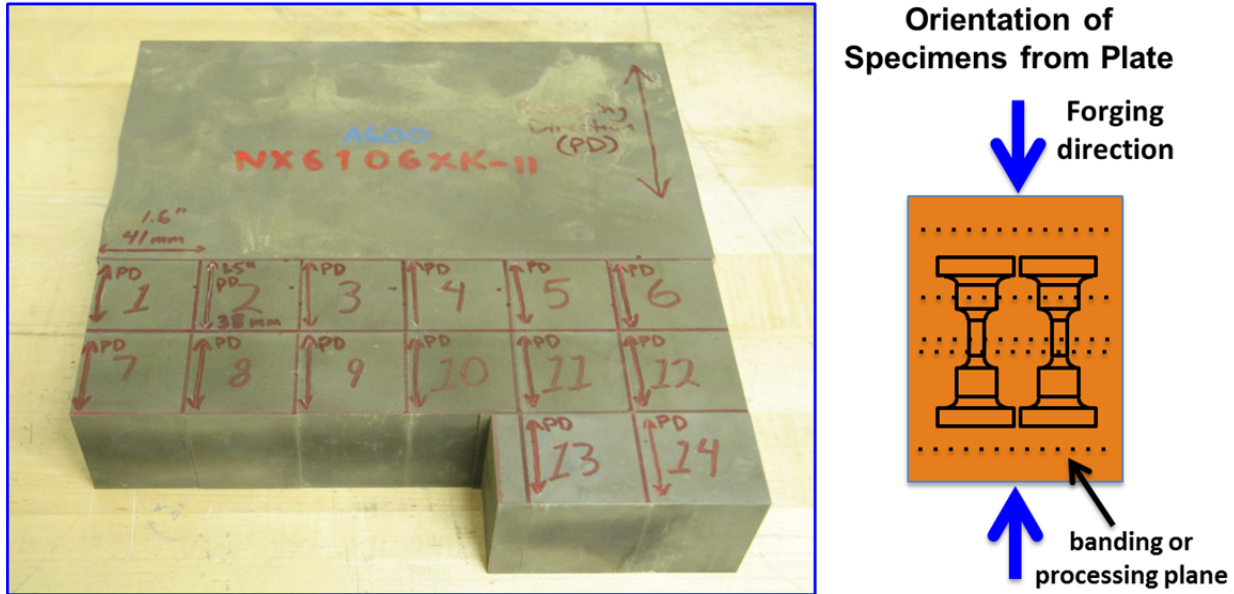
Figure 12. Preparation of the 15%CF blocks from the MA alloy 600 plate heat NX6106XK-11 for use in the testing.

As shown in Table 1, the GDMS measurements revealed surprisingly high B content in this material. Therefore, atom probe tomography (APT) has been utilized to examine grain boundary chemical composition variation. Presented in Figures 13 and 14 is an example of the APT data obtained on an IG carbide revealing strong segregation of B (~6 at%) and minor Si (~1.2 at%) to the carbide interface. The local chemistry at the interface was compared to previous data collected from the MA Davis Besse service CRDM heat (Figure 14). The latter exhibited high IGA and SCC susceptibility in which its high B coverage at grain boundaries is believed to have played a role. While similar B segregation (~6 at%) and Cr depletion (~5 at%) was observed in both materials, the Davis Besse material exhibited a high density of Ni-boride precipitates at carbide interface whereas the PNNL plate material showed none. However, only one APT sample has been characterized for the PNNL plate material so far. More data is needed to clarify the role of local chemistry variations in SCC initiation, especially at the boundaries between large elongated grains and small grains because they seem to serve as preferential sites for crack nucleation and growth, which will be discussed later in this report.
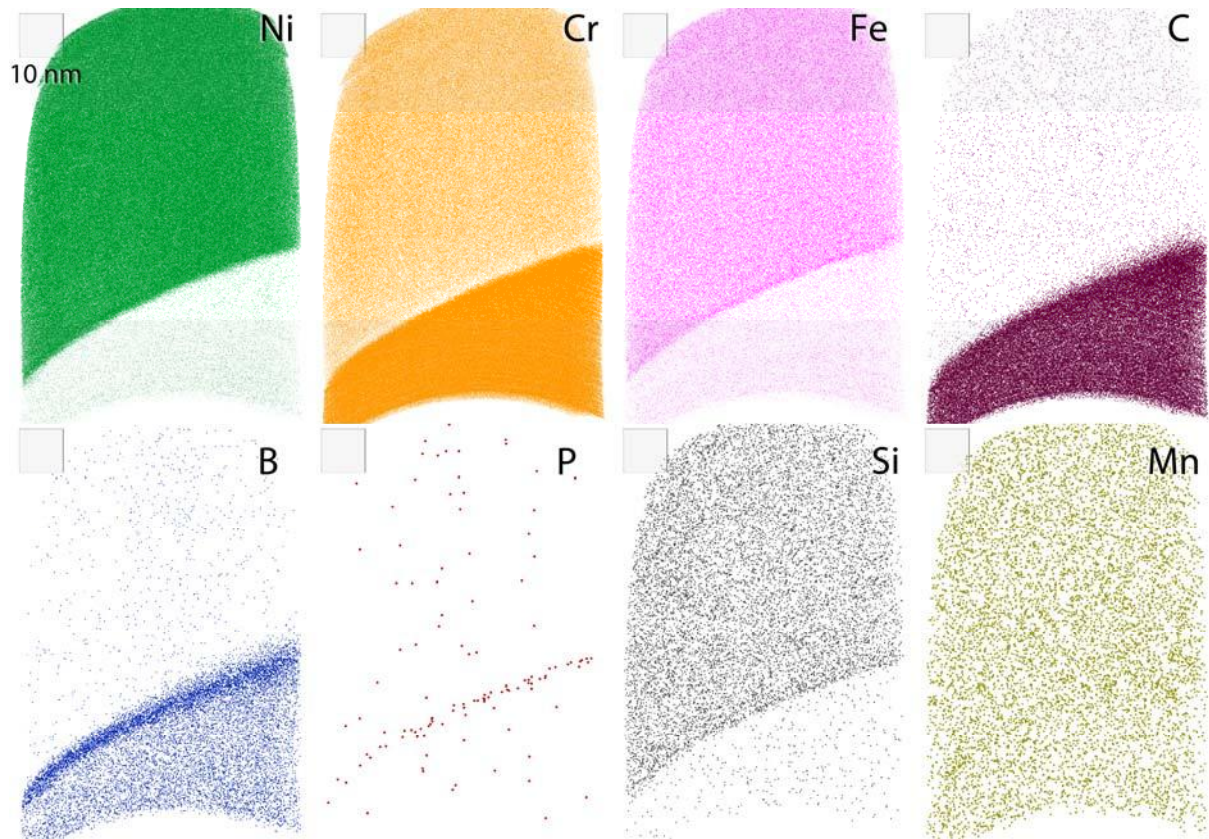
Figure 13.  APT atom maps of the MA alloy 600 plate heat NX6106XK-11 that contains a grain boundary carbide.  Segregation is visually observed for B, P and Si at the carbide/matrix interface.  Image depth is 10 nm.
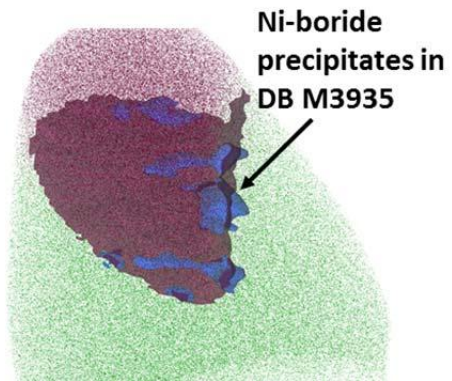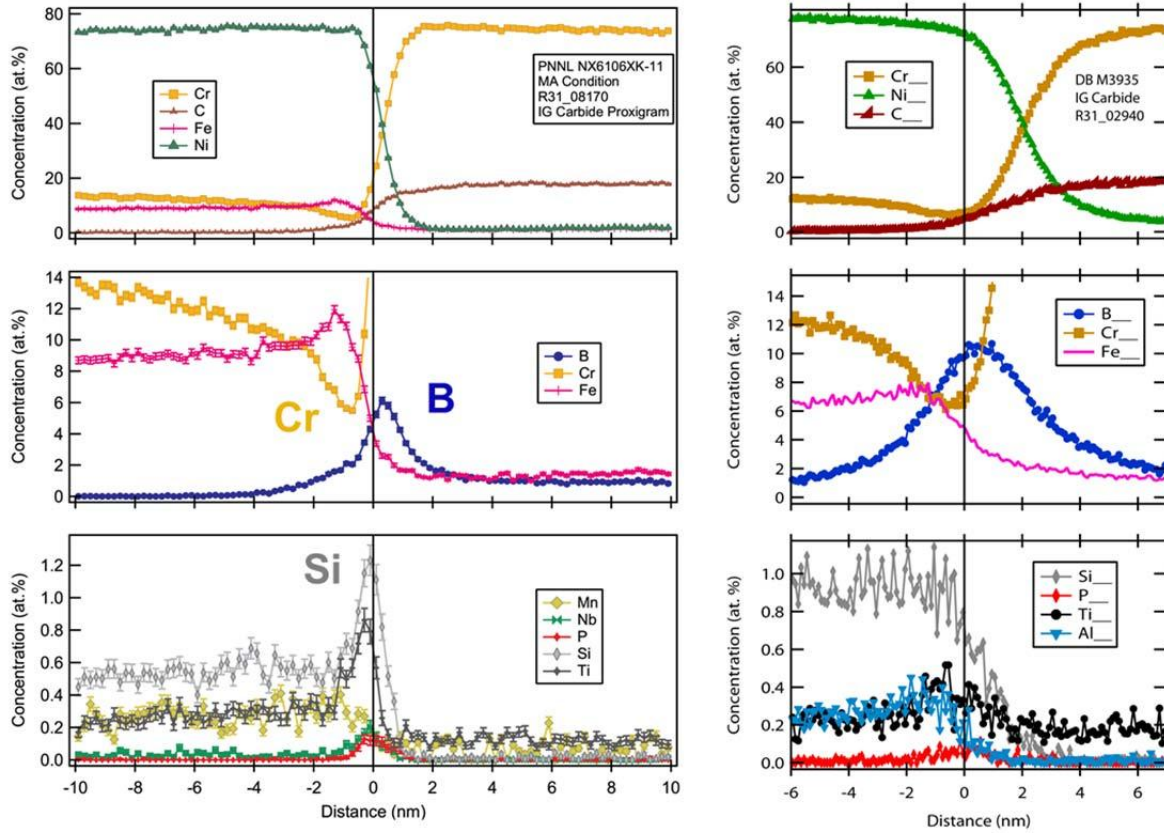
Figure 14. Comparison of the APT concentration profile across a precipitate/matrix interface in the MA alloy 600 plate heat NX6106XK-11 and the MA alloy 600 service CRDM heat M3935 (Davis Besse) that exhibited SCC in service and high crack-growth rates in lab tests.

Alloy 600 Plate Heat 31907

The EPRI/GE heat 31907, produced by Foroni, was received in the MA condition with a final heat treatment at 950°C for 3 h followed by a water quench. GE subsequently performed a SA treatment at 1100°C for 30 min followed by a water quench, which produced a duplex grain size distribution consisting of 50–200 μm grains in addition to much larger grains ~400–600 μm in diameter. High resolution SEM imaging of grain boundaries revealed no evidence for IG precipitates in the SA condition (Figure 15).
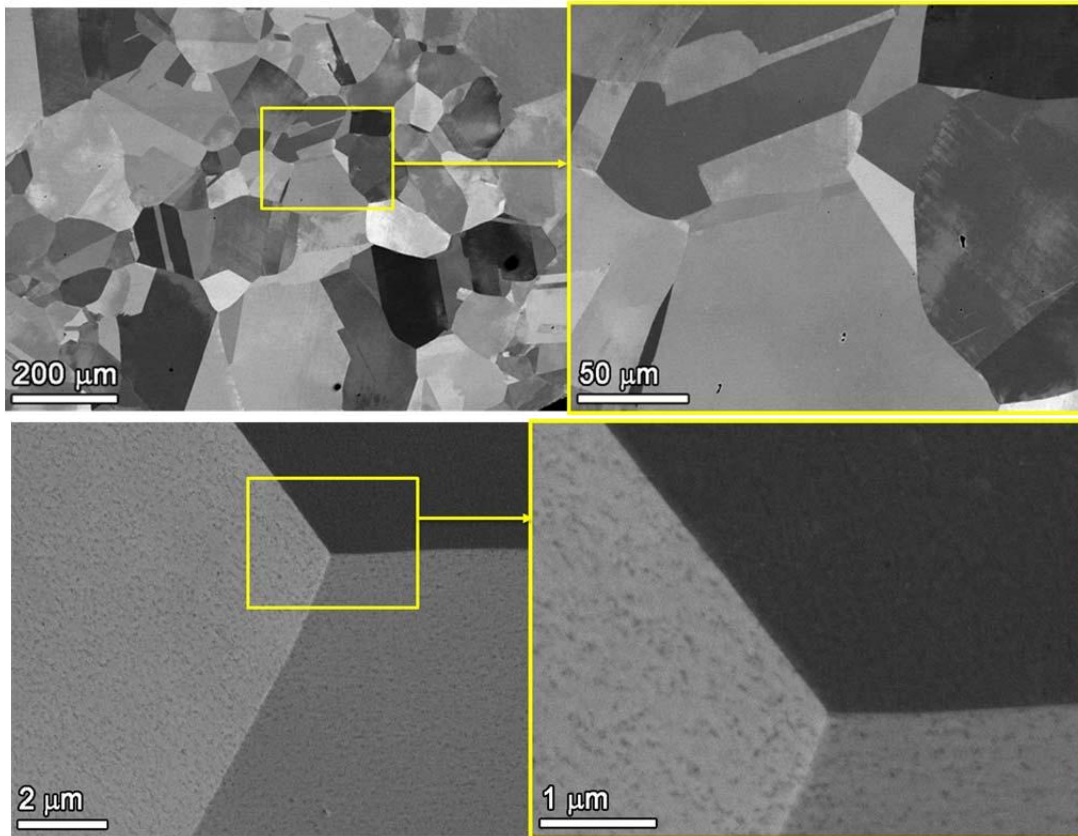


Figure 15. SEM-BSE images of grain size distribution (top) in the SA alloy 600 plate heat 31907 (Foroni) material and higher-magnification images of a grain boundary (bottom) revealing no apparent IG precipitation.
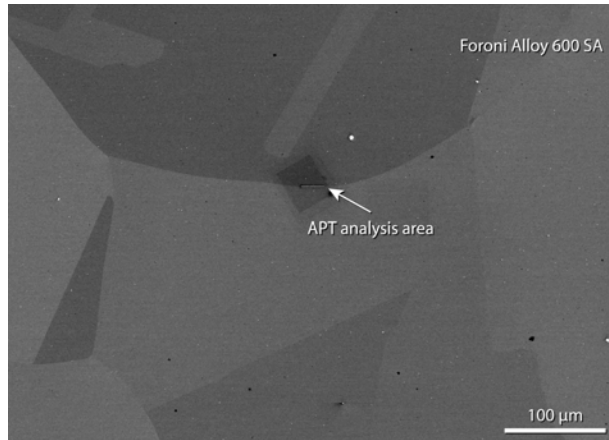
Figure 16. Low magnification SEM image of the grain boundary of Foroni alloy 600 in the SA condition that was selected for APT characterization.

As reported in Table 1, this material has a low bulk carbon content (0.01 wt%, ~0.002 at%) and a relatively high boron content (46 appm) compared to typical alloy 600 compositions. In order to quantify the grain boundary segregation of C and B, APT characterizations were performed on a section of high energy boundary selected from a relatively large grain (~400 μm in size) as shown in Figure 16. Two APT specimens successfully captured GB data. The first APT dataset is summarized in Figures 17 and 18. These atom maps and concentration profiles reveal segregation of B (1 at%), Si (0.9 at%), C (0.2 at%), P (0.2 at%) and Ti (0.54 at%). A slight Cr enrichment is also apparent at ~18 at% Cr. APT atom maps and concentration profiles of grain boundary segregation from the second APT dataset (R31_06413) of the SA condition are shown in Figures 19 and 20. These data generally agree well with the previous dataset but with slightly higher peak concentrations of B (~1.6 at%), Si (1 at%), C (0.3 at%), P (0.08 at%) and Ti (0.6 at%). Cr did not show any significant enrichment at this position of the grain boundary (17.2 at% Cr).
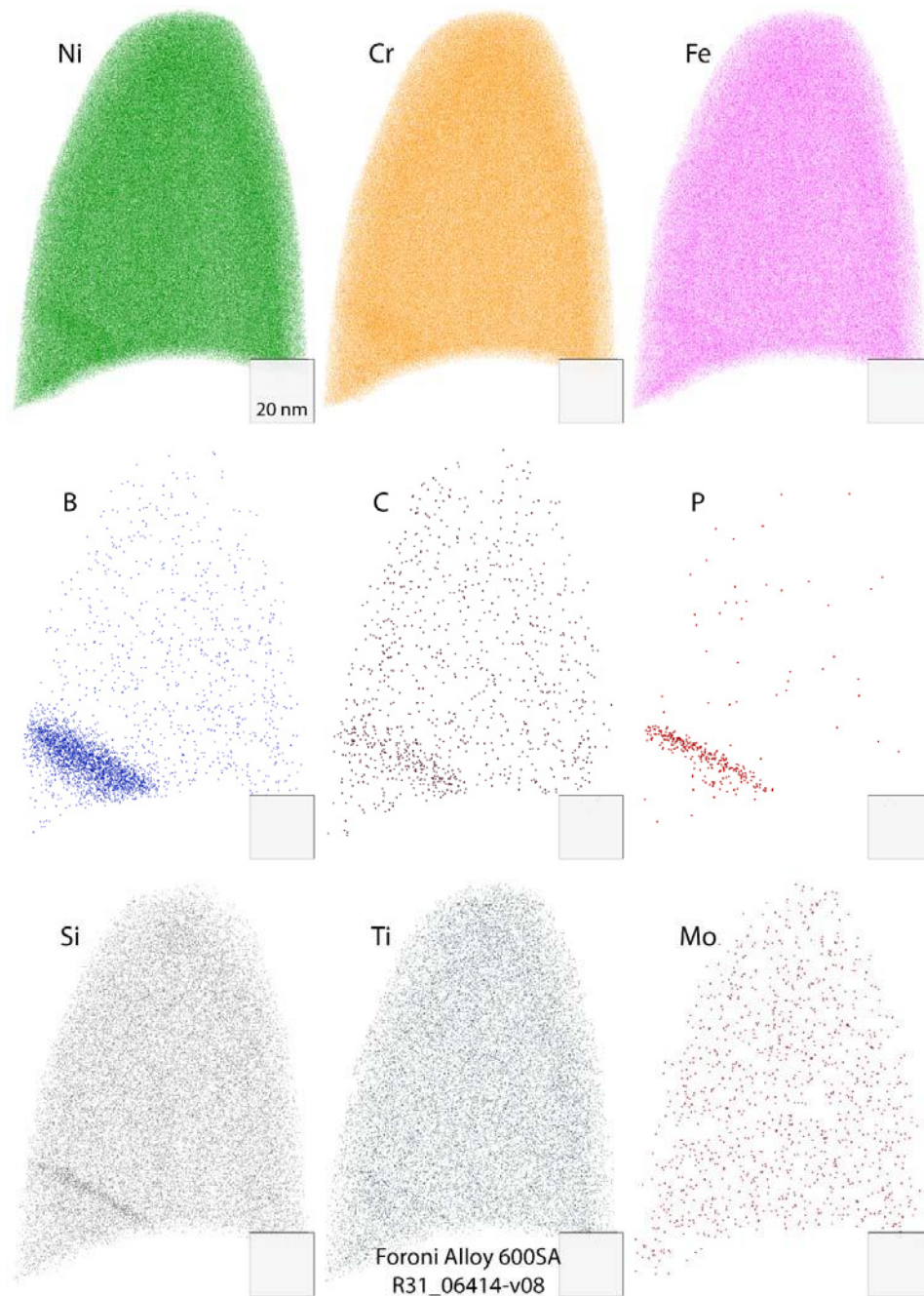
Figure 17. APT atom maps of the Foroni alloy 600 material in the SA condition. Segregation is visually observed for B, C, P and Si. Image depth is 20 nm.

Figure 18. APT concentration profile across a grain boundary in the SA condition, revealing segregation of B, Si, C, Ti and P at the grain boundary.

Figure 19. Atom maps from APT reconstruction depicting segregation at a grain boundary in the Foroni alloy 600 material in the SA condition. Image depth is 20 nm.

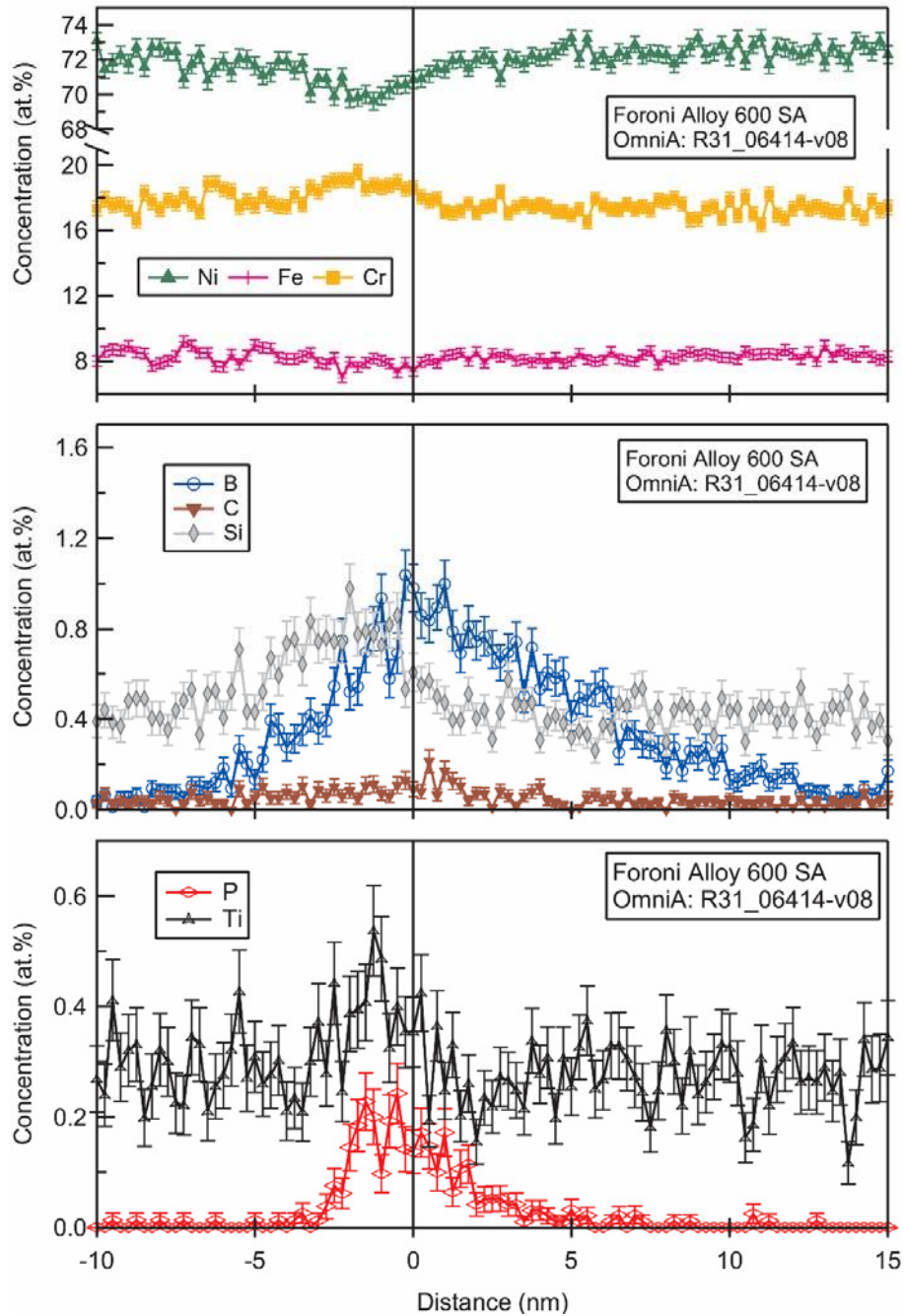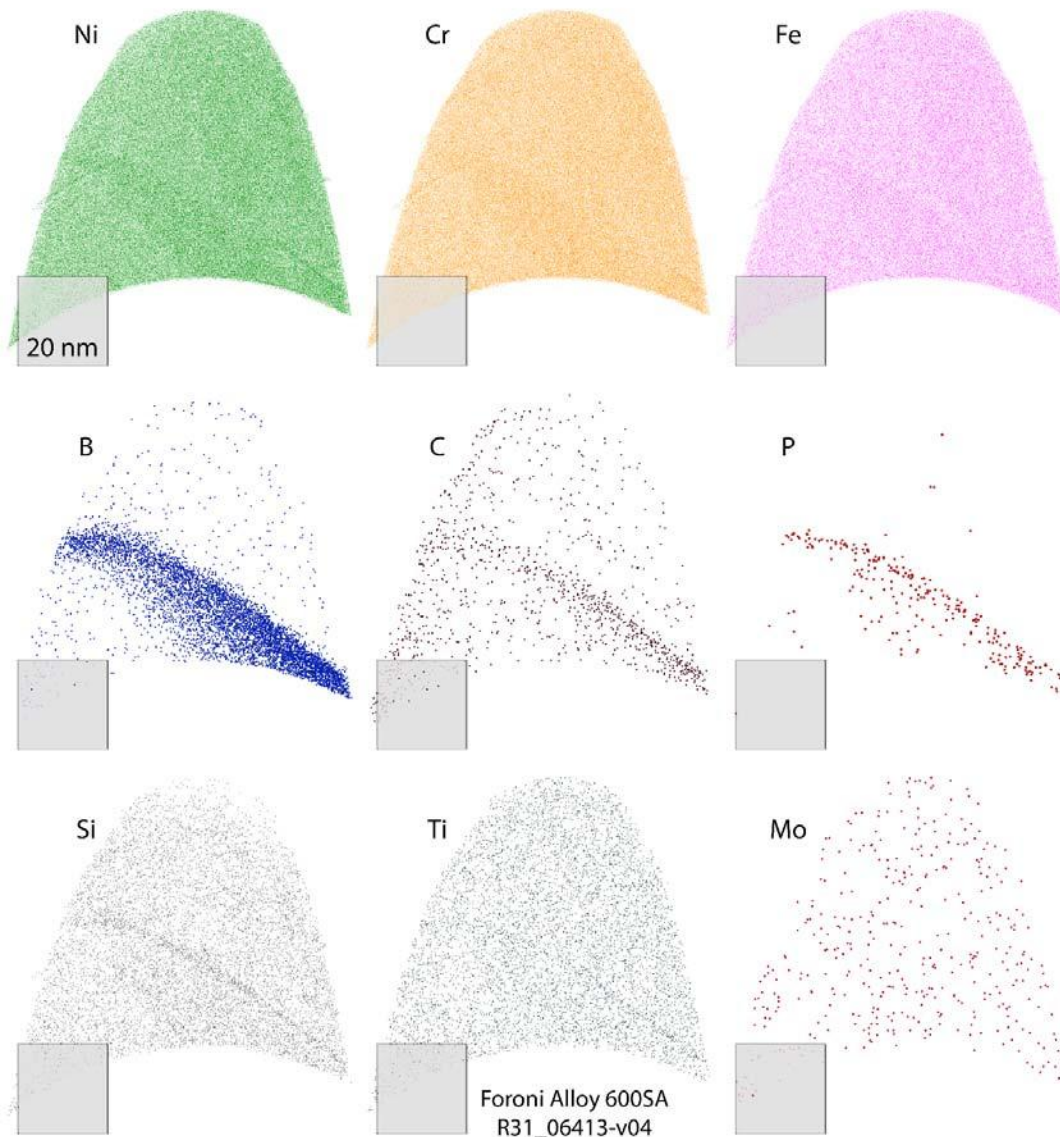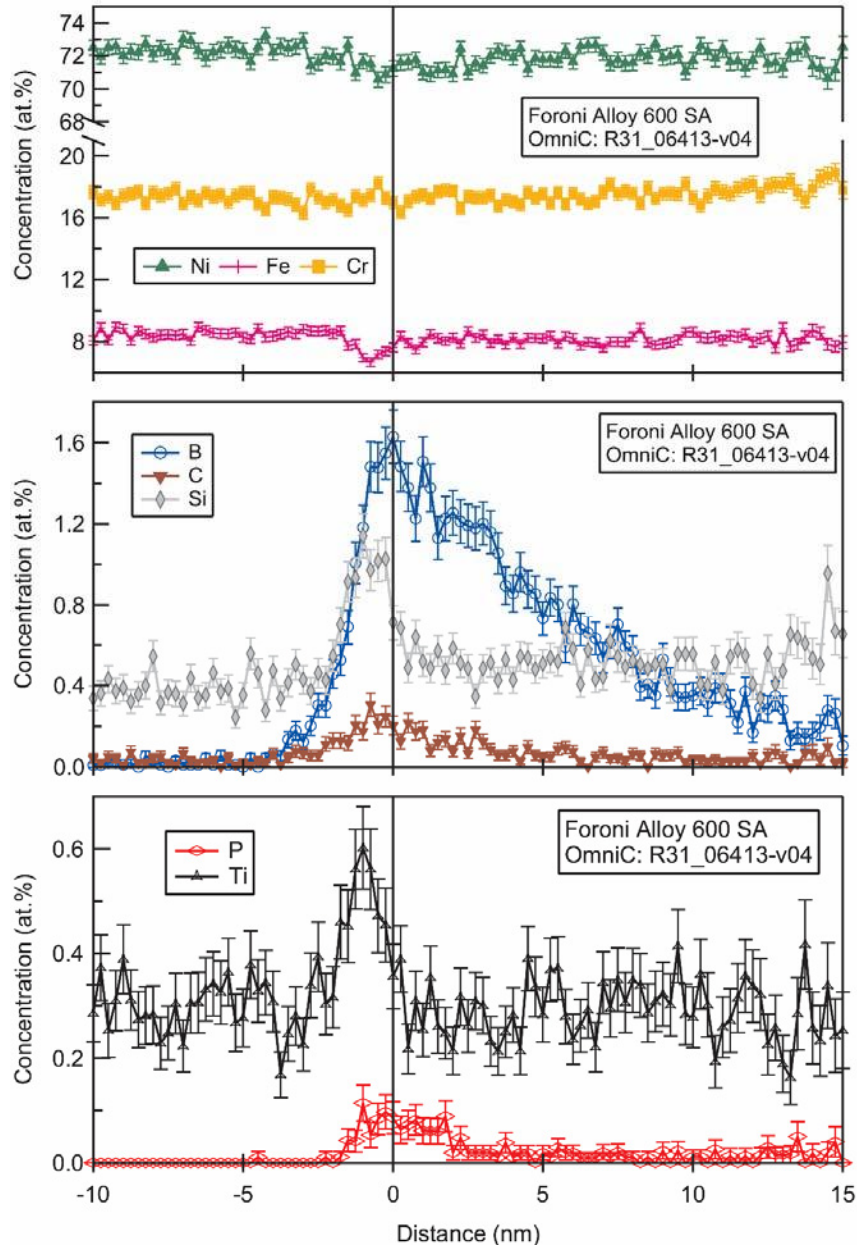Figure 20. APT concentration profile across a grain boundary from the SA condition of the Foroni alloy 600 material.

Comparisons are presented in Tables 2 and 3 of the current APT measurements of GB segregation in the SA Foroni alloy 600 material with several other alloy 600 heats. Note that most of these other alloy 600 heats were characterized in the MA condition, which generally allows for more diffusion and segregation than would be expected for a SA condition followed by a water quench. Nevertheless, similarities abound amongst these measurements both in terms of the maximum segregation (Table 2) and the enrichment ratio (Table 3). The B segregation of

the SA Foroni heat is higher than most of the other heats, but remarkably lower than the concentrations measured for heats M3935 and M7929, which correspond to relatively high-B heats of CRDM material. This suggests that the SA treatment and WQ of the Foroni heat was partially successful in reducing the segregation of B. Carbon segregation is also quite low in the Foroni heat, as one would expect from its low nominal C concentration and thermal history.

Table 2. Summary of APT measured GB concentrations (at%) for various alloy 600 heats. Notation of "-C" in the material description indicates close proximity of the measurement to an IG Cr carbide. The B segregation is also reported as the Gibbsian interfacial excess value ($\Gamma$, atom/nm$^2$). Measurements from the SA condition of the Foroni heat are highlighted.

| Material | B (atom/nm$^2$) | B (at%) | C+Mg | Cr | Si+N | P | Fe | Ti |
|---|---|---|---|---|---|---|---|---|
| M3935 - C | 22.98 | >6.00 | 1.2 | 5.8 | 1.2 | 0.25 | 8.1 | 0.65 |
| M7929 | 15.79 | >2.65 | 0.6 | 11.50 | 0.79 | 0.16 | 6.10 | 0.52 |
| NX4292 | 10.16 | 0.50 | 0.46 | 11.06 | 1.53 | 0.18 | 8.26 | 0.62 |
| E-110 | 4.68 | 0.97 | 0.7 | 15.93 | 0.88 | 0.09 | 8.21 | 0.6 |
| 96834 | 2.28 | 0.64 | 0.44 | 18.5 | 1.21 | 0.04 | 8.7 | 0.56 |
| WF422 | 1.65 | 0.56 | 0.28 | 11.80 | 2.33 | 0.23 | 11.0 | 0.86 |
| WF422 - C | 0.64 | *trace* | 0.60 | 6.70 | 1.70 | *trace* | 10.5 | 0.79 |
| Foroni SA R31_06413 | 11.60 | 1.63 | 0.3 | 17.2 | 1.02 | 0.08 | 7.77 | 0.60 |
| Foroni SA R31_6414 | 7.78 | 1.04 | 0.2 | 18.3 | 0.86 | 0.24 | 7.97 | 0.54 |

Table 3. Enrichment ratios of the measured GB segregation to the measured matrix concentration for various elements from various alloy 600 heats. Measurements from the SA condition of the Foroni heat are highlighted.

| Material | B | C+Mg | Cr | Si+N | P | Fe | Ti |
|---|---|---|---|---|---|---|---|
| M3935 - C | >600 | 13.33 | 0.38 | 1.45 | 25 | 1.25 | 2.71 |
| M7929 | >265 | 12.00 | 0.65 | 0.94 | 16 | 0.85 | 2.17 |
| NX4292 | 50 | 2.19 | 0.70 | 3.56 | 18 | 0.93 | 2.21 |
| E-110 | 97 | 7.78 | 0.92 | 2.20 | 0.9 | 0.80 | 2.61 |
| 96834 | 64 | 14.67 | 1.03 | 2.33 | 4 | 1.01 | 2.07 |
| WF422 | 56 | 5.60 | 0.69 | 2.59 | 23 | 1.11 | 2.97 |
| WF422 - C | - | 12 | 0.39 | 1.89 | - | 1.06 | 2.72 |
| Foroni SA R31_06413 | 163 | 15 | 0.99 | 2.49 | 8 | 0.93 | 1.88 |
| Foroni SA R31_06414 | 104 | 10 | 1.05 | 2.1 | 24 | 0.95 | 1.69 |

Alloy 600 Plate Heat 11415

The Alloy 600 plate heat 11415 provided by Rolls Royce was solution annealed at $1100^oC$ for 30 minutes followed by a water quench. As shown in Figure 21, this material exhibits a similar duplex grain size distribution as the SA EPRI/GE Foroni heat with grain diameters ranging from ~100 μm in diameter to much larger grains ~500 μm in diameter. High resolution imaging of grain boundaries revealed no evidence for IG precipitates in the SA condition (Figure 22). No APT was performed on this material since GDMS revealed little B content in the bulk.
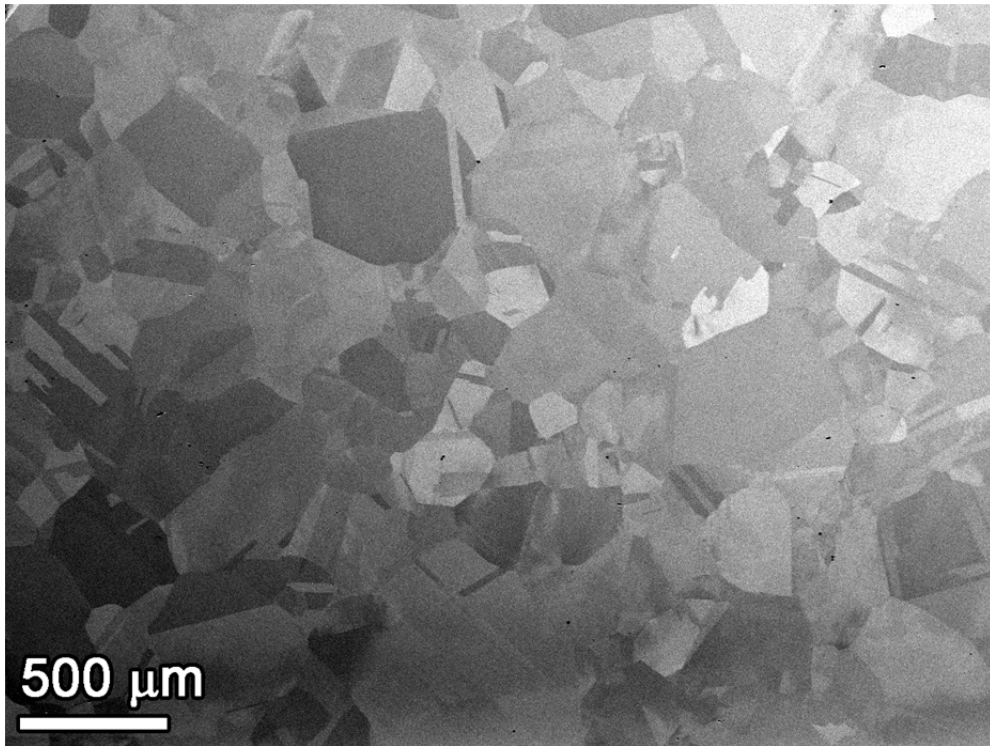


Figure 21. SEM-SE image of the microstructure in the Rolls Royce plate heat 11415 in the SA condition illustrating the large variation in grain size.
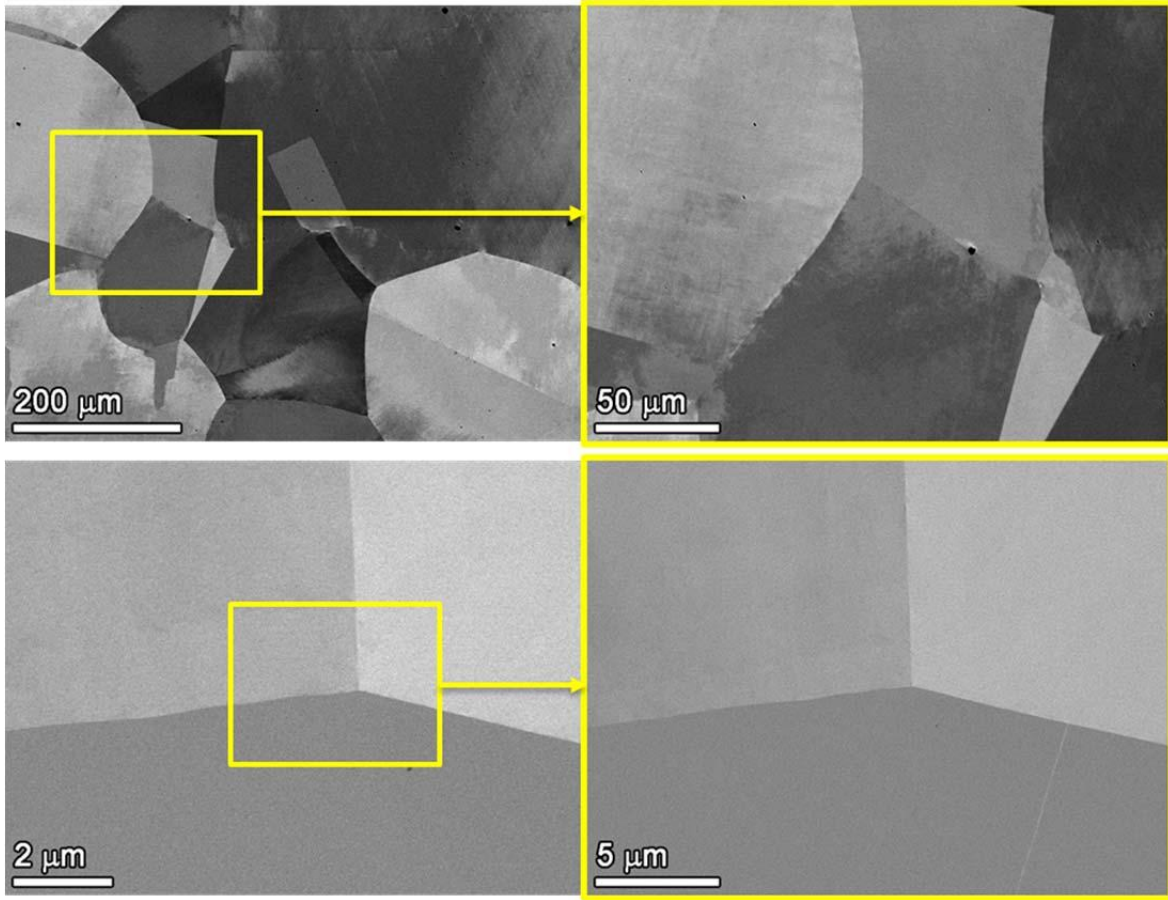
Figure 22.  SEM-BSE images of grain size distribution (top) in the SA alloy 600 plate heat 11415 (Rolls Royce) material and higher-magnification images of a grain boundary (bottom) revealing no IG precipitation.

**Review of Previous SCC Initiation Test Results on Alloy 600**

Previous constant load SCC initiation tests on the three MA alloy 600 heats M3935, 93510 and NX6106XK-11 at different cold work levels have established baseline responses for AR and CW alloy 600. Below is a brief summary of the in-situ DCPD measurements and characterization results on tested specimens with highlights on detectability of DCPD and effects of cold work and surface finish on SCC initiation.

*SCC Initiation Measurements*

Measured SCC initiation responses for 17 specimens from the three alloy 600 heats are summarized in Table 4. To date, tests have been terminated for 14 specimens with DCPD-indicated SCC initiation times determined for 10 of them. The remaining 4 specimens were removed before clear indication of SCC initiation for destructive characterizations in order to obtain complementary insights on the development of SCC precursors and the relationship between DCPD response and crack depth. Figure 23 illustrates the referenced DCPD strain responses for selected AR and CW specimens from the PNNL plate heat. As shown in Figure 23(a), a significant change in DCPD strain rate by a factor of 3 occurred in the 8%CTS specimen IN052 after 1250 h of exposure. In comparison, the AR ground specimens IN014 and IN015 in Figure 23(b) showed a very gradual increase in slope (25-50%) at exposure times ~6X longer than that for the 8%CTS IN052 specimen. Some AR specimens exhibited a small jump in DCPD-measured strain as illustrated for IN013 in Figure 23(c) where a 0.08% jump in strain can be seen at 5942 h. The DCPD record revealed that this jump took place within ~105 s, suggesting a relatively rapid change. Interestingly after the detection of this strain jump, the DCPD strain rate remained similar to the value prior to the jump. This suggests that the crack evolution after the strain jump had not altered appreciably. In order to better understand crack morphology associated with the strain jump, this specimen was removed after a total exposure of 6021 h for destructive characterizations.

Table 4.  PNNL Alloy 600 SCC Initiation Testing Status (09/2016).

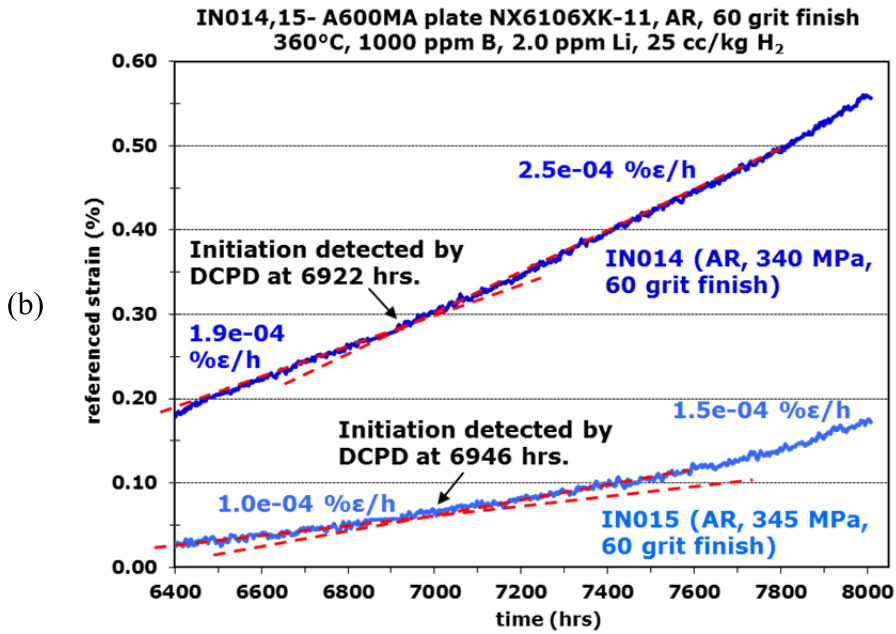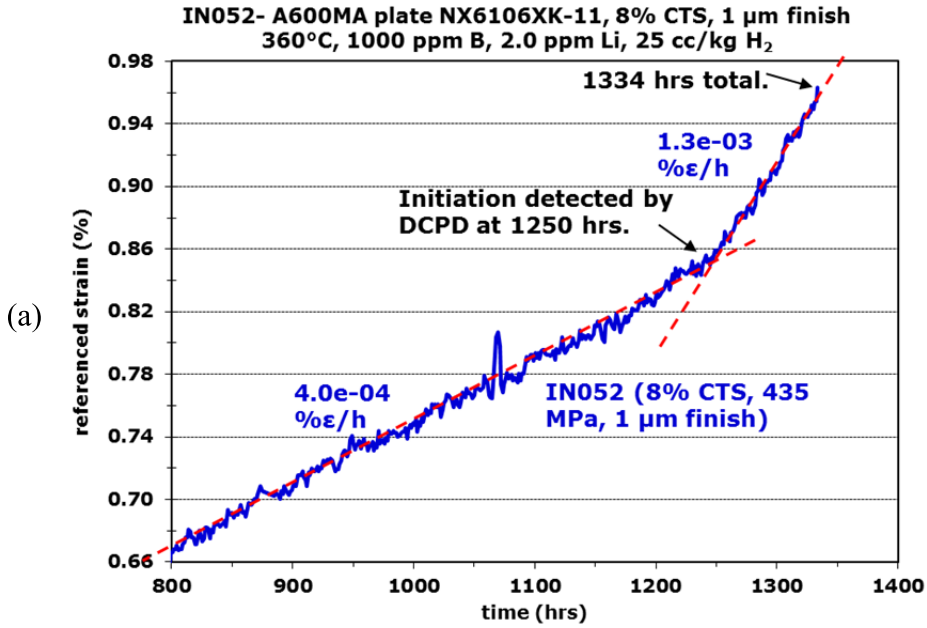| Spec. ID | Material Type | Heat Number | CW level | Finish | Applied Stress‡ (MPa) | Time to SCC Initiation (h) |
|---|---|---|---|---|---|---|
| IN022 | Service CRDM | M3935 | 20% CTS | 1 μm | 420 | 385▲ |
| IN048 | Service CRDM | M3935 | AR† | 1 μm | 240-255 | SJ* (3775) |
| IN049 | Service CRDM | M3935 | AR | 1 μm | 240-255 | 3806▲ |
| IN050 | Service CRDM | M3935 | AR | "C" | 240-255 | NI** (5785) |
| IN002 | CRDM | 93510 | 18% CTS | 1200 grit | 740 | 2025 |
| IN003 | CRDM | 93510 | 18% CTS | 1 μm | 740 | 1775 |
| IN023 | CRDM | 93510 | 5-7% CTS | 1 μm | 425-445 | 2183 |
| IN045 | CRDM | 93510 | AR | 1 μm | 290 | 4967▲ |
| IN046 | CRDM | 93510 | AR | 1 μm | 290 | NI (10200) |
| IN047 | CRDM | 93510 | AR | "C" | 290 | NI (10200) |
| IN016 | Plate | NX6106XK-11 | 19% CR | 1 μm | 610 | 1522 |
| IN017 | Plate | NX6106XK-11 | 19% CR | 60 grit | 610-634 | 1787 |
| IN018 | Plate | NX6106XK-11 | 19% CR | 60 grit | 610-634 | 1715 |
| IN052 | Plate | NX6106XK-11 | 8% CTS | 1 μm | 435 | 1250 |
| IN013 | Plate | NX6106XK-11 | AR | 1 μm | 330-350 | SJ (5942) |
| IN014 | Plate | NX6106XK-11 | AR | 60 grit | 330-340 | 6922 |
| IN015 | Plate | NX6106XK-11 | AR | 60 grit | 330-345 | 6946 |

‡ The applied stress is the yield stress of the specimens at the tested temperature ($360^{o}C$).

† AR = as-received condition, no cold work.  CTS = cold tensile strained.  CR = cold rolled.

▲ Test stopped before clear indication of SCC initiation.

* SJ = strain jump detected in DCPD strain response.  Time in parenthesis is the total exposure time when the strain jump was observed.

** NI = no DCPD-detected initiation.  Time in parenthesis is the total exposure time.

(a)

IN052- A600MA plate NX6106XK-11, 8% CTS, 1 µm finish
360°C, 1000 ppm B, 2.0 ppm Li, 25 cc/kg H₂

1334 hrs total.

1.3e-03 %ε/h

Initiation detected by DCPD at 1250 hrs.

4.0e-04 %ε/h

IN052 (8% CTS, 435 MPa, 1 µm finish)

(b)

IN014,15- A600MA plate NX6106XK-11, AR, 60 grit finish
360°C, 1000 ppm B, 2.0 ppm Li, 25 cc/kg H₂

2.5e-04 %ε/h

Initiation detected by DCPD at 6922 hrs.

IN014 (AR, 340 MPa, 60 grit finish)

1.9e-04 %ε/h

Initiation detected by DCPD at 6946 hrs.

1.5e-04 %ε/h

1.0e-04 %ε/h
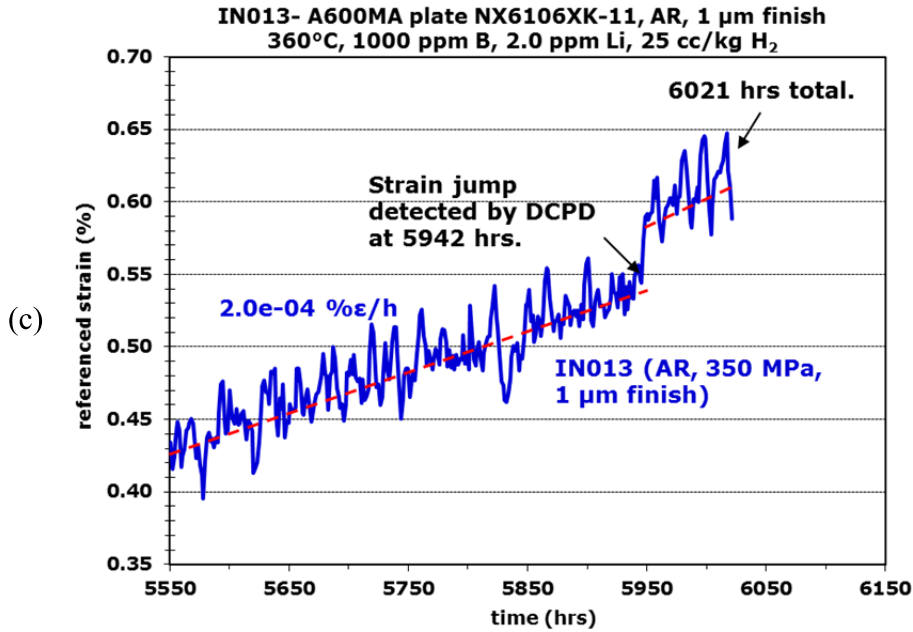
IN015 (AR, 345 MPa, 60 grit finish)

34

**(c)**

Figure 23. Referenced DCPD strain response for four specimens from the Alloy 600MA plate heat NX6106XK-11 tested at their yield stress: (a) IN052 - an 8%CTS specimen with 1 μm finish, (b) IN014 & 15 - two AR specimens with 60 grit finish, and (c) IN013 - an AR specimen with 1 μm finish.

The referenced DCPD strain responses for all the service CRDM specimens are summarized in Figure 24. A higher-than-normal steady strain rate was observed in the 22%CTS specimen IN022 from the very start of the test (Figure 24a). Since this heat exhibited high SCC crack growth susceptibility in the AR (non-CW) condition [9, 13], it was suspected that crack nucleation had occurred at the onset of the test of this CW specimen and the test was terminated after 385 h of exposure. Post-test characterization revealed significant cracking with the primary crack reaching a depth of 350 μm, comparable to those in other CW specimens that showed clear DCPD-indicated crack initiation. This suggests that significant growth of nucleated cracks occurred immediately from the start of the test for IN022. Based on the crack depth observations, the time at which the test was stopped (385 h) was considered to be a reasonable estimate of the SCC initiation time. This is the only CW sample tested for SCC initiation in this heat and more tests are needed to confirm the behavior of this material. For the AR material, one of the 1 μm finish AR specimens IN048 showed a strain jump of ~0.3% at ~3775 h (Figure 24b). Again, no obvious immediate change was observed in the strain rate afterwards. The decision was made to remove this specimen along with a companion specimen (IN049) so that the crack morphology in these two could be compared, while the test on the AR ground specimen (IN050) was continued for another ~2000 h without any observable DCPD indication of initiation.
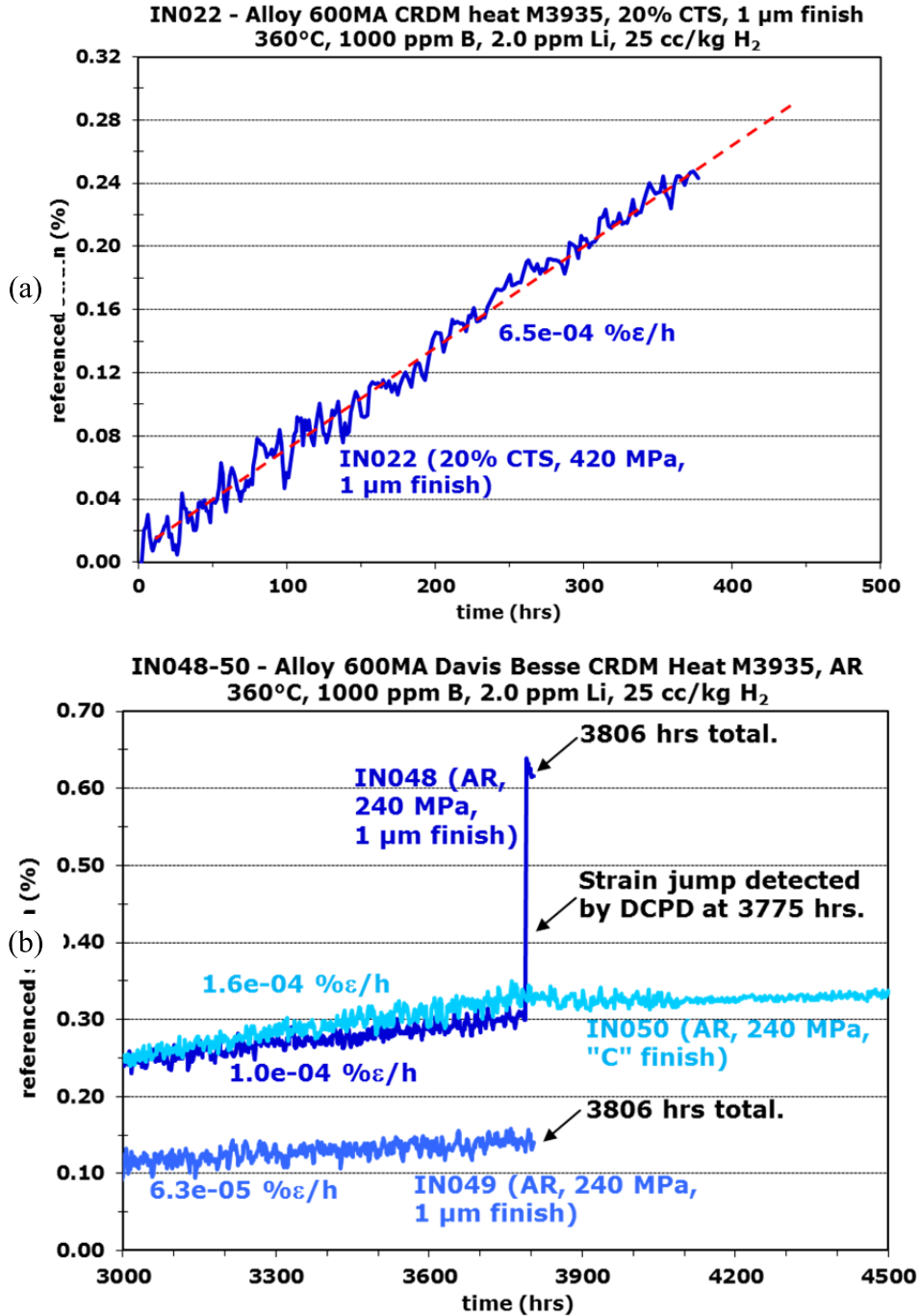
Figure 24. Referenced DCPD strain response for four specimens from the Alloy 600MA CRDM service heat tested at their yield stress: (a) IN022 - a 20%CTS specimen with 1 μm finish and (b) IN048, 49 & 50 - three AR specimens.
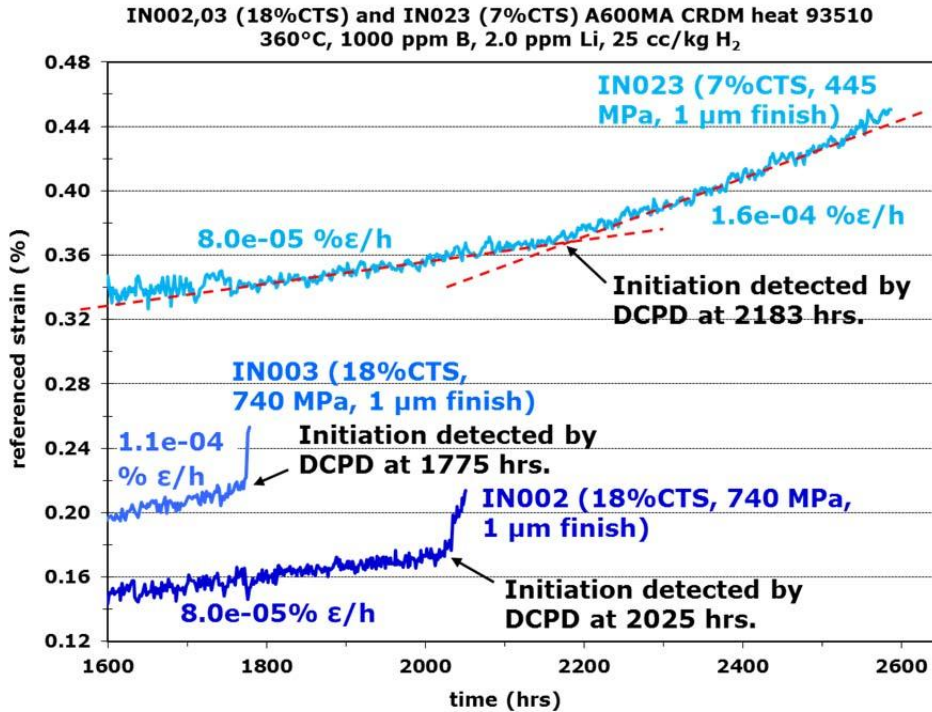
Figure 25. Referenced DCPD strain response for three CW specimens from the Alloy 600MA CRDM heat 93510 tested at their yield stress.

As shown in Figure 25, the CW specimens from the CRDM tube heat 93510 exhibited similar DCPD strain response as the PNNL plate heat in the CW condition. While the 7%CTS specimen IN023 showed a more gradual strain rate increase than the other two 93510 specimens with higher CW levels (IN002 and IN003), its DCPD-indicated SCC initiation time is only slightly longer than the 20%CW specimens. In contrast, no SCC initiation has been observed for the AR specimens after ~8000 h of exposure, which is more than 3 times longer than the 7%CTS specimen IN023. The results on this heat and the plate heat demonstrate that a relatively small amount of cold work can significantly increase SCC initiation susceptibility in MA alloy 600.

*SCC Initiation Characterizations*

Surface examinations were conducted to document the evolution of IGA, small cracks and large cracks that developed during exposure. Despite variations in composition and microstructure, the AR and CW specimens from the three alloy 600 heats tested exhibit similar IGA and crack morphologies. Examples are provided in Figure 26, where an etched grain boundary appearance due to IGA was observed on 80-90% of the high-energy grain boundaries intersecting the surface regardless of the exposure time and the orientation of the high-energy grain boundaries to the applied stress. Meanwhile, IG cracks perpendicular to the loading direction were observed sporadically on high-energy grain boundaries. While the morphology of these features on the cross sections of the AR (Figure 27) and the CW (Figure 28) materials are similar, a higher density of long circumferential cracks with surface length >200 μm were observed in the AR specimen. Comparison of the images taken of the same region at increasingly longer exposure time suggests that these long circumferential cracks were formed predominantly by growth and coalescence of smaller cracks (Figure 29). The depth of these long circumferential cracks was documented after the conclusion of a test by serial polishing and SEM examinations of cross sections to establish crack depth profiles as illustrated in Figures 30 and 31. Most circumferential cracks greater than 200 μm in length could be approximated by a semi-elliptical shape. The maximum depth of every crack observed is shown as a function of its surface length in Figures 32 and 33 for selected plate heat and service CRDM heat specimens, respectively.

Although the crack density differs in specimens due to factors such as microstructure and applied stress, the trend in the change of crack geometry is consistent in the AR specimens as well as in the CW specimens from these two heats. It was found that the aspect ratio (crack depth divided by ½ the crack surface length) of cracks less than ~200 μm in depth is ~0.8 for both the AR and CW materials. However, distinctively different crack growth behavior was observed for deeper cracks in the AR and CW specimens after a threshold crack geometry was reached. The depth of cracks continues to increase in the CW specimens producing similar or higher aspect ratios up to the point of DCPD-detected SCC initiation, but crack depths saturate for the AR materials after a critical shape is reached despite further evolution of the surface crack length. As a result, the crack aspect ratio drops to <0.2 for the largest cracks as can be seen in Figures 32 and 33.
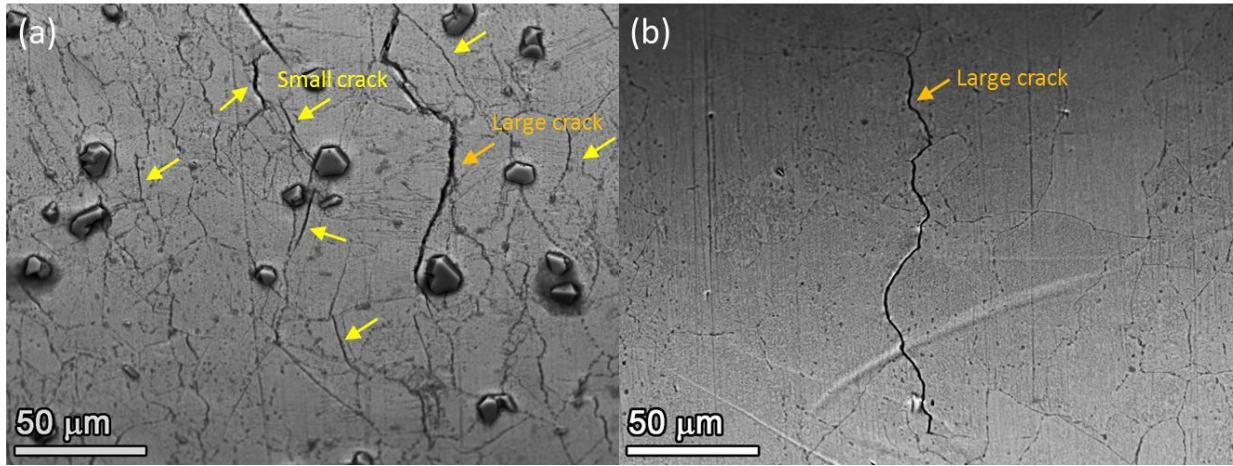
Figure 26. SEM-BSE images of typical IGA (tight grooves delineating high-energy grain boundaries) and crack morphology (marked by arrows) on the surface of specimens from MA alloy 600 plate heat NX6106XK-11: (a) IN013 (AR, 1 μm finish, 330 MPa, 6021 h exposure) and (b) IN052 (8%CTS, 1 μm finish, 435 MPa, 1334 h exposure).
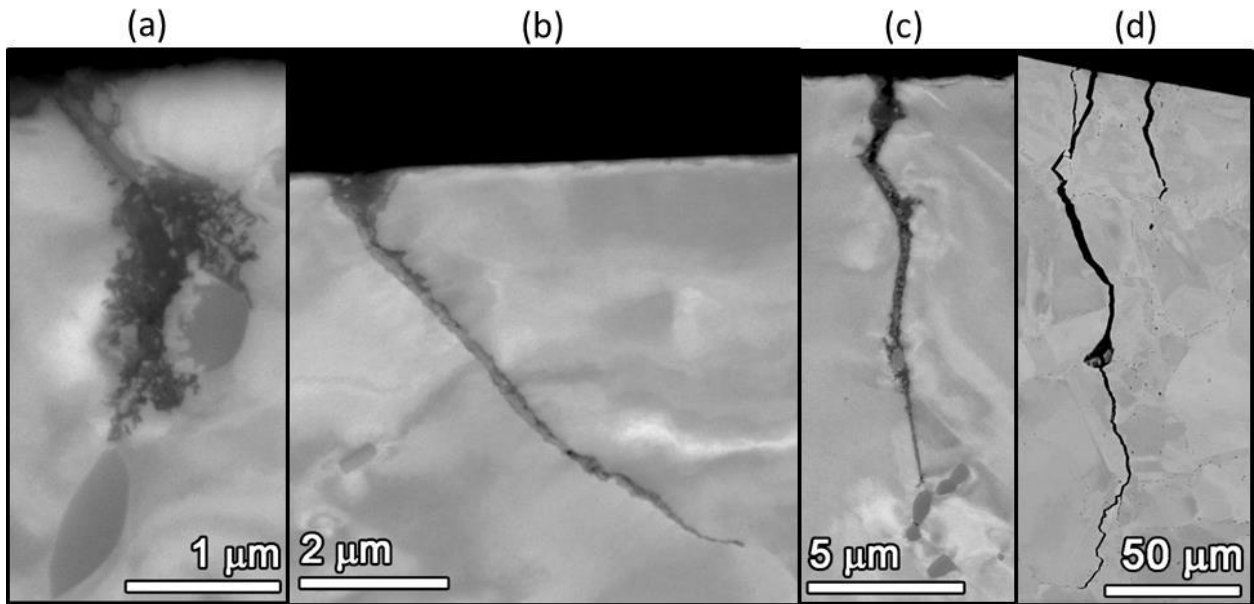


Figure 27. SEM-BSE images of typical morphology of IGA (a,b), small crack (c) and large crack (d) on the cross-section of IN013, a highly polished AR specimen from the plate heat NX6106XK-11.
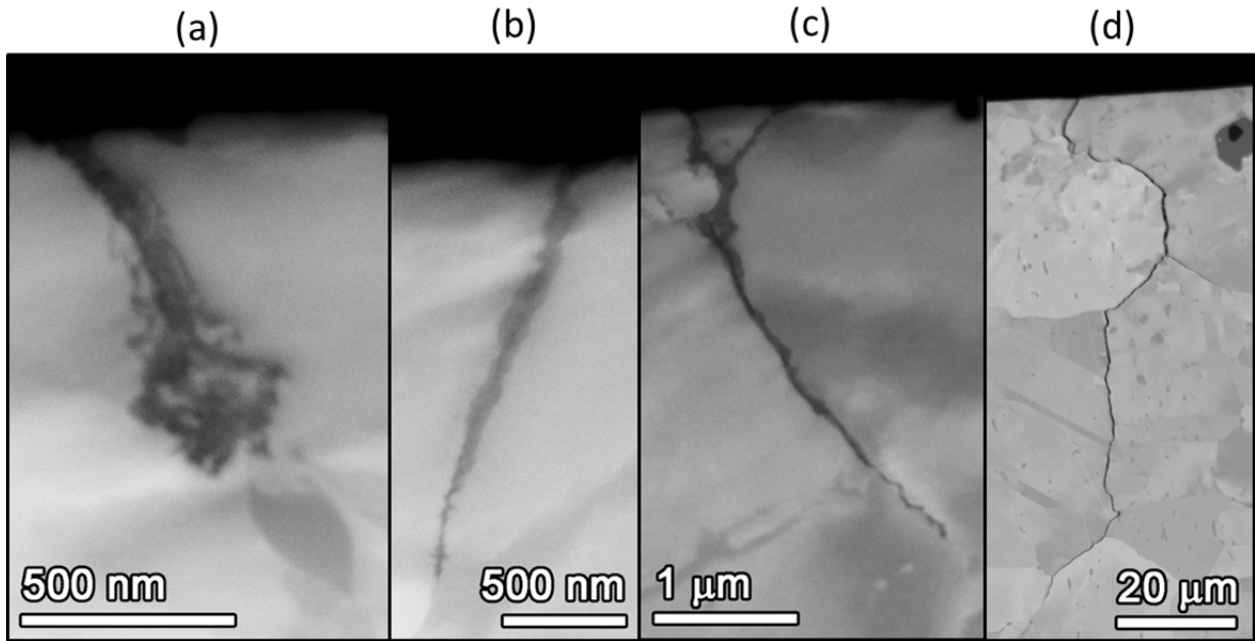
Figure 28.  SEM-BSE images of typical morphology of IGA (a,b), small crack (c), and large crack (d) on the cross-section of IN052, a highly polished 8%CTS specimen from the plate heat NX6106XK-11.
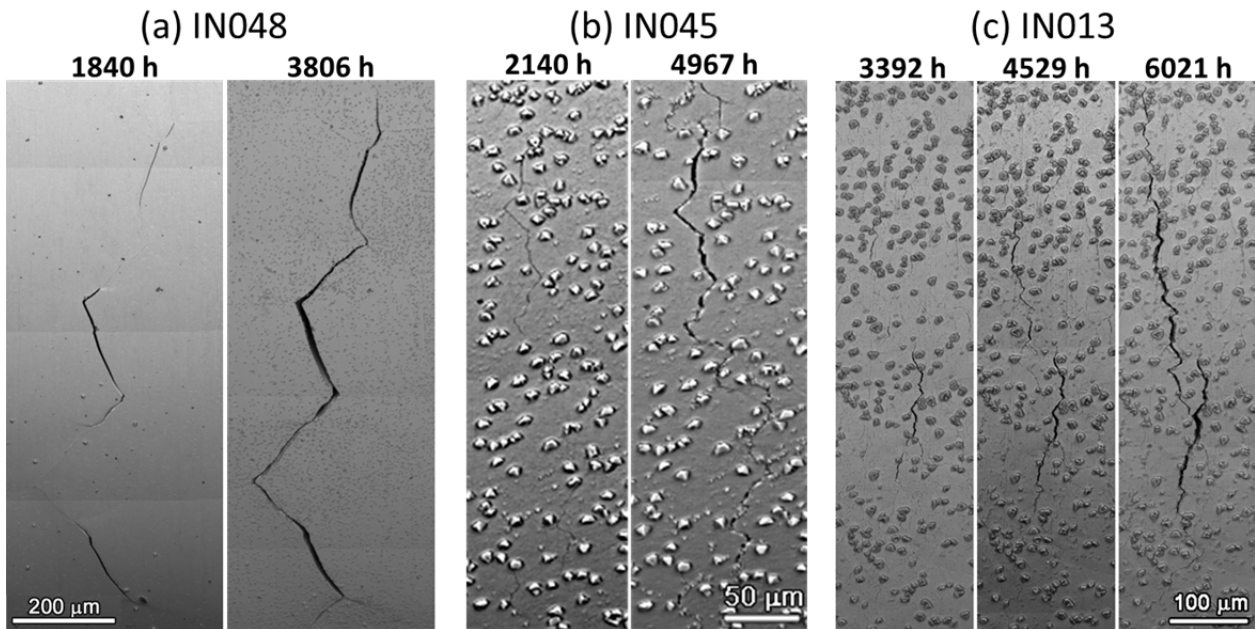


Figure 29.  SEM-BSE images of coalescence of multiple cracks observed at the same site with progress in exposure time in the AR specimens from the three tested heats: (a) IN048 of the CRDM heat M3935, (b) IN045 of the CRDM tube heat 93510 and (c) IN013 of the plate heat NX6106XK-11.
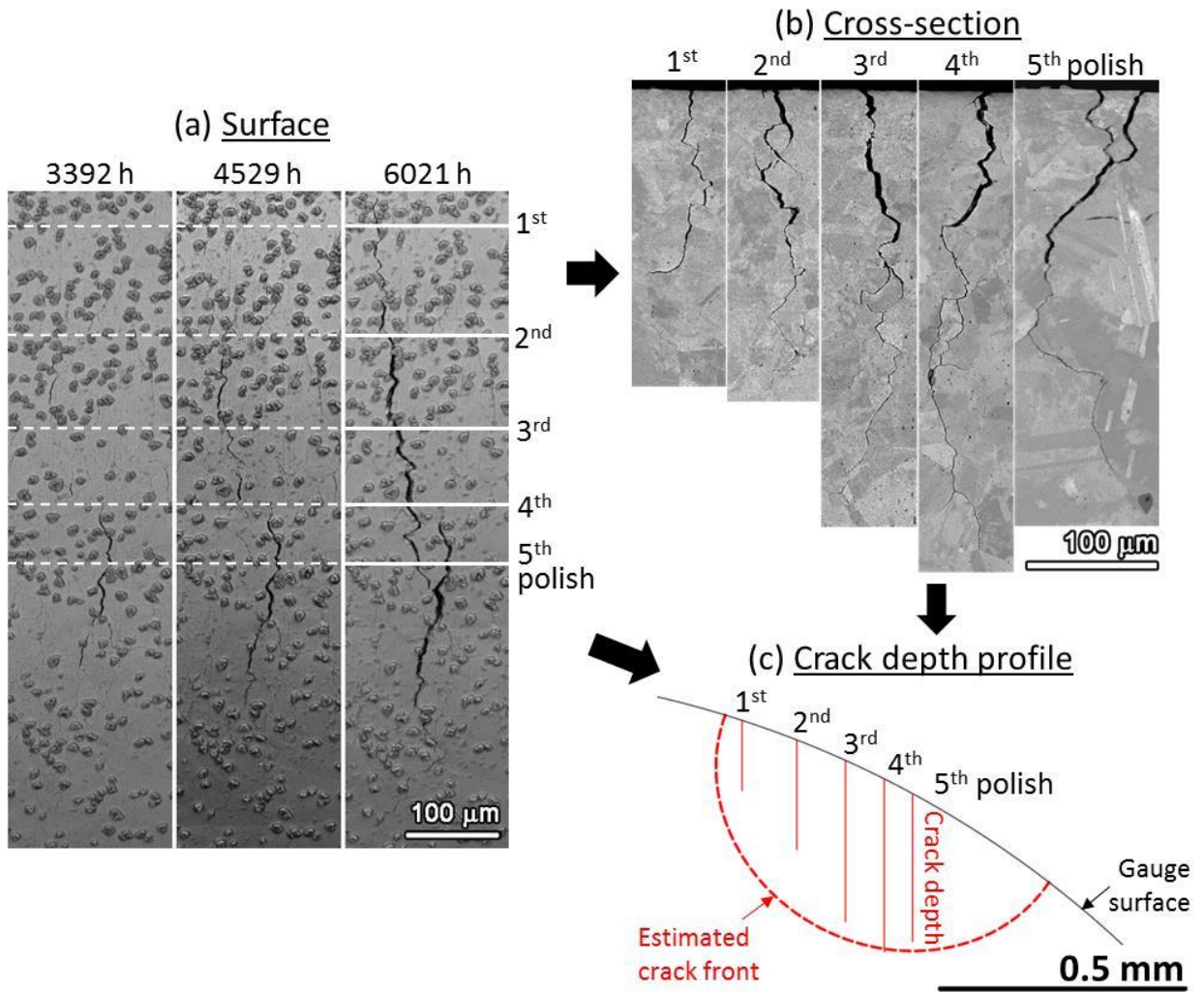
Figure 30.  BSE image of the surface (a) and cross-section (b) morphology for a crack observed in AR plate specimen IN013 with solid lines marking the position of individual cross-sections and the thickness removed after serial polish.  Dashed lines are added to facilitate viewing the crack evolution on the surface near the positions of serial polish after conclusion of the test. Corresponding crack depth profile obtained by correlating crack depth measured in cross-section and the position of the cross-section plane on the surface after each polish is provided in (c).
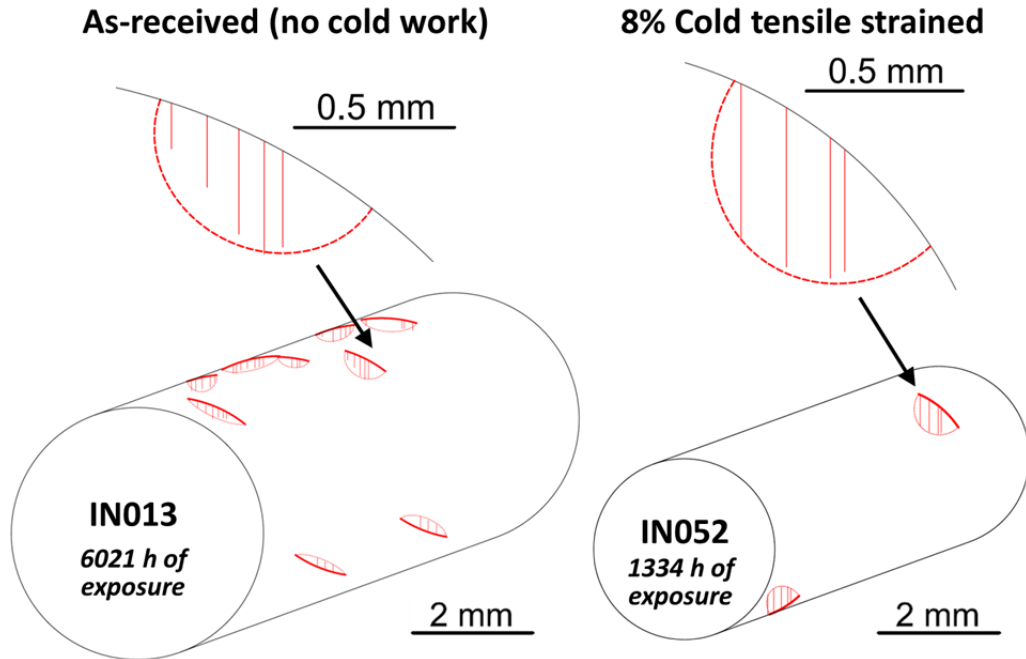
Figure 31. Position and depth profile of selected large cracks observed in the gauge section in an AR and an 8%CTS specimen from the plate heat NX6106XK-11.
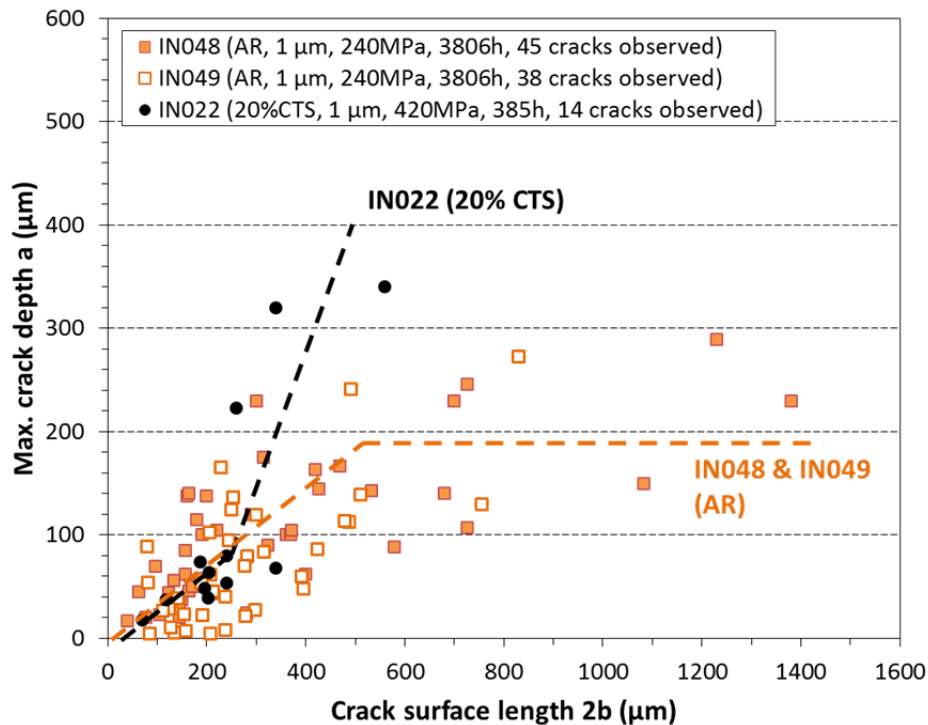


Figure 32. Distribution of maximum depth as a function of surface length for all cracks observed in the 20%CTS specimen IN022 and two AR specimens IN048 and IN049 from the alloy 600 service CRDM heat M3935. Dashed lines are showing the trend of the data distribution.
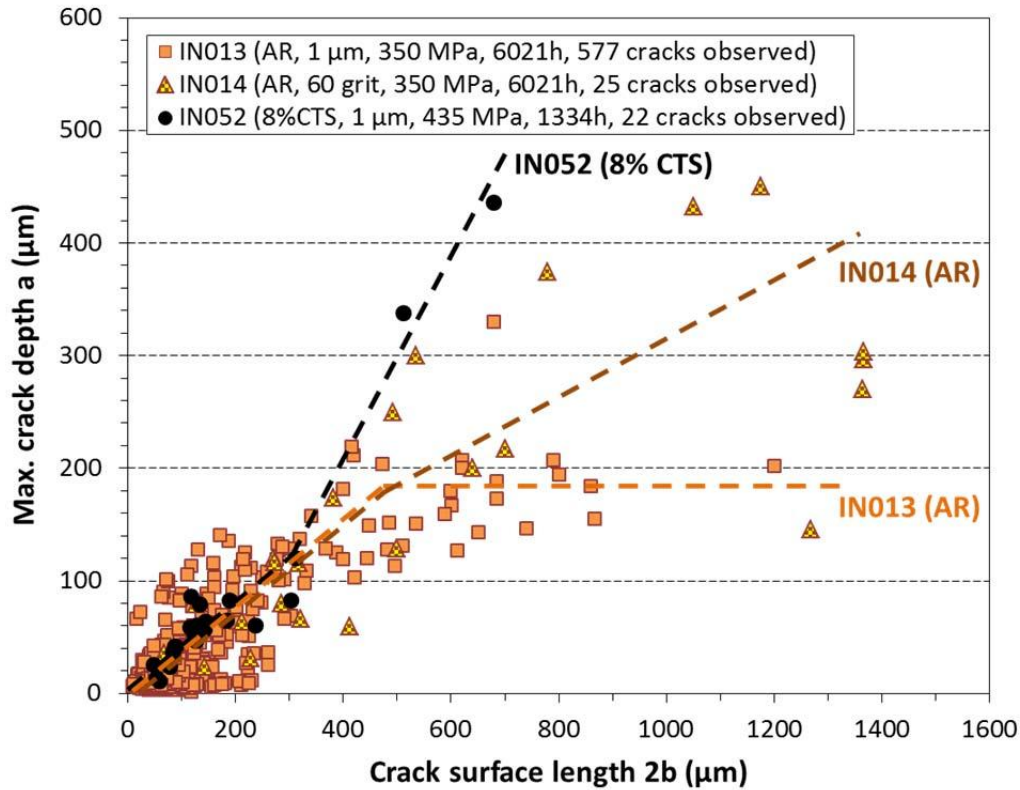
Figure 33. Distribution of maximum depth as a function of surface length for all cracks observed in the 8%CTS specimen IN052, the 1 μm AR specimen IN013 and the 60 grit AR specimen IN014 from the alloy 600 plate heat NX6106XK-11. Dashed lines are showing the trend of the data distribution.

IGA and small cracks on the gauge surfaces of the ground samples were much more difficult to identify due to high surface roughness. However, large cracks became observable by the time SCC initiation was detected. The typical morphology of the large cracks on the surface and in cross-section for ground specimens is shown in Figure 34. Measurements suggest that the shape of cracks is consistent with those observed in the polished samples (Figure 33). It was also observed that the nanocrystalline surface layer was heavily oxidized (Figure 3) and may occur as a precursor to the formation of deep cracks.
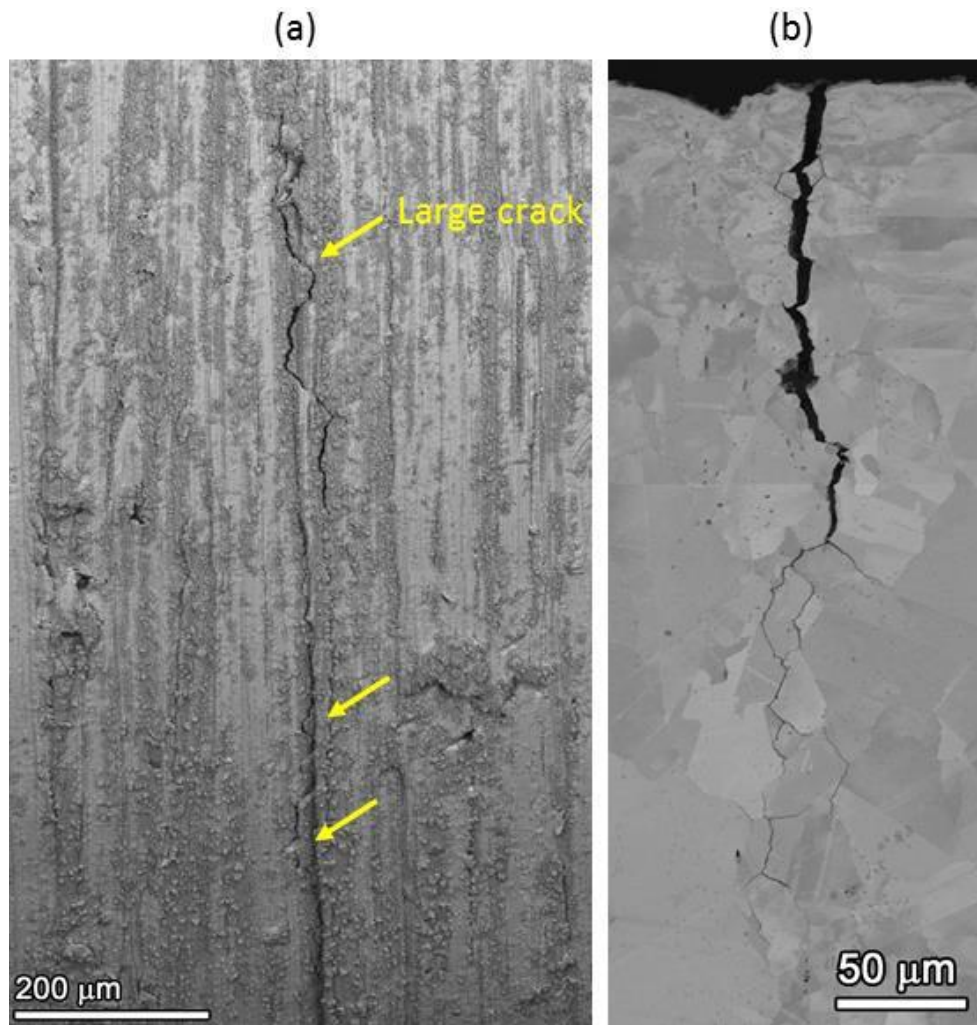
Figure 34. Typical morphology of a large crack on the surface (a) and cross-section (b) of IN014, a 60-grit ground finish plate specimen.

*Discussion*

Correlation of SCC Initiation to DCPD Response

A variety of definitions have been proposed for "SCC initiation" ranging from microscopically small cracks that are usually less than one grain diameter to larger ones that can be detected by non-destructive examination (typically >1 mm long) [14]. In this study, SCC initiation has been based on in-situ DCPD response combined with insights from microstructural characterizations.

A common feature to all the alloy 600 materials that have been examined is for extensive IGA to form on high-energy grain boundaries intersecting the surface with some of these converting to shallow IG cracks. DCPD is not sufficiently sensitive to detect this precursor damage evolution for the current specimen design. In order for DCPD to detect initiation, the cracking component of the signal must be discernable above the component due to creep. This can be accomplished in two ways. The first is that the increase in DCPD voltage due to a unit change in crack length would have to be very large. A slow growing crack with this attribute would be readily detected above the creep signal. Alternatively if the increase in DCPD voltage due to a unit change in crack length is small, then crack growth would have to be rapid enough to cause a sufficient increase in the signal to be detectable above creep. Since the microstructural investigations show that extensive crack nucleation and short crack growth occurred before initiation was detected by DCPD, it is thought that this latter scenario best describes what is taking place during the current tests and that the crack growth rate has to be sufficiently high before it can be detected. This behavior can be seen in Figure 23(a), where the high-strength CW specimen that undergoes rapid SCC growth exhibited a very distinct initiation point and rapid transition. Quite differently, the AR specimens with lower strength and lower SCC propagation showed a very gradual transition to an increasing slope (Figures 23b and 25) or exhibited a DCPD jump (Figures 23c and 24b). A number of factors may play a role in the varied response observed in the AR and CW specimens, but two factors are believed to be important: (1) the highly CW materials are tested at a higher applied stress (equivalent to its yield stress) and (2) SCC growth rates increase with the degree of cold work particularly at low $K$ levels. As a result, the transition from a nucleated surface crack to long crack growth is much easier for the highly CW materials under a higher applied stress.

The crack depth distribution as a function of surface length of IN014 and IN052 in Figure 33 shows one or a few cracks were generally identified as having distinctively greater depth than the others. Therefore it seems reasonable to consider that the DCPD detection of SCC initiation is associated with the onset of faster and continuing propagation of one or a few dominant cracks. The formation of a dominant crack is likely due to a combination of locally unique microstructural and specimen stress factors, which may interact and change as the crack evolves until a critical size is reached, producing a $K$ that prompts a higher CGR. What is less clear is the cracking behavior associated with the DCPD jump observed in the AR material. Since this phenomenon usually takes place between two consecutive DCPD readings which are ~20 s apart

(see Figures 23c and 24b), it likely indicates a large unit change in microstructure or crack length as discussed in the previous paragraph. A variety of microstructural processes representing a strain pulse or a rapid increase in crack dimension could account for the DCPD jump. One possible explanation is the slow formation and rapid release of dislocation pile-ups as localized strain propagates from one grain to the next, producing a strain burst that eventually stops due to work hardening [15]. Another is that the DCPD jump may represent a strain burst that could occur as dislocations overcome solute pinning that is known to occur in alloy 600 at elevated temperature. In either case, crack growth and coalescence could have played an important role in driving up stress and the local $K$. In Figure 30, it is shown that a ~20 μm long uncracked grain boundary section between the 4th and 5th polish in IN013 at 4529 h had become the deepest portion of a large crack at 6021 h after coalescence, reaching a depth of ~350 μm. Such a rapid breakage of ligament between cracks could possibly trigger a widespread of dislocation avalanches in the cross section of the specimen and lead to strain bursts. Further investigation is needed to fully understand the effects of coalescence on SCC initiation and DCPD response. In addition, the depth of large cracks appear to become saturated in Figures 32 and 33 after reaching ~200 μm in the two specimens IN013 and IN048 which exhibited a strain jump. It is therefore concluded that the strain jump observed in these non-CW specimens may not be true indication of SCC initiation, and instead an upward trend in strain rate may be the more appropriate indicator of SCC initiation.

Correlation of SCC Initiation to Stress Intensity

Since IG cracks of significant depth have been observed in all the characterized AR and CW specimens, consideration has been given to the relationship between crack geometry and the local $K$. According to a number of FEM studies [16-18], the $K$ along the crack front of a thumbnail surface crack growing through a rod under tension can be estimated by assuming an elliptical crack shape and using the following equation:

$$K = F\sigma\sqrt{\pi a} \quad (4)$$

where $F$ is a correction factor calculated by FEM based on the geometry of relative crack depth, crack aspect ratio and relative position along the crack front from the crack center. Since the cracks observed in this study can be approximated as elliptical (Figures 30 and 31), preliminary $K$ estimates were made using measured crack geometries and $F$ values obtained FEM studies. Calculation results of $K$ at the center of the largest crack observed in selected specimens are summarized in Table 5. The variation in $K$ is due to slightly different $F$ values produced by each of the FEM studies. These results suggest that the crack dimensions and resultant $K$ at which SCC initiation becomes discernable by DCPD is ~10 MPa√m. This is very close to the threshold $K$ of 9 MPa√m identified by several French researchers first for SCC growth [19] and then for SCC initiation using a combination of constant load and constant extension rate tests [20, 21]. It is therefore considered that the transition from slow development of IGA and small cracks to

more rapid SCC propagation takes place when a few large cracks grow to a size that is sufficient to trigger the critical $K$ (~10 MPa√m in this case).  Finally, this transition signifies the onset of "practical" initiation with cracks reaching a size where stable SCC growth occurs.  This more readily occurs in higher strength materials at a higher applied stress for the reasons just described and is pictorially represented in Figure 35.  This description of SCC initiation is consistent with that given by LeHong [21] for a combination of constant load and constant extension rate tests.

Table 5.  Estimated $K$ (MPa√m) at the front center of the largest crack observed.

| Spec. ID | Heat | CW level | Applied load (MPa) | DCPD response | Crack depth (µm) | Crack surface length (µm) | $K$ at crack front center (MPa√m)* |
|---|---|---|---|---|---|---|---|
| **IN048** | Service CRDM | AR | 240 | Strain jump | 289 | 1567 | 6.5–7.1 |
| **IN049** | Service CRDM | AR | 240 | No initiation | 243 | 829 | 5.2–6.0 |
| **IN022** | Service CRDM | 20%CTS | 420 | **Initiated** | 342 | 560 | **9.0–9.8** |
| **IN013** | Plate | AR | 350 | Strain jump | 330 | 748 | 7.8–8.9 |
| **IN014** | Plate | AR | 340 | **Initiated** | 412 | 1346 | **10.0-11.4** |
| **IN052** | Plate | 8%CTS | 435 | **Initiated** | 440 | 828 | **10.4–12.2** |

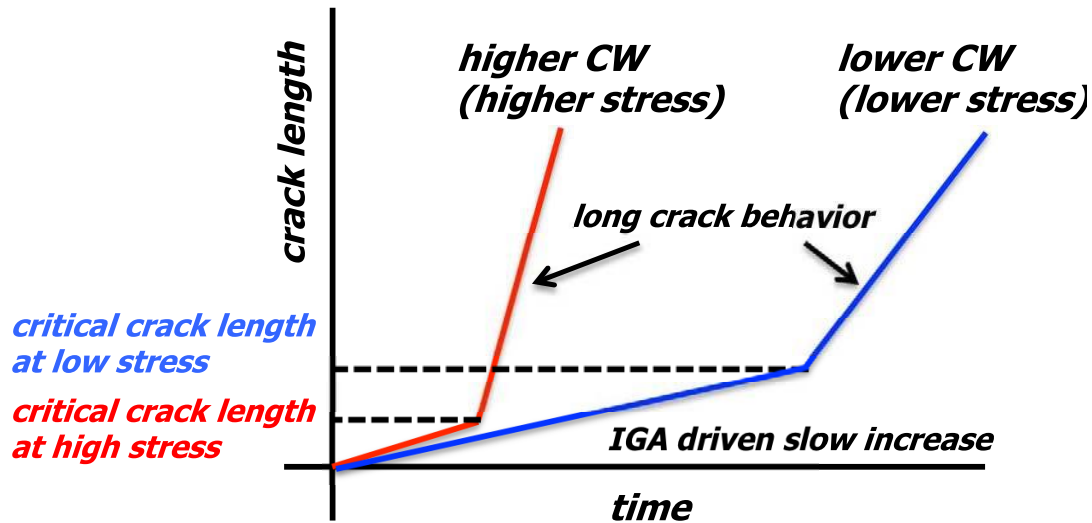*The $K$ values were estimated using F values given in three publications [16-18].



Figure 35.  Qualitative representation of possible differences in initiation response between a material in a low and a high CW condition that are tested at their yield stress.

Effect of Cold Work on SCC Initiation

A sufficient number of tests have been completed to show key trends of SCC initiation time for alloy 600 specimens as a function of cold work.  The relationship between DCPD-indicated SCC initiation time and applied stress is shown in Figure 36, while initiation time versus the level of cold work is plotted in Figure 37.  Dashed lines in the plots are meant to bound the data and aid in visualization of the trend in initiation response.  In a previous study on multiple alloy 600 heats, Etien et al. [6] suggested that SCC initiation time is strongly affected by plastic strain but not by stress.  While the initiation times obtained in this study are consistent with those reported in [6], the data also show an apparent dependence on applied stress that is identical to the dependency of initiation time on plastic strain.  Materials with 7-8%CTS have initiated in less than 2200 hours, and higher levels of cold work have caused only a small additional reduction. Data on the non-CW specimens suggest that initiation time in these AR materials range from ~6000 hours and above, roughly 3 times higher than the 7-8%CTS material.  Post-test examination revealed that the dominant cracks in the CW materials had reached a comparable or longer depth within a much shorter exposure time as those found in the AR materials (Figures 32 and 33) suggesting the growth rate of short cracks had been greatly enhanced by cold work.  This is consistent with a number of studies on SCC propagation in alloy 600 exposed to PWR primary water, where low-levels of cold work (5-12%) have increased crack growth rate by a few orders of magnitude [11, 22, 23].
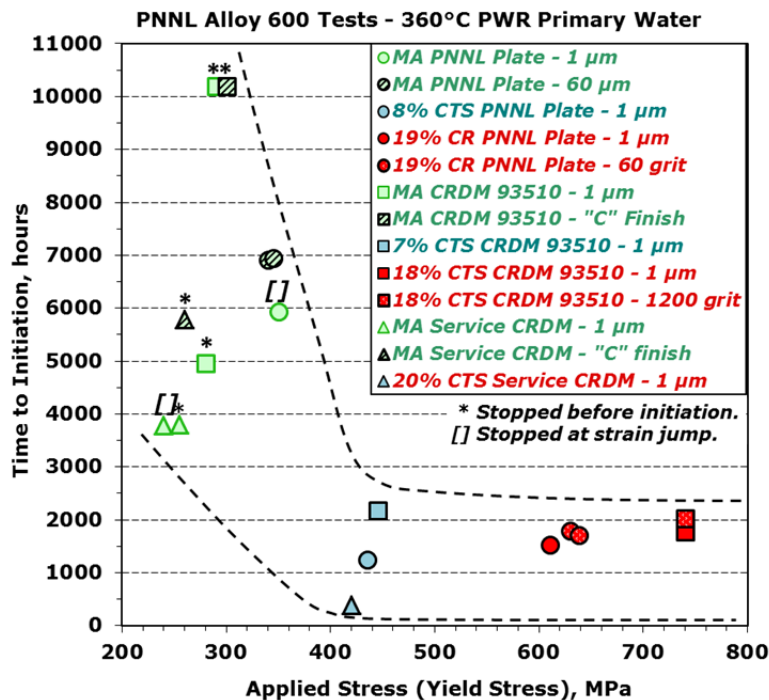


Figure 36.  Measured SCC initiation time as a function of applied stress.  Dashed lines are meant to bound the data and aid in visualization of the initiation response.
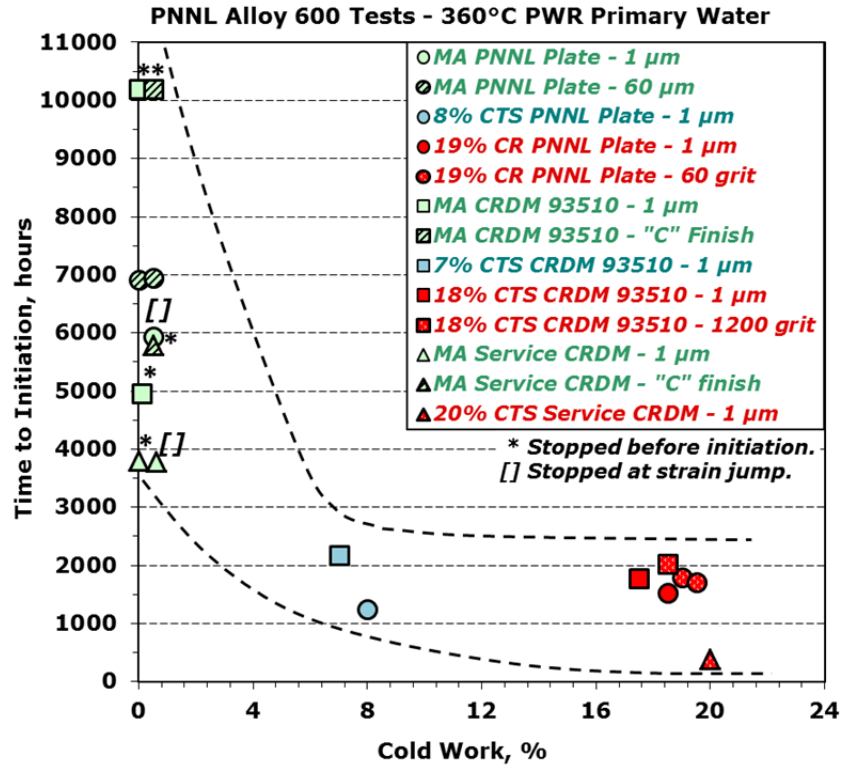
Figure 37. Measured SCC initiation time as a function of % cold work. Dashed lines are meant to bound the data and aid in visualization of the initiation response.

Effect of Surface Finish on SCC Initiation

Service experience suggest that SCC initiation first occurs on highly stressed, heavily damaged or ground surfaces, which is believed to be caused during component assembly activities or from loose part impacts during reactor operation [24-26]. This surface damaged region can include a thin nanocrystalline layer with extreme levels of deformation and a work-hardened layer below it that can have high levels of deformation but more closely resembles the bulk grain shape. This work-hardened layer is typically produced at lower temperatures and is often effectively a CW region. The depth of the work-hardened layer depends strongly on how the deformation was introduced, and the total thickness of the surface damaged region may have a strong influence on SCC initiation time [24, 27, 28]. A shallow cold work layer (<20 µm deep) is reported to have little effect on initiation time whereas a thick surface damaged layer can increase crack density, allow for rapid crack extension deeper into the material and reduce SCC initiation time [24, 27]. For the present work, the surface damaged layer from grinding was found to be less than 50 µm deep in the AR alloy 600 specimens suggesting that it should have little effect on initiation time. In fact, the direct comparisons of data in Table 4 suggest that the ground specimens initiate slightly after the polished specimens. This trend for longer initiation times may simply be data scatter, since the thin damage layer is not expected to have a strong effect on SCC initiation time.

49

However, comparison of the near-surface corrosion microstructures between highly polished samples and ground samples indicate that additional time may be required for corrosion and cracking to proceed through the ground region (Figure 3). It is shown that in the ground sample, corrosion occurred almost exclusively in the thin layer of recrystallized nanocrystalline grains produced by aggressive grinding. This is consistent with various experimental observations obtained on both stressed and unstressed alloy 600 samples in similar environmental conditions [29, 30]. High-resolution composition analysis revealed a thin film of Cr-enriched oxide on the outer surface of the sample and elevated Cr content in the surface damage layer [29]. Therefore, the deformed nanocrystalline layer not only creates a microstructural barrier (albeit temporary) between bulk grain boundaries and the environment, but may also accelerate Cr diffusion to the surface to produce more protective oxides. In comparison, a highly polished surface ensures that all grain boundaries reaching the surface have direct access to the corrosion environment and IGA can begin immediately on exposure.

**Update of SCC Initiation Test Results on Alloy 600**

Previous investigation on SCC initiation behavior of three MA alloy 600 heats in simulated PWR primary water provided an integrated view of SCC initiation encompassing IGA, crack nucleation, short crack growth, crack coalescence and propagation of fully developed cracks. The effect of cold work was assessed and the influence of surface finish was examined. More recent research measured SCC initiation times on several 15%CF alloy 600 in collaboration with an international round robin to analyze lab-to-lab variability and investigate temperature effects. Three alloy 600 heats (MA plate heat NX6106XK-11 provided by PNNL, SA plate heat 31907 provided by GE/EPRI, and SA plate heat 11415 provided by Rolls Royce) were selected for this evaluation. In addition, another MA plate heat 33375-2B provided by KAPL was tested in collaboration with a joint NRC/EPRI program. Experiments have now been completed on 27 additional specimens with details summarized in Table 6 and bring the total number of tests on alloy 600 materials to 44 (including prior tests shown in Table 4). The SCC initiation response and characterization results for the new specimens will be detailed in the following sections.

*SCC Initiation Tests at 360$^o$C PWR Primary Water*

MA+15%CF Alloy 600 Plate Heat NX6106XK-11

Among the total 16 tested specimens from the alloy 600 plate heat NX6106XK-11, IN013-018, IN052 (Table 4) and IN146-148 (Table 6) were tested in smaller SCC initiation systems where three specimens were loaded in series. This set up enabled more flexibility in test control and most tests were stopped immediately (within hours) after an increasing slope in strain rate was detected by DCPD. The rest of the specimens (IN156-157, IN160-161, IN164-165 in Table 6) were tested simultaneously with six other alloy 600 specimens in a larger SCC initiation system that was equipped with three load trains (each can handle up to 12 specimens) especially designed for long-term SCC initiation testing. They can sustain the load even when certain specimens fractured during the test to allow the test to continue for the other specimens loaded in the same string. As described earlier, this was achieved through interaction with software programs to partially unload the system and let the initiated specimen fail at a reduced load when a sharp increase in strain is detected by DCPD. For this specific test, a small strain overload occurred after ~1100 h in the test during the rapid failure of a single alloy 600 specimen. The specimens were brought back to the previous target load, but this was below the new material yield stress resulting from the small strain overload. After 1772 hours of exposure at this condition without DCPD detection of crack initiation in any specimen, it was decided to increase the load and again reach an applied stress equal to the yield stress based on the DCPD response of the monitored specimens. The new applied stress to reach the specimen yield stress was ~595 MPa, requiring a ~9% higher load than when the test was started. SCC initiation was detected

by DCPD in the six MA+15%CF alloy 600 plate specimens soon after the new yield stress was reached and all the specimens initiated in the following ~1800 h.  The adjusted (total test time at yield stress) SCC initiation time of these specimens are shown in Table 6.

Table 6.  Additional PNNL Alloy 600 SCC Initiation Testing Results (09/2017).

| Spec. ID | Material Type | Heat Number | CW level | Finish | Temp (°C) | Applied Stress‡ (MPa) | Time to SCC initiation (h) |
|---|---|---|---|---|---|---|---|
| IN146 | MA Plate | NX6106XK-11 | 15%CF | 1 μm | 360 | 548 | 396 |
| IN147 | MA Plate | NX6106XK-11 | 15%CF | 1 μm | 360 | 535 | 385 |
| IN148 | MA Plate | NX6106XK-11 | 15%CF | 1 μm | 360 | 548 | 219 |
| IN156* | MA Plate | NX6106XK-11 | 15%CF | 1 μm | 360 | 550-592 | 2790 |
| IN157* | MA Plate | NX6106XK-11 | 15%CF | 1 μm | 360 | 550-595 | 2830 |
| IN160* | MA Plate | NX6106XK-11 | 15%CF | 1 μm | 360 | 550-592 | 1230 |
| IN161* | MA Plate | NX6106XK-11 | 15%CF | 1 μm | 360 | 550-595 | 1450 |
| IN164* | MA Plate | NX6106XK-11 | 15%CF | 1 μm | 360 | 550-592 | 1480 |
| IN165* | MA Plate | NX6106XK-11 | 15%CF | 1 μm | 360 | 550-595 | 2370 |
| IN206 | MA Plate | NX6106XK-11 | 15%CF | 1 μm | 325 | 534 | 1465 |
| IN207 | MA Plate | NX6106XK-11 | 15%CF | 1 μm | 325 | 540 | 2580 |
| IN208 | MA Plate | NX6106XK-11 | 15%CF | 1 μm | 325 | 528 | 1680 |
| IN151 | SA Plate | 31907 | 15%CF | 1 μm | 360 | 350 | 290 |
| IN152 | SA Plate | 31907 | 15%CF | 1 μm | 360 | 350 | 342 |
| IN153 | SA Plate | 31907 | 15%CF | 1 μm | 360 | 350 | 354 |
| IN209 | SA Plate | 31907 | 15%CF | 1 μm | 325 | 364 | 1220 |
| IN210 | SA Plate | 31907 | 15%CF | 1 μm | 325 | 354 | 1350 |
| IN211 | SA Plate | 31907 | 15%CF | 1 μm | 325 | 351 | 1040 |
| IN203 | SA Plate | 11415 | 15%CF | 1 μm | 360 | 416 | 880 |
| IN204 | SA Plate | 11415 | 15%CF | 1 μm | 360 | 421 | 890 |
| IN205 | SA Plate | 11415 | 15%CF | 1 μm | 360 | 412 | 840 |
| IN154* | MA Plate | 33375-2B | 15%CF | 1 μm | 360 | 550-574 | 1100 |
| IN155* | MA Plate | 33375-2B | 15%CF | 1 μm | 360 | 550-584 | 1480 |
| IN158* | MA Plate | 33375-2B | 15%CF | 1 μm | 360 | 558 | 120 |
| IN159* | MA Plate | 33375-2B | 15%CF | 1 μm | 360 | 550 | 1025 |
| IN162* | MA Plate | 33375-2B | 15%CF | 1 μm | 360 | 550 | 830 |
| IN163* | MA Plate | 33375-2B | 15%CF | 1 μm | 360 | 550-558 | 1034 |

‡ The applied stress is the yield stress of the specimens at the tested temperature.
* These 12 specimens were tested in collaboration with a NRC/EPRI initiation program in a large SCC initiation system.

The SCC initiation times for all non-CW and CW alloy 600 specimens tested to-date are summarized in Figure 38 as a function of applied stress (i.e. yield stress in this study). Previous data from multiple heats (reviewed in the prior section) have shown that when loaded at yield stress, a slight degree of cold work can significantly promote SCC initiation in alloy 600 whereas higher levels of cold work do not necessarily lead to additional reduction in initiation time. While the new data obtained from the MA+15%CF alloy 600 plate heat specimens agrees with this trend, unexpected low SCC initiation times ranging from ~220-400 h were observed in specimens IN146-148 as shown in Figure 39. All of these three specimens were machined from a single region of the plate. In comparison, the other six 15%CF specimens (IN156-157, IN160-161, IN164-165) exhibited much longer, more consistent SCC initiation times with prior tests on the material in other cold work conditions (Figures 38 and 40). This revealed that large difference in SCC initiation response can occur in the same material at similar cold work levels and similar surface conditions. In order to investigate the cause behind this phenomenon, detailed characterizations were carried out on these two groups of specimens.
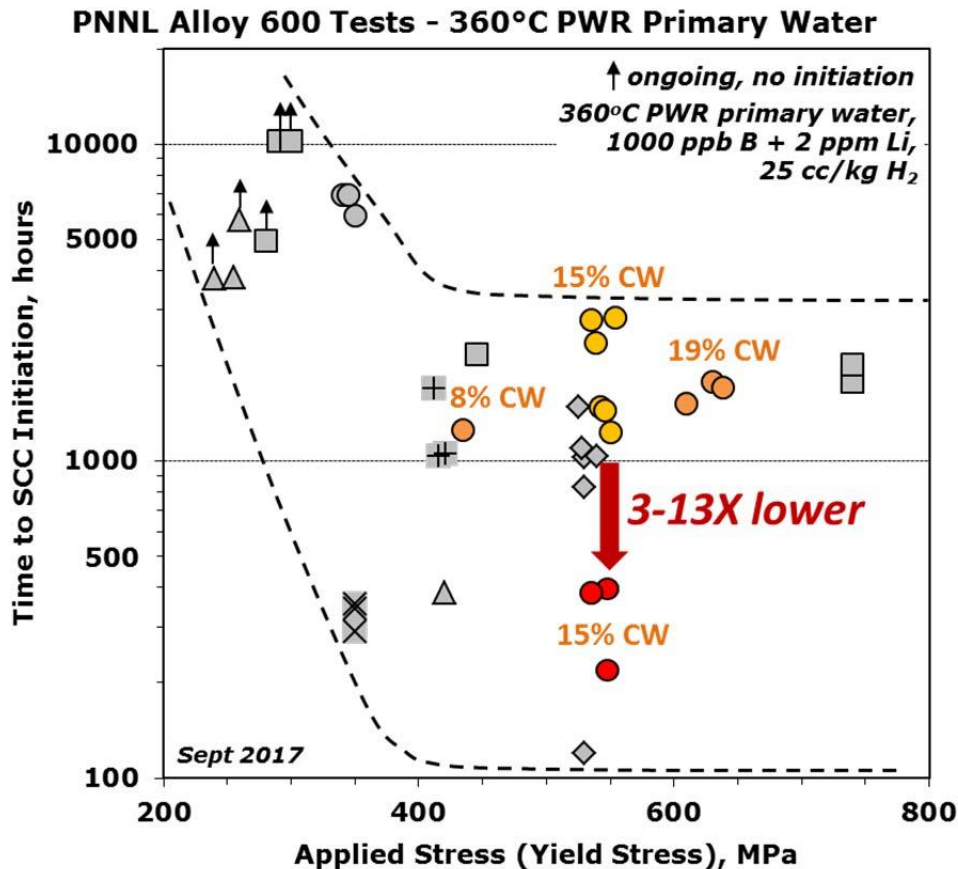


Figure 38. Measured SCC initiation time as a function of applied stress. Dashed lines are meant to bound the data and aid in visualization of the initiation response. The data from the MA alloy 600 plate heat NX6106XK-11 are highlighted.
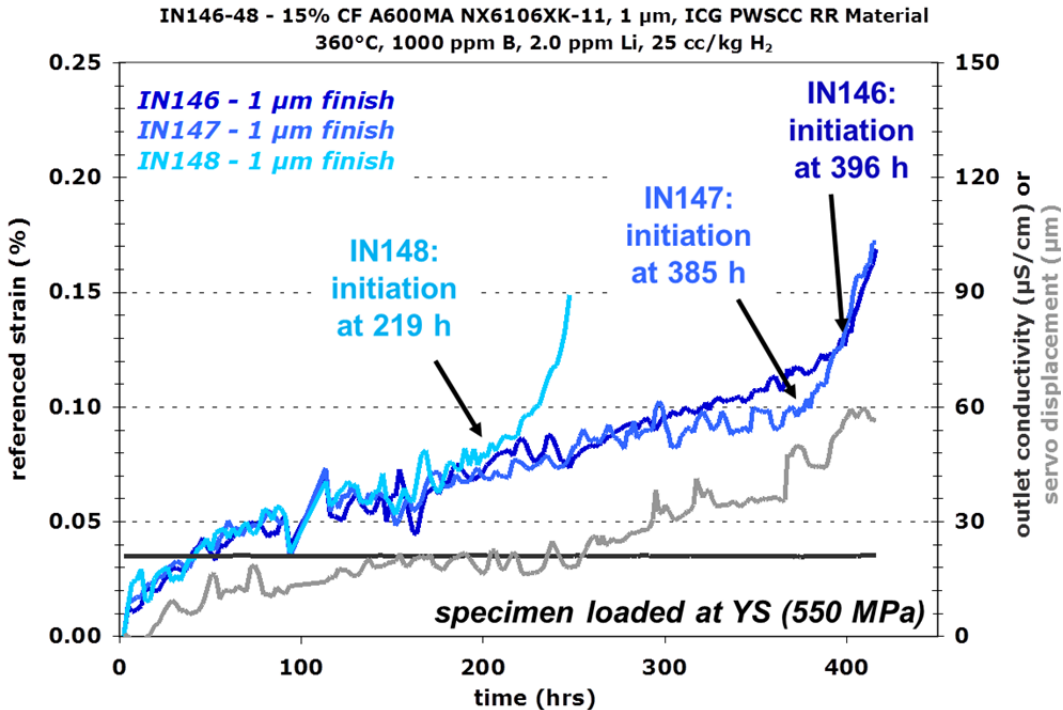
Figure 39.  Referenced DCPD strain response showing early initiation for the 15%CF specimens IN146-148 from the MA Alloy 600 plate heat NX6106XK-11 tested at their yield stress at 360°C.

Post-test SEM examinations first started with the three specimens IN146-148 that showed unexpectedly early SCC initiation.  The results revealed that the early initiation can be associated with crack nucleation and growth occurring on *large elongated grains*.  As shown in Figure 41, the primary crack in IN148 nucleated along the grain boundary of a large elongated grain in a banded region.  A similar observation was found for IN146 where only one large crack was observed.  The morphology and shear bands associated with this crack indicate that it first formed along one side of a large elongated grain and then extended further as the test continued (Figure 42).  This was confirmed by comparing the surface morphology along the crack to that recorded at test interruption after 250 h of exposure.  As shown in Figure 43, while IGA can be identified along a large number of high energy grain boundaries, only a small fraction of ~60 μm in length along the boundary of the large elongated grain showed a much stronger contrast, indicating that this is the site where crack first nucleated.  The final 15%CF specimen IN147 in the same series showed DCPD detection of initiation at ~385 h and propagated to failure before the test was stopped.  Therefore, microstructural characterization was conducted on the fractured surface instead of the gauge surface for this specimen.  As shown in Figure 44, a large elongated grain protruding into the gauge for ~1 mm in depth was found on the crack plane again highlighting the important role of microstructural inhomogeneity in SCC initiation.
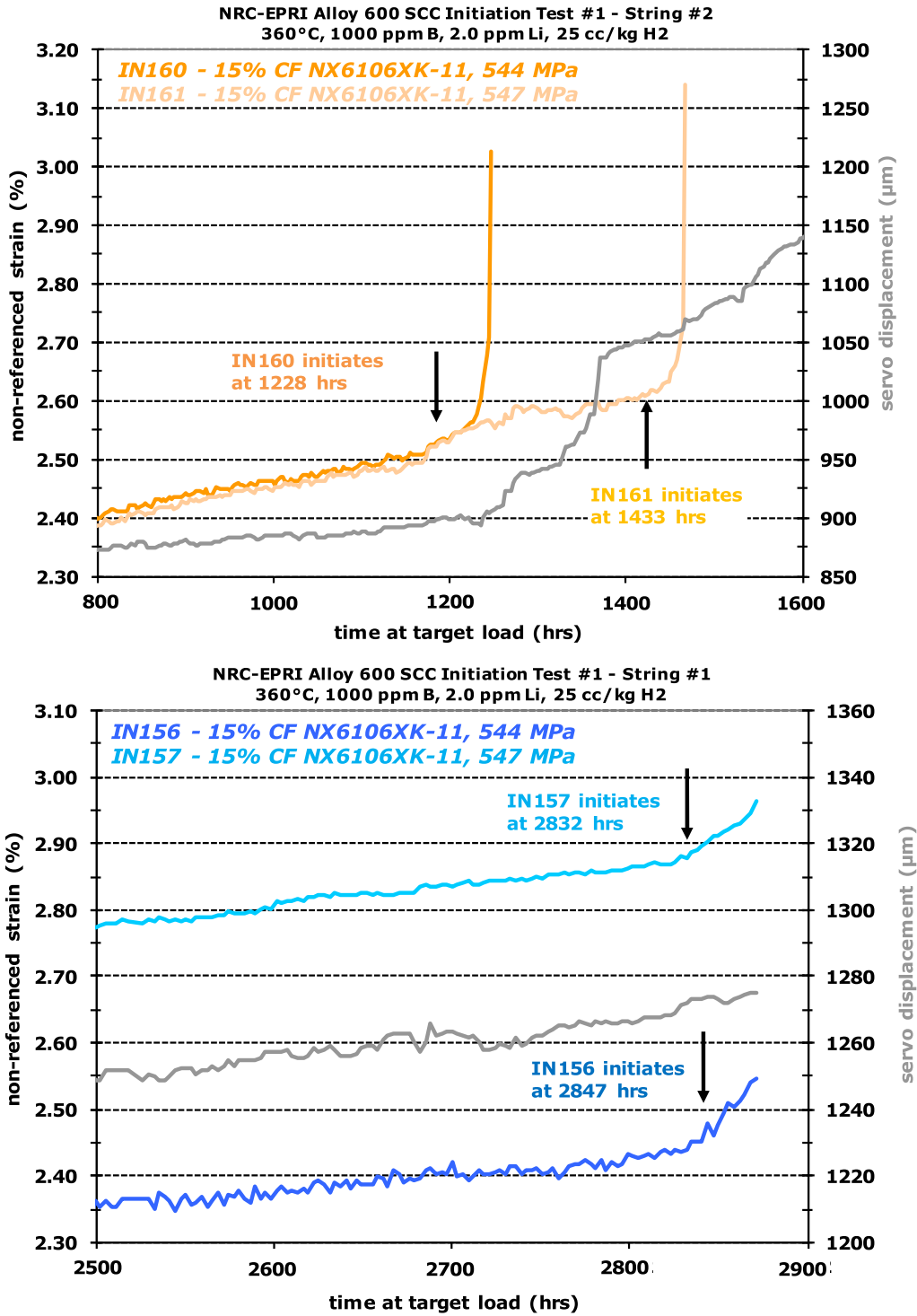
54

Figure 40. Non-referenced DCPD strain response showing SCC initiation for the 15%CF specimens IN156, IN157, IN160 and IN161 from the MA Alloy 600 plate heat NX6106XK-11 tested at their yield stress.
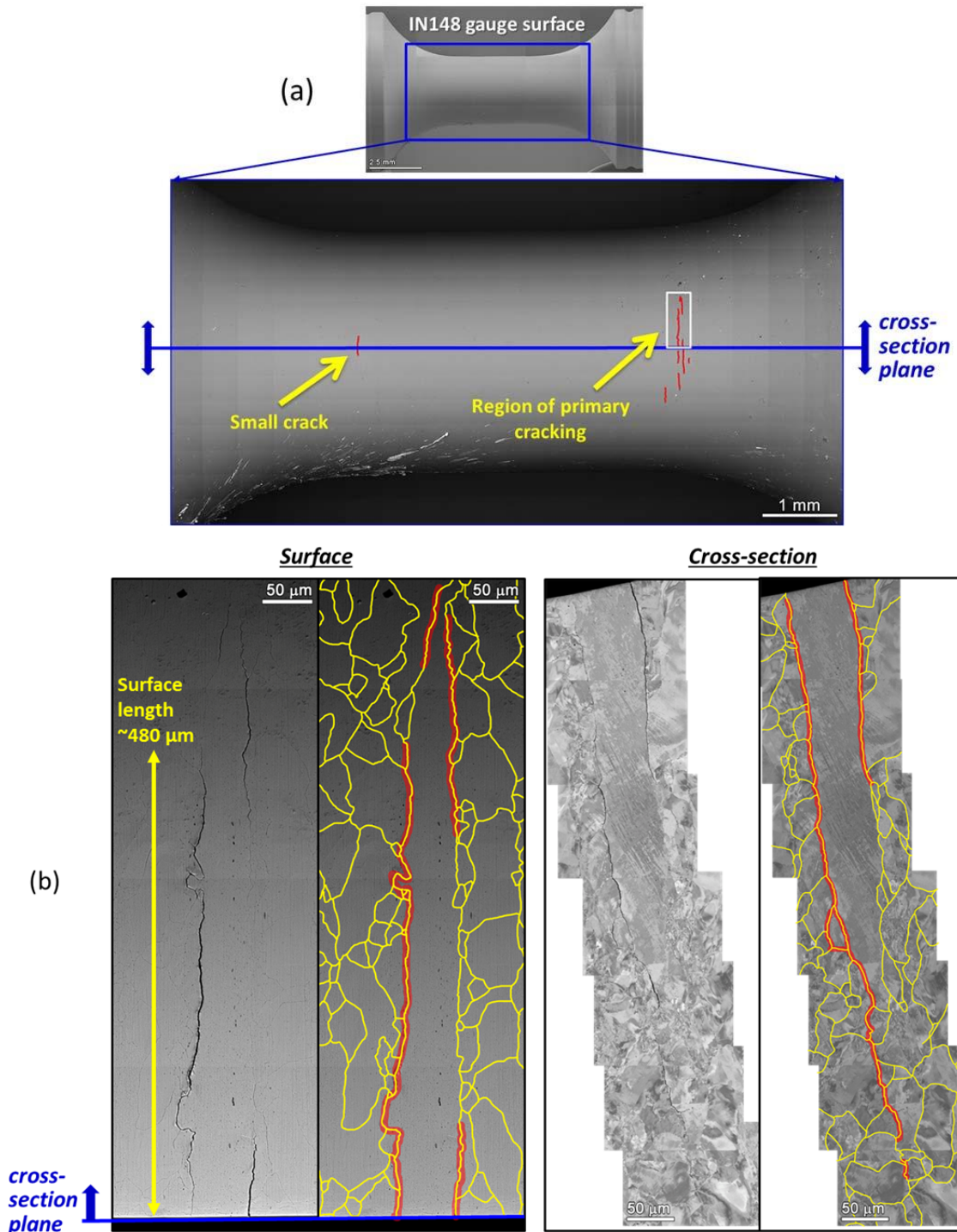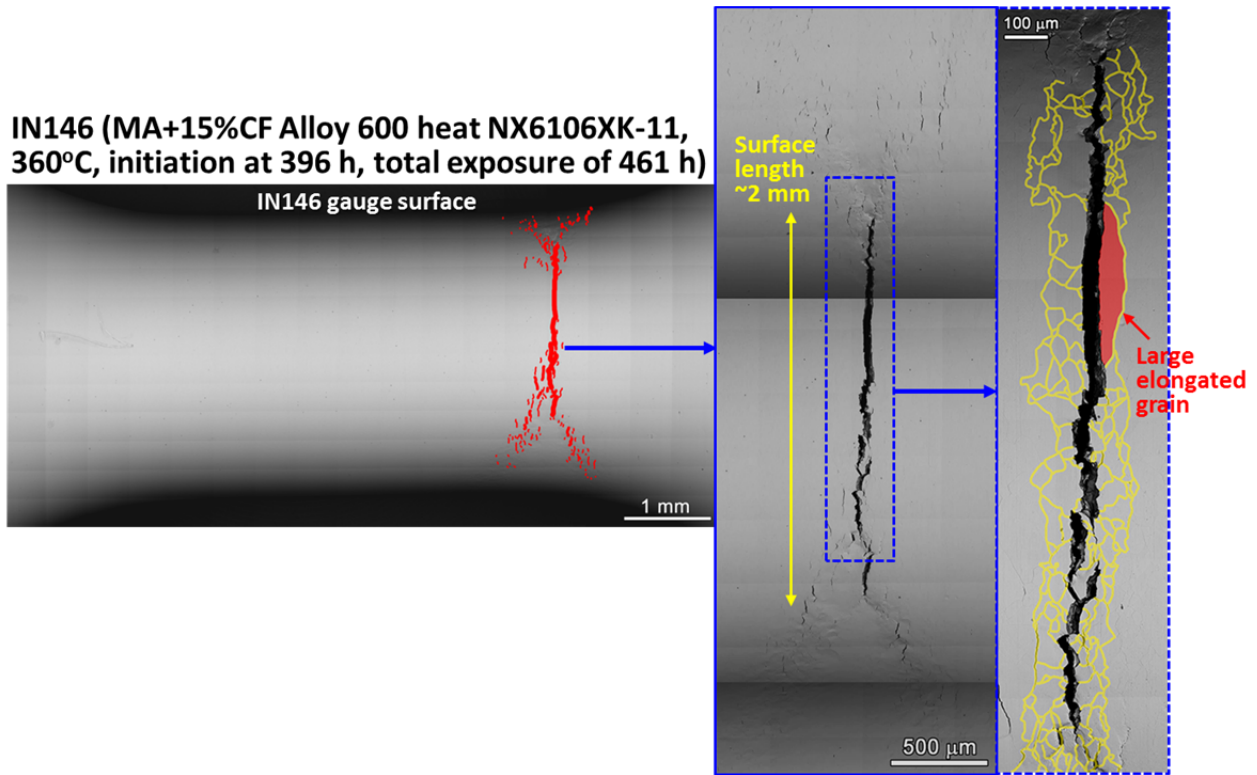
Figure 41.  SEM-BSE imaging of the MA+15%CF alloy 600 plate heat NX6106XK-11 specimen IN148 with DCPD initiation detection at 219 h of exposure at yield stress: (a) crack locations on the gauge surface and (b) the surface and cross-section morphology of the primary crack in the highlighted region in (a).  The cracks are highlighted in red and the grain boundaries are highlighted in yellow.
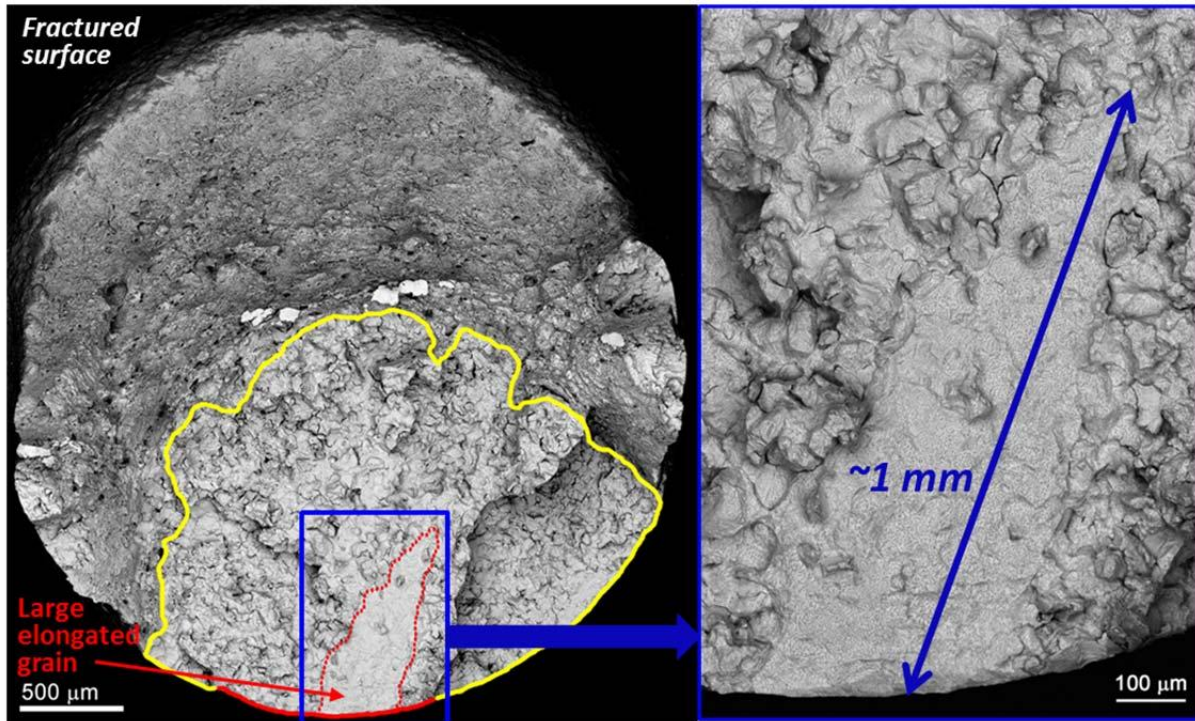
56

Figure 42. SEM-BSE imaging on the gauge surface of the MA+15%CF alloy 600 plate heat NX6106XK-11 specimen IN146 with DCPD initiation detection at 396 h of exposure at yield stress. The primary crack was found to nucleate along an elongated large grain in a banded region where grain boundaries are highlighted in yellow.
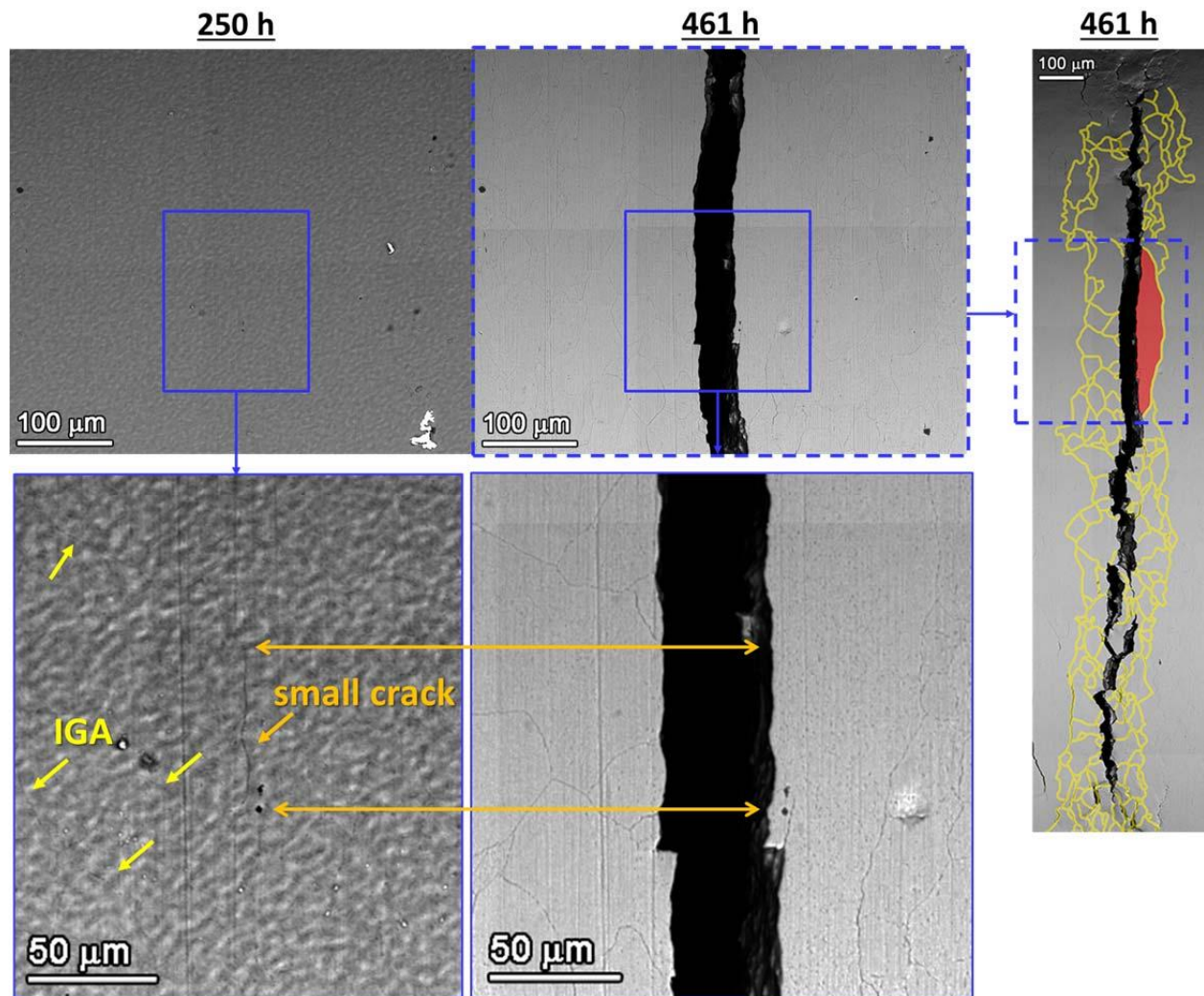
Figure 43.  Evolution of the gauge surface in the vicinity of the large elongated grain of the MA+15%CF alloy 600 plate heat NX6106XK-11 specimen IN146 before (left) and after (right) DCPD initiation detection.  IGA were observed on a large number of high energy grain boundaries (highlighted in yellow) despite of the surface oxides obscuring a clear view. However, only a small crack (highlighted in orange) was found along the boundary of the large elongated grain at 250 h of exposure.

Figure 44. SEM-BSE imaging on the fracture surface of the MA+15%CF alloy 600 plate heat NX6106XK-11 specimen IN147 with DCPD initiation detection at 385 h of exposure at yield stress. The region of IG failure is enclosed in yellow with the primary crack on the surface identified in red. The region of the large elongated grain is outlined using dashed red lines to aid visualization and a zoom-in image of the region is provided on the right side.

SEM examinations were also conducted on the fracture surface of several other 15%CF specimens that underwent significantly longer times of exposure before DCPD-detected initiation with results summarized in Figure 45. The areas of IG failure in these specimens are outlined in yellow. The primary cracks on the gauge surface were identified in red after correlating the fracture surface morphology to gauge surface morphology. This is straightforward because the final cracking process beyond the initial cracks always exhibits obvious plastic deformation typically ~45° off the crack plane on the gauge surface. Large elongated grains were either not observed (IN160) or were present in different morphologies to the surface as those observed in IN146-148. For example, a large elongated grain was found in IN161 with the longitudinal direction along the gauge circumference, resulting in a limited extension (<200 μm) into the gauge. Similarly, a large grain was discovered in IN164 that exhibited only a limited IG extension (<300 μm) from the surface. Four large elongated grains were identified on the fracture surface of IN165, however only two of them (on the left side) extended deeply into the gauge cross-section and they were located on different planes. It is possible that multiple IG cracks nucleated along these large grains retarding short crack growth
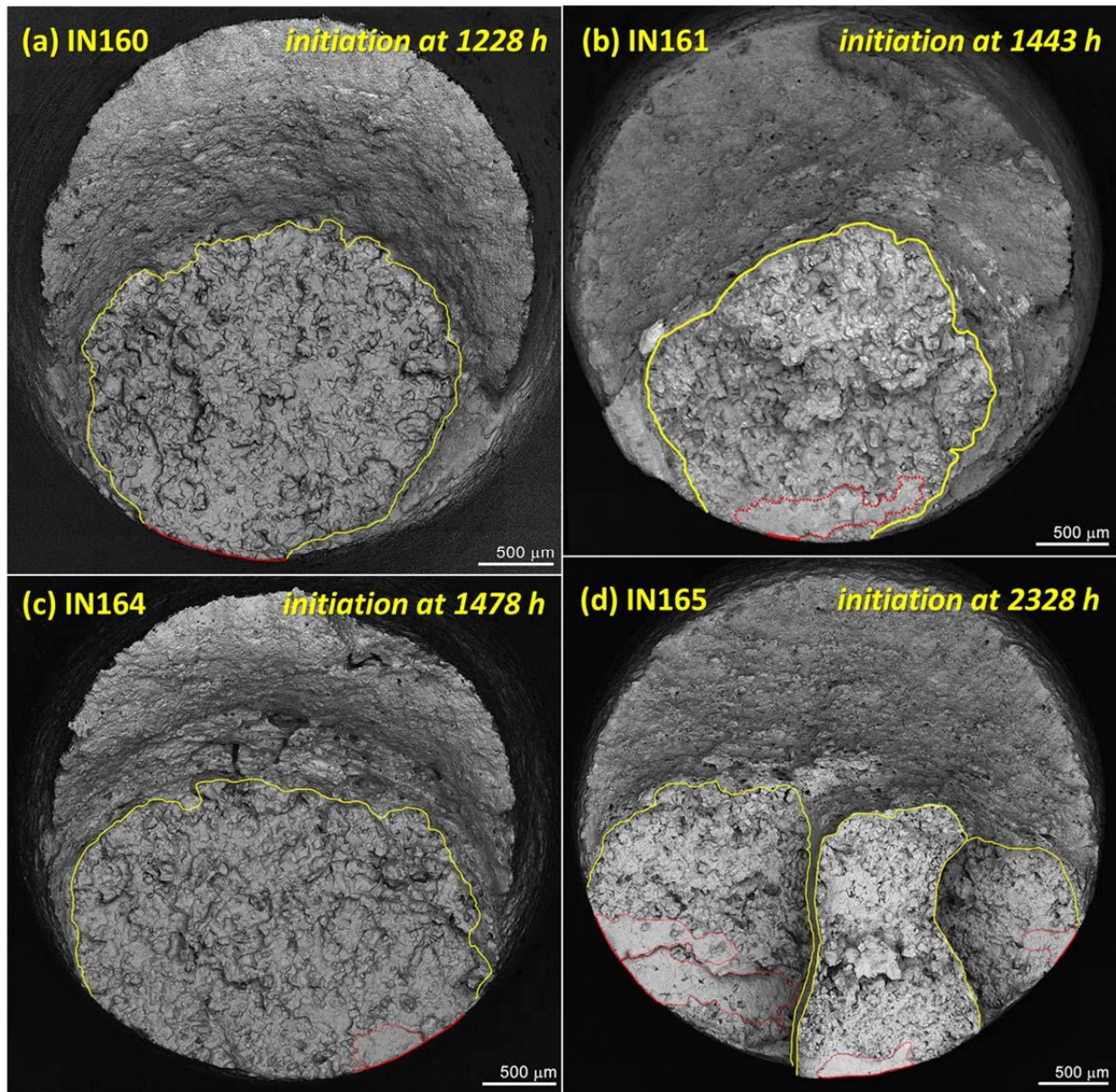
Figure 45.  SEM-BSE imaging on the fracture surface of four 15%CF specimens from the MA alloy 600 plate heat NX6106XK-11 with ascending order in DCPD-detected initiation time.  The region of IG failure is enclosed in yellow with the primary crack on the surface identified in red. The regions of large elongated grain are outlined using dashed red lines to aid visualization when presented.
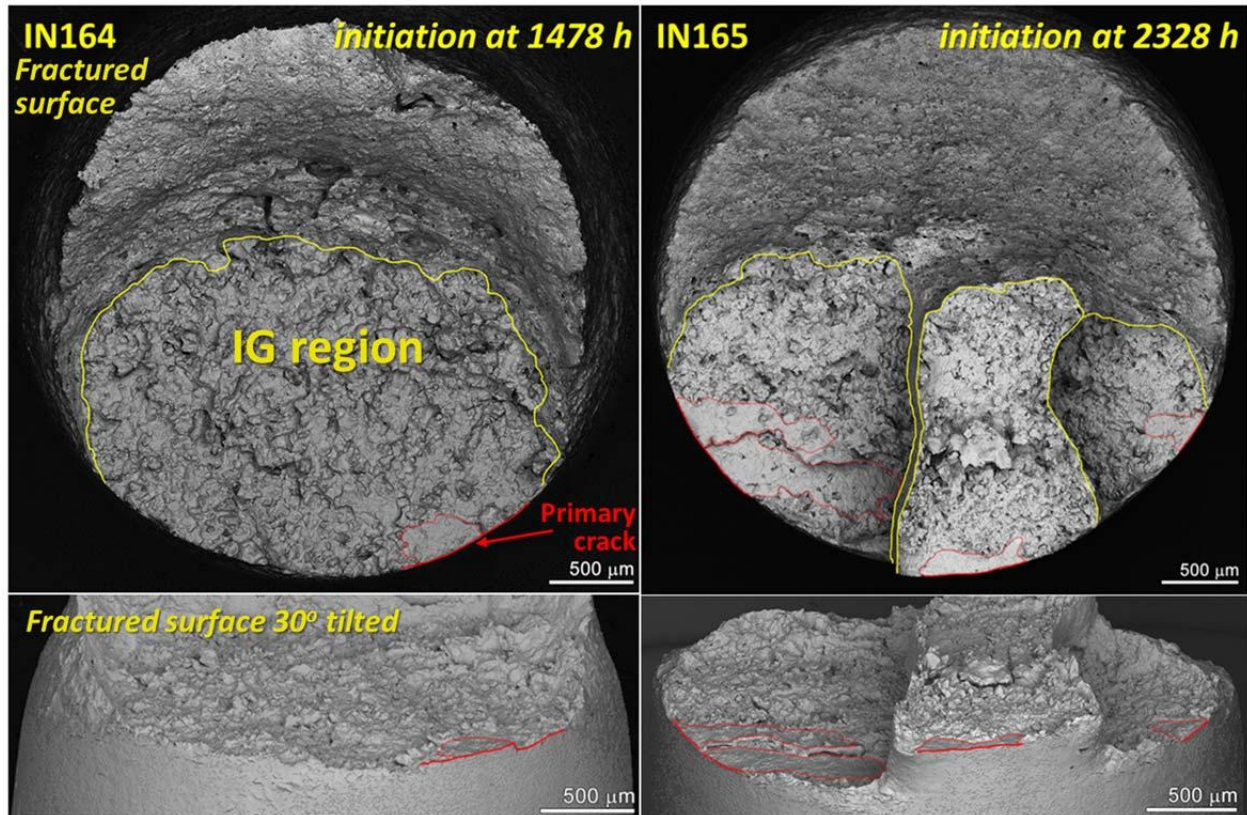
Figure 46.  SEM-BSE montage images of the same fracture surface of IN164 and IN165 shown in Figure 45 at a 30° tilt.  The primary cracks are highlighted in red on the gauge surface with associated large grains identified in dashed lines.

and delaying DCPD detection of initiation until they finally coalesced.  A better indication of the primary crack locations on the IN164 and IN165 specimen gauge surface can be seen in Figure 46.  In comparison, the IN146-148 specimens exhibiting unexpectedly early SCC initiation contained large elongated grains protruding into the gauge with a depth commonly exceeding 500 µm (Figures 41 and 44).  Therefore, it appears that the orientation of large elongated grains is a critical influencing factor for SCC initiation and growth in the 15%CF alloy 600 plate material.  It is likely that when the large grains are oriented preferentially with deep protrusion into the gauge, their grain boundaries can provide a path for early IG crack nucleation and more rapid growth leading to macroscopic SCC initiation.

The reason for the enhanced IGSCC susceptibility at the large grains is uncertain, but several possibilities can be suggested.  First of all, the inhomogeneous grain microstructure may result in more intense localized deformation during cold working and localized stresses during the test.  However, the EBSD on the cross-section of IN148 where the primary crack was observed did not exhibit higher local strains along the boundaries of the large elongated grain (Figure 47).   In
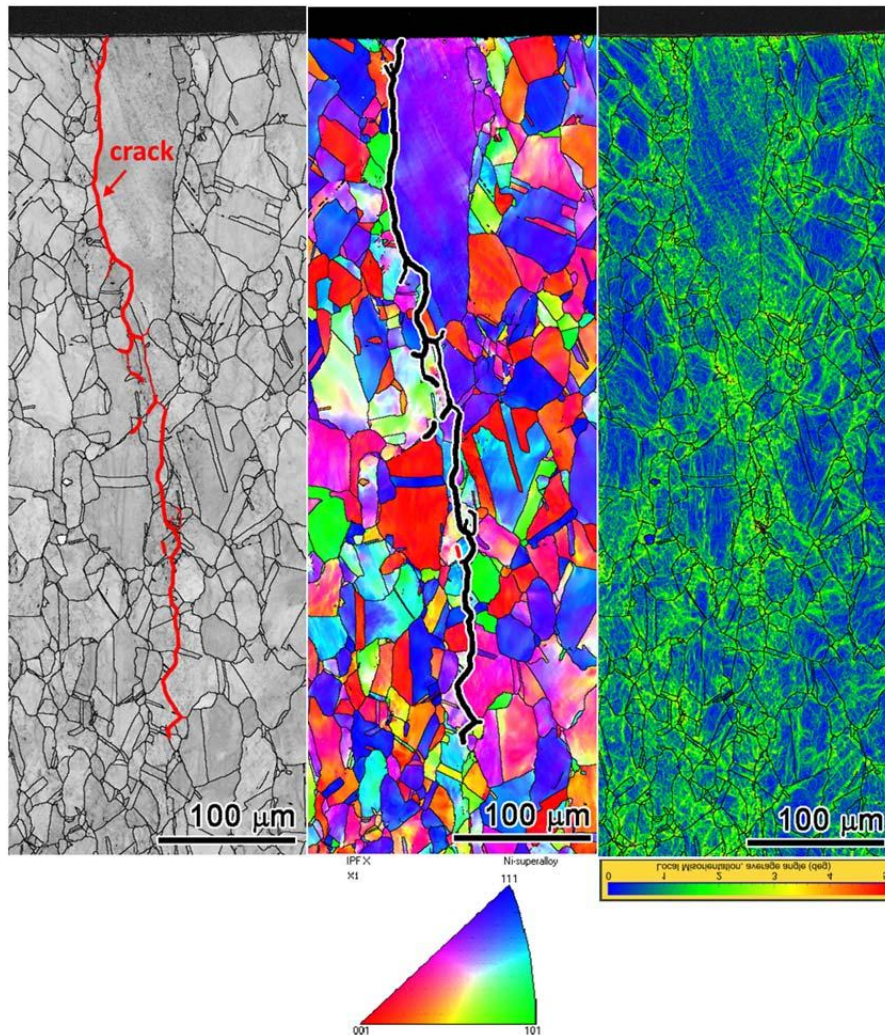
Figure 47. The pattern quality, inverse pole figure (IPF), and local misorientation maps in the cross-section of IN148 where the crack was found along the boundary between a large elongated grain and small grains (highlighted in the pattern quality and IPF figures).

addition, carbide variations and B segregation differences in this MA material may also play a role. Preliminary examinations did not reveal apparent differences in IG carbide density and composition at the grain boundaries of small grains and the boundary between large grains and small grains where crack nucleation took place (Figure 48). More investigations are needed to establish these grain boundary characteristics for the large elongated grains. Another possibility is that a properly oriented large grain results in a less tortuous grain boundary with a better alignment for mode I cracking [34]. This has been evidenced in the fracture surface in the 15%CF specimens where the large elongated grains exhibited a smoother surface in comparison to the smaller grains (Figures 44 and 45). It is also possible that the high applied stress at low homologous temperature produces a higher local strain rate at the boundary of large elongated grains and promotes SCC initiation. However, previous characterization results suggest that

SCC initiation seems to take place once the primary crack reaches a critical size of ~250 µm in surface length and ~100 µm in depth.  As shown in Figure 45, some of the 15%CF PNNL specimens with longer SCC initiation times also have large grains at the crack plane with a size well beyond the critical size for macroscopic SCC initiation, suggesting not all large grains can lead to rapid SCC initiation.  While this might be related to the orientation of the specific grains that can affect local shear stress and creep strains, more study is needed to elucidate the dominant factors of this phenomenon.
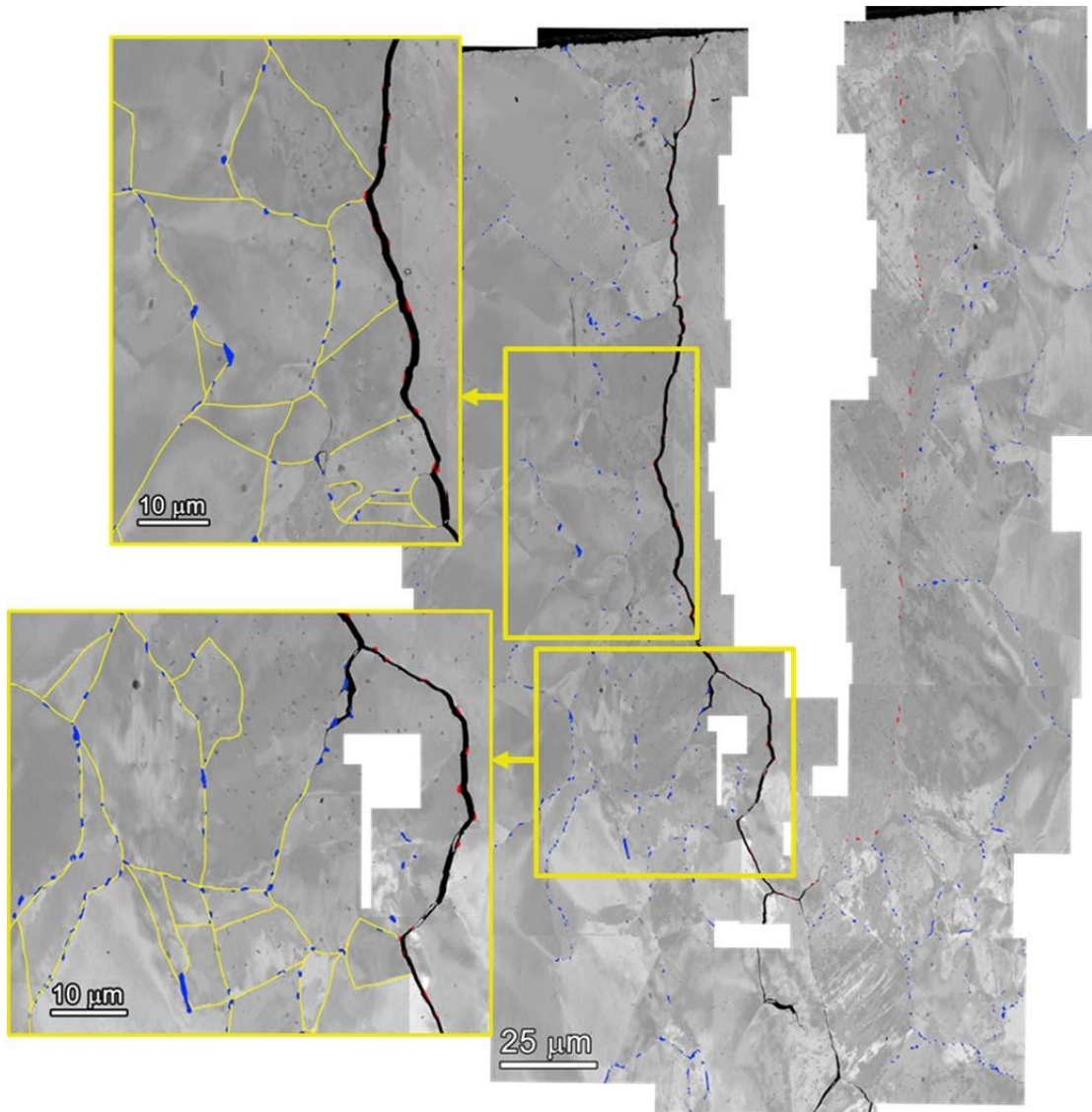


Figure 48.  IG carbide distribution in the vicinity of the primary crack on the cross-section of IN148.  The carbides on the boundary of large grain are highlighted in red and the carbides on the boundary of small grains are highlighted in blue.

SA+15%CF Alloy 600 Plate Heat 31907

The three 15%CF alloy 600 Foroni 31907 specimens IN151-153 were tested in a small LWRS system. As shown in the overall evolution of referenced DCPD strain in Figure 49, all three specimens exhibited surprisingly short and very consistent SCC initiation times ranging from 295-356 hours. IN151 showed the earliest initiation at 295 h, but with a slightly more gradual increasing slope in comparison to the other two specimens. Post-test examination at 352 h revealed a few large cracks with surface lengths ranging from ~150-350 μm. These cracks appear to be much less tortuous than those observed in the MA PNNL plate heat specimens. This is reasonable since the SA alloy plate heat 31907 has a much larger grain size, and it seems that the cracks generally occur along only 1 or 2 grains on the surface. In addition, the cracks also appear to be tighter as compared to those in the MA PNNL plate heat specimens. In order to have an idea on the depth of the cracks, this specimen was cross-sectioned along a plane intersecting a crack of medium size on the surface. As shown in Figure 50, this crack extended to a depth of ~580 μm, which is more than two times of its surface length. This confirmed that the specimen had fully initiated and it is expected that the cracks with longer length on the surface had grown even deeper inside the material.
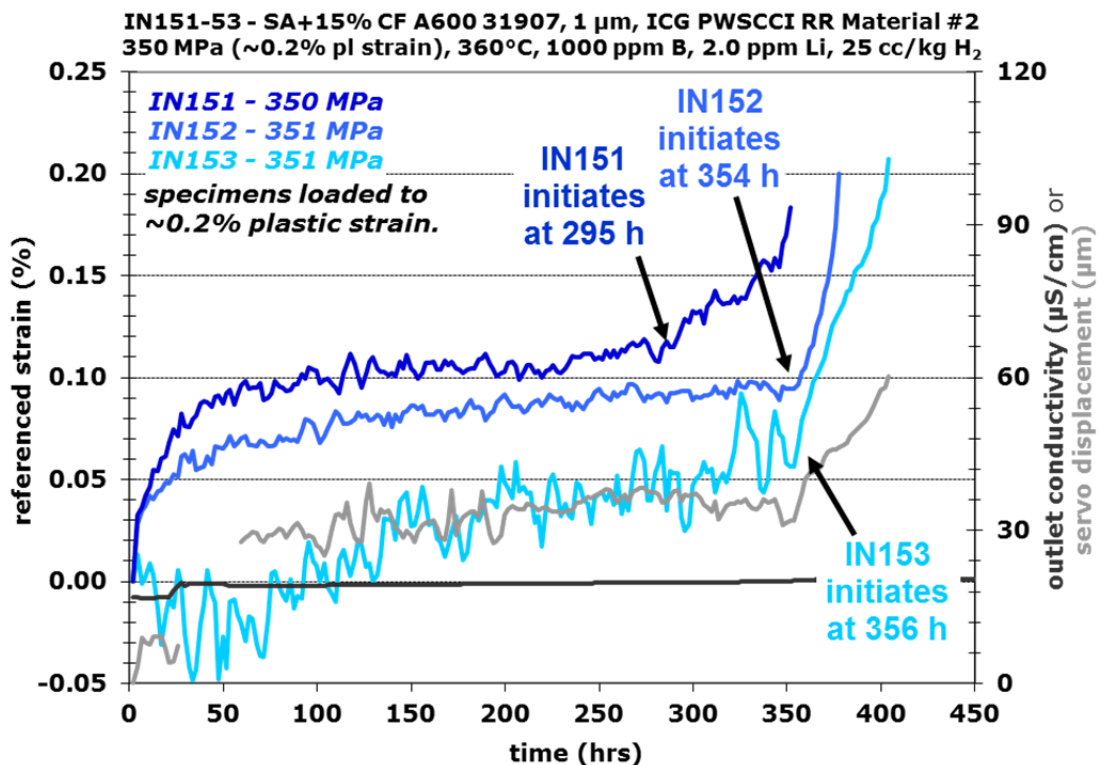


Figure 49. Referenced DCPD strain response showing early initiation for the 15%CF specimens IN151-153 from the SA Alloy 600 plate heat 31907 tested at their yield stress at 360$^{o}$C.
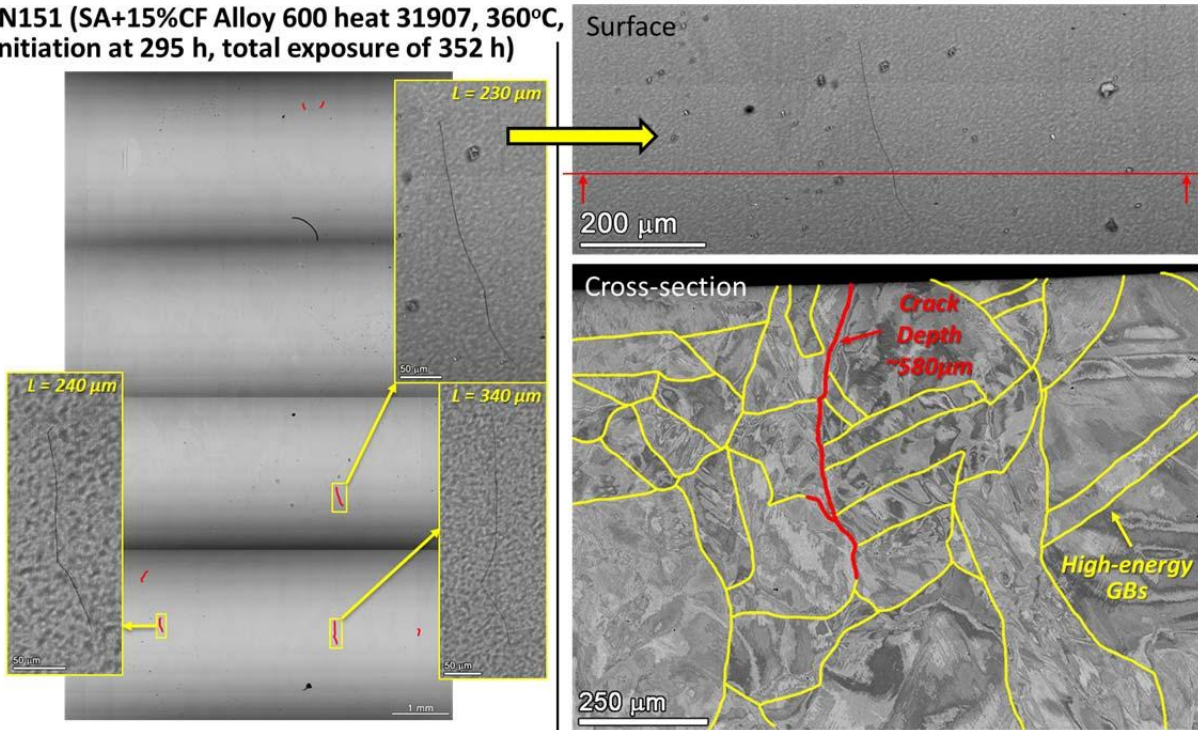
Figure 50. SEM-BSE montage image of the post-test gauge surface of SA alloy 600 plate heat 31907 specimen IN151 with obvious cracks are highlighted in red (left). The specimen was later cut into two halves and the cross-section morphology of a medium size crack is shown with the crack highlighted in red and surrounding high-energy grain boundaries in yellow (right).

IN152 and IN153 were also examined for indication of precursors and cracks when the test was interrupted at 350 h to remove the already initiated IN151. The two specimens were reloaded to yield stress and SCC initiation was detected soon afterwards at ~354 h for IN152 and ~356 hours for IN153. The reason that the test continued for a longer time after DCPD-detected SCC initiation is the appropriate reduced load was being evaluated where an initiated specimen was allowed to fail without affecting other specimens. As a result, IN152 failed during this trial and the test ended at 514 h. It should be noted that from 356 to 514 h, the two specimens were loaded at a stress significantly lower than the yield stress.

As shown in the left image in Figure 51, two obvious cracks of ~300 μm long on the surface were identified in IN152 at 352 h right before SCC initiation was detected by DCPD. This specimen failed at a reduced load before the test ended and the fractured surface morphology is presented on the right side of Figure 51. Large grains of up to ~500 μm in diameter can be seen on the fracture surface with sporadically distributed small grains of 100-200 μm in size. On the other hand, no obvious cracks were observed on the surface of IN153 when the test was interrupted at 352 h, but SCC initiation readily occurred at the restart of the test (Figure 50). Interestingly, post-test examination after 514 h of exposure only revealed three cracks with

similar or shorter surface length ($\leq$200 μm) as those detected on IN151 and IN152 when exposed for much shorter time (Figures 50 and 51).  However, one crack in IN153 showed significantly wider opening in comparison to all cracks observed in the three specimens, suggesting it had grown significantly deep below the surface.  The above findings suggest that instead of extending on the surface, the cracks in the SA+15%CF Foroni material tend to favor propagation in depth.  While this likely indicates high variability in SCC initiation susceptibility at different grain boundaries, more investigation is needed to elucidate whether this can be associated with the duplex grain size or any local change in segregation and stress/strain distribution that may affect the SCC initiation susceptibility of grain boundaries.
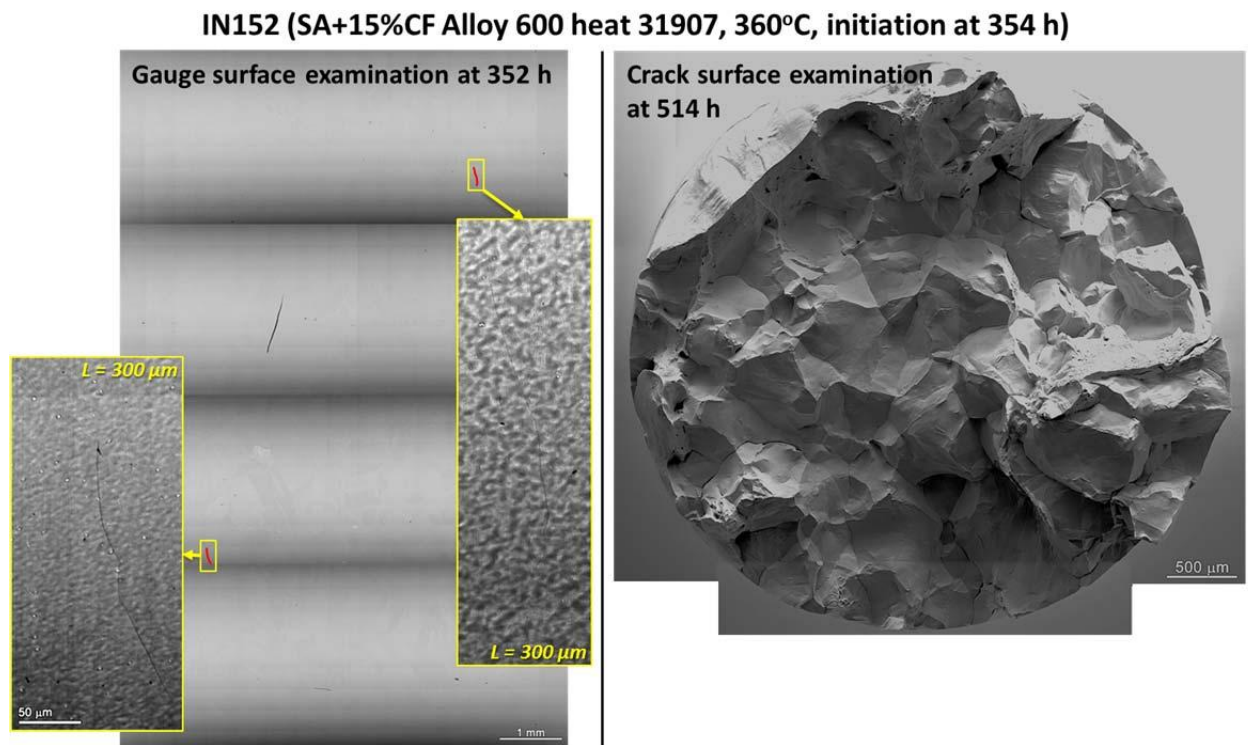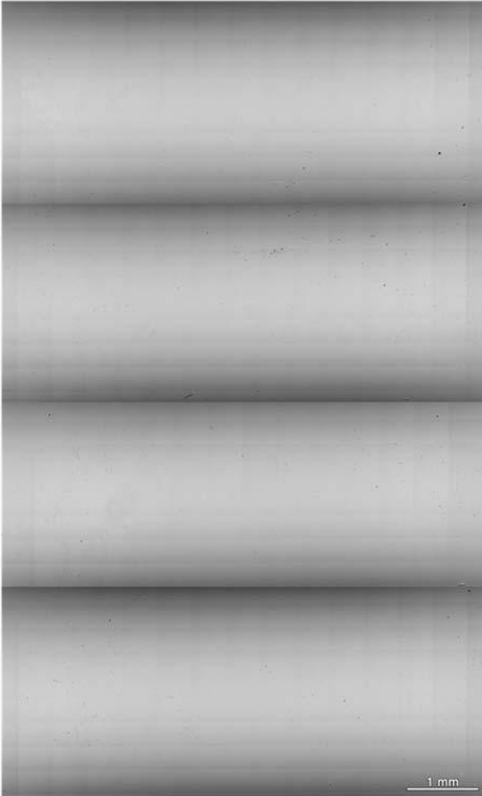


Figure 51.  SEM-BSE montage image of the gauge surface of SA alloy 600 plate heat 31907 specimen IN152 right before SCC initiation detected ~2 h later, revealing two large cracks (left). The specimen was failed in the test and the fracture surface was examined after conclusion of the test (right).

**IN153 (SA+15%CF Alloy 600 heat 31907, 360°C, initiation at 356 h)**

Surface morphology *at 352 h* right before DCPD-indicated initiation - **No obvious cracks**

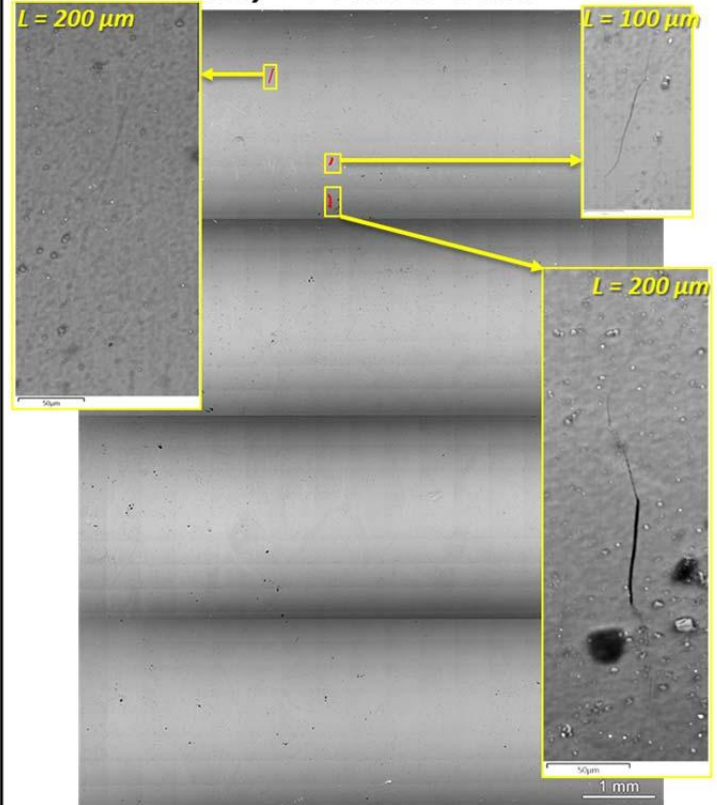Surface morphology *at 514 h* after DCPD-indicated initiation at 356 h - **Only 2-3 obvious cracks**

Figure 52.  SEM-BSE montage image of the gauge surface of SA alloy 600 plate heat 31907 specimen IN153 at test interruption at 352 h right before SCC initiation detected ~4 h later (left) and after the conclusion of the test at 514 h (right).

67

SA+15%CF Alloy 600 Plate Heat 11415

The final ICG-EAC round robin material (15%CF Rolls Royce alloy 600 SA plate heat 11415) was also tested in a small LWRS system and included specimens IN203, IN204 and IN205. The referenced DCPD strain response during the test is shown in Figure 60. SCC initiation was detected in IN203 at 1023 h followed closely by IN204 at 1054 h. The test continued until IN205 showed signs of SCC initiation at 1696 hours and ended at 1985 h. All three specimens exhibited well-behaved initiation behavior with obvious upturn in referenced strain rate typical of CW alloy 600 materials. Somewhat different from other experiments, the test on the Rolls Royce plate material continued until SCC initiation was detected by DCPD for all three specimens without interruptions.
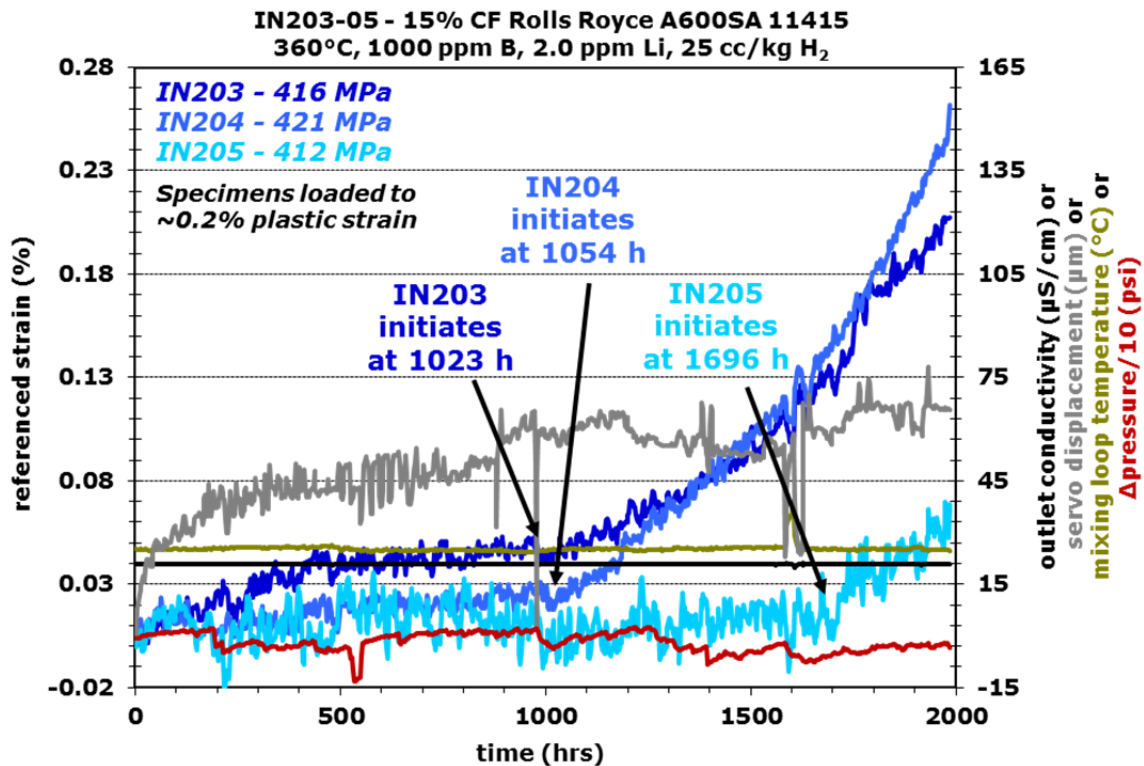


Figure 53. Referenced DCPD strain response for the 15%CF specimens IN203-205 from the SA Alloy 600 plate heat 11415 tested at their yield stress at 360°C.

Post-test SEM examinations were performed on the gauge surface of these three specimens with results summarized in Figures 58-60. Longer cracks with surface length reaching 1 mm were observed in IN203 and IN204, whereas the largest crack in IN205 was only ~350 μm. This can be explained by the longer exposure time after SCC initiation was detected for IN203/204 (~1000 h) than for IN205 (~300 h). As noted earlier, this Rolls Royce heat exhibited a bimodal grain size distribution with grain diameters from ~100 μm to ~500 μm. Further examinations are planned on these specimens to obtain crack depth information and correlate to the grain size distribution. The SA+15%CF Rolls Royce specimens also revealed a higher density of

sporadically distributed short cracks on the gauge surfaces in comparison to the SA+15%CF Foroni specimens. This may suggest that crack nucleation occurs, but short crack growth is much more difficult for the Rolls Royce material leading to the much longer SCC initiation times that were detected by DCPD.
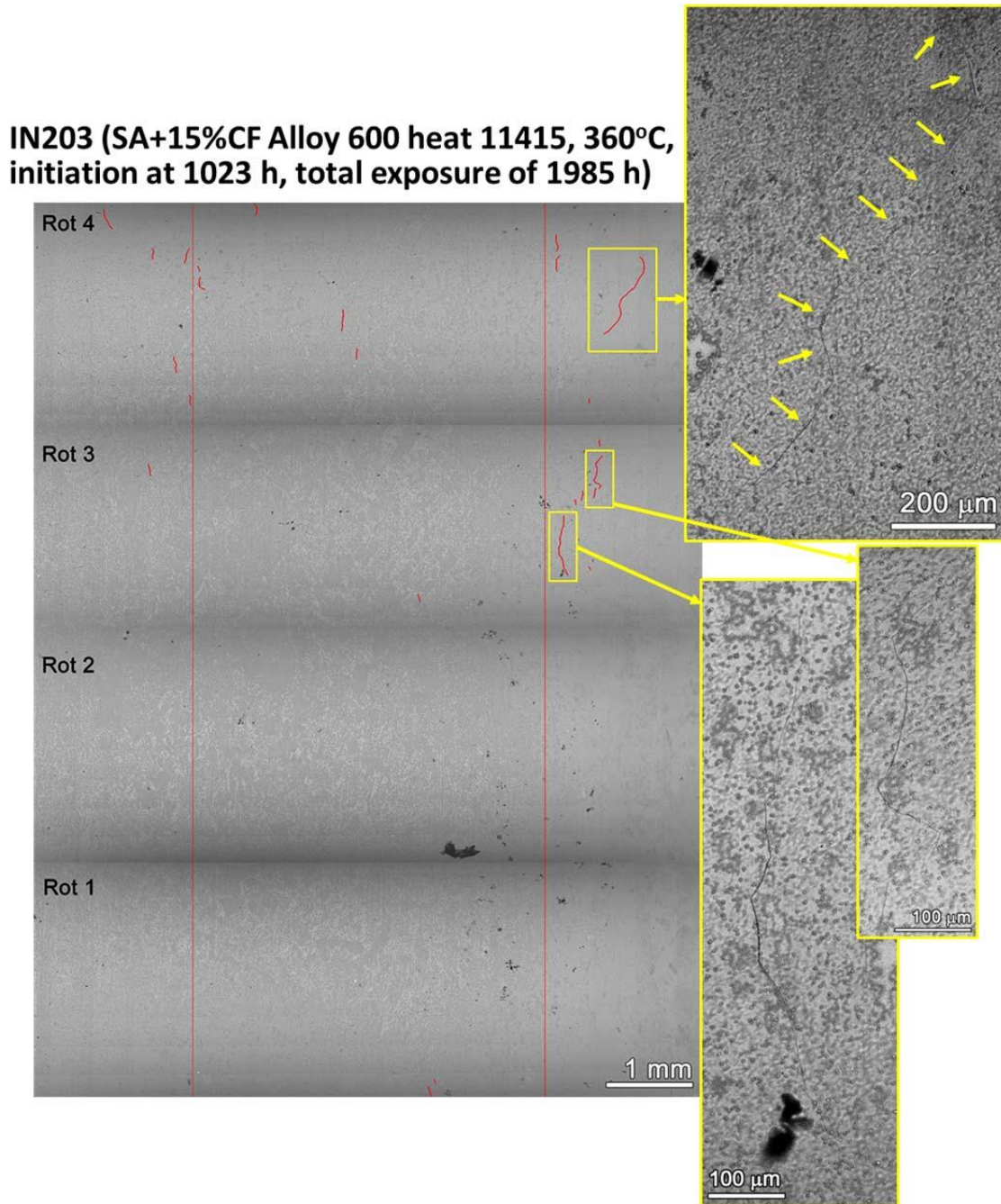


Figure 54. Post-test SEM-BSE montage image of the gauge (region within the two red lines) and part of the fillet (region outside the red lines on both sides) surface of SA+15%CF alloy 600 plate heat 11415 specimen IN203.
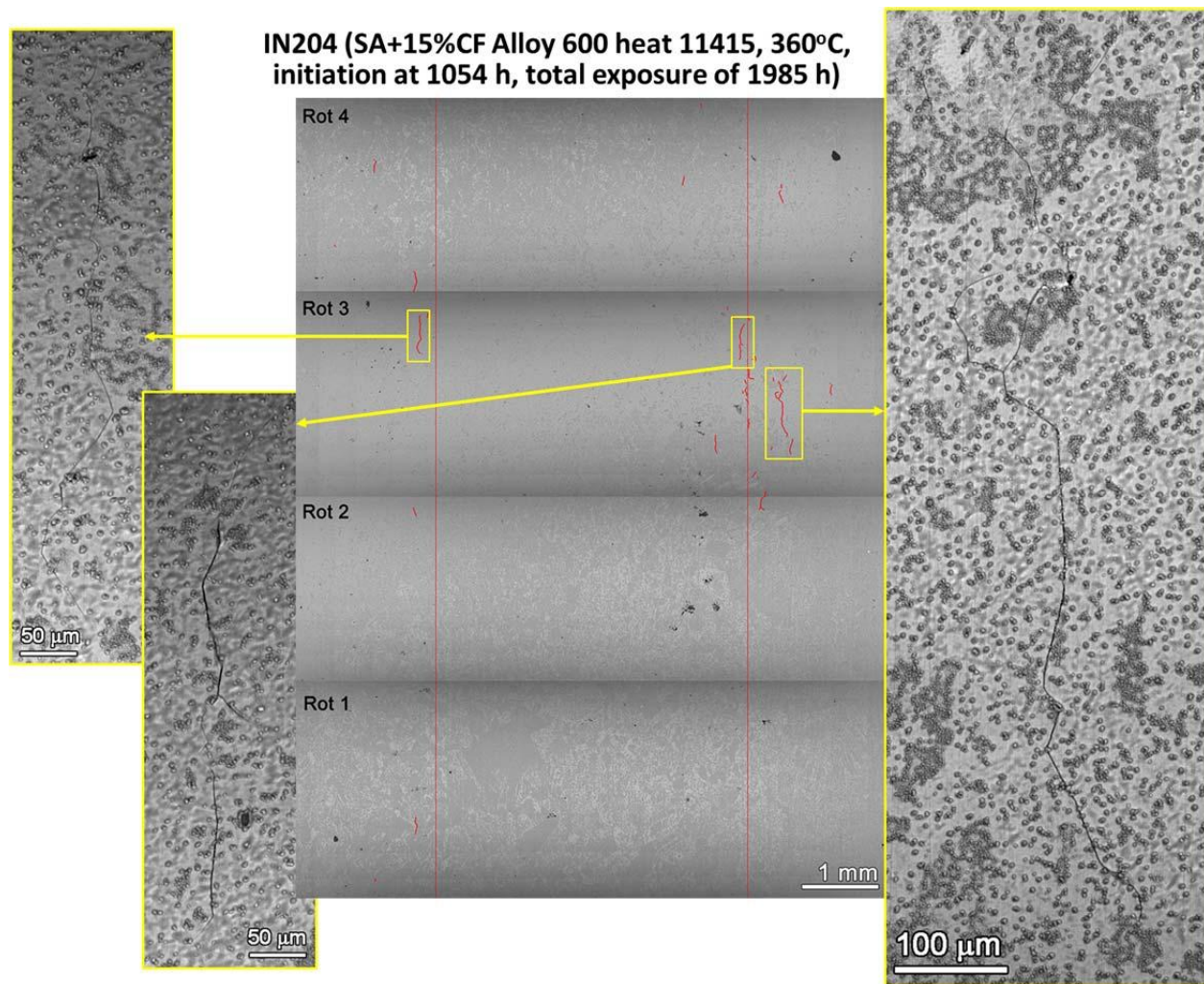
Figure 55.  Post-test SEM-BSE montage image the gauge (region within the two red lines) and part of the fillet (region outside the red lines on both sides) of SA+15%CF alloy 600 plate heat 11415 specimen IN204.
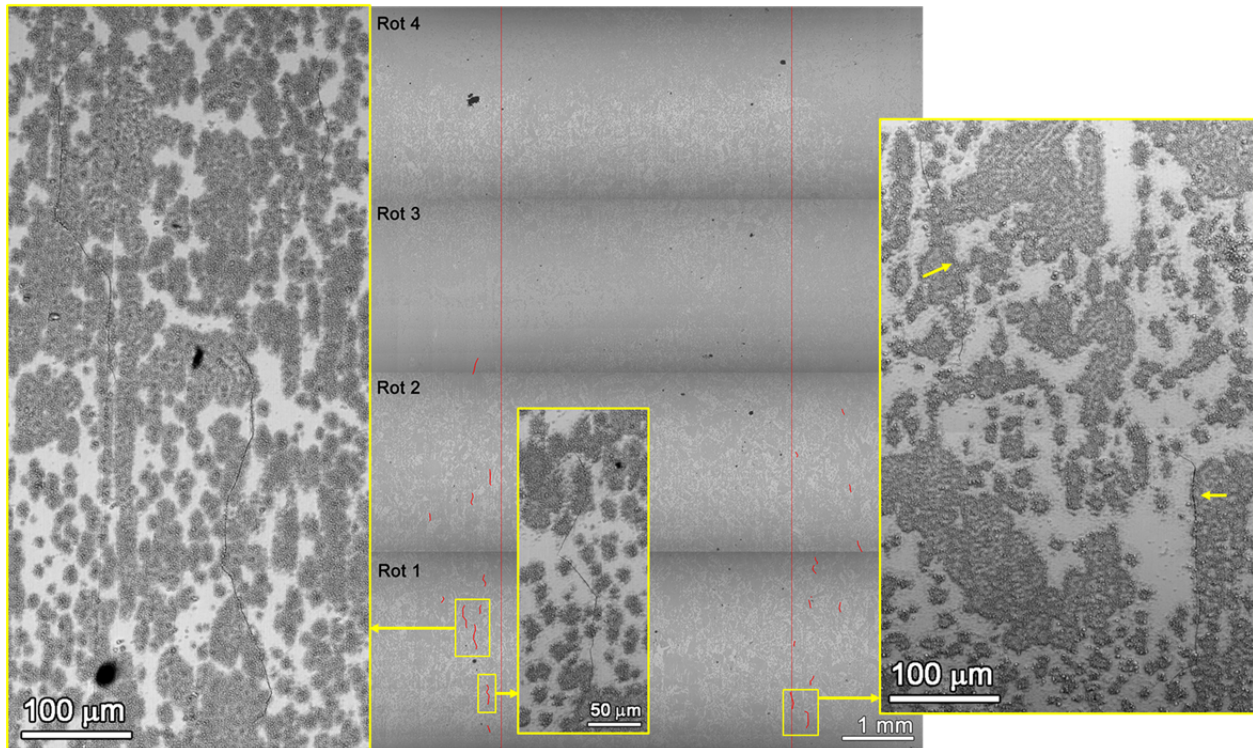
Figure 56.  Post-test SEM-BSE montage image of the gauge (region within the two red lines) and part of the fillet (region outside the red lines on both sides) of SA+15%CF alloy 600 plate heat 11415 specimen IN205.

*SCC Initiation Tests at 325°C PWR Primary Water*

Most of the SCC initiation testing in this program is performed in an accelerated manner at temperatures higher than those in normal PWR operation conditions. In order to better estimate SCC initiation behavior of materials used in service, the effect of test temperature on SCC initiation has been investigated using 15% CF alloy 600 materials. The heats NX6106XK-11 and 31907 were chosen for this study because of their high susceptibility to SCC initiation revealed in 360°C testing. It was anticipated that SCC initiation could be detected in a reasonable amount of time for these materials even when they are exposed to lower temperatures. The decision was made to perform the first lower temperature tests in simulated PWR primary water (1000 ppm B + 2 ppm Li) at 325°C that corresponds to the higher temperature range for operating PWR systems. A dissolved $H_2$ of 10.5 cc/kg was selected to again produce an electrochemical potential at the Ni/NiO stability line enabling a direct comparison to the 360°C tests and the determination of the activation energy for SCC initiation.

MA+15%CF Alloy 600 Plate Heat NX6106XK-11

Three 15%CF PNNL plate heat NX6106XK-11 specimens (IN206-208) and three 15%CF Foroni plate heat 31907 specimens IN209-211 were tested together in the same autoclave after the system had been upgraded to test up to 6 fully-instrumented specimens. The overall referenced DCPD strain evolution for the three PNNL plate specimens is summarized in Figure 57. SCC initiation was detected at 1465 h in IN206 followed by 1680 h in IN208 with an obvious upturn in referenced strain rate typical of CW materials as discussed in the previous section. However, IN207 exhibited a much longer initiation time of ~2580 h and the test was recently ended. It should also be noted that the time to SCC initiation in IN206 and IN208 is similar to the SCC initiation times obtained in most CW specimens from the same material at 360°C except the 15%CF IN146-148 exhibiting large elongated grains protruding deeply into the gauge. Therefore, it is suspected that the relatively early SCC initiation detected in IN206 and IN208 might be associated with large elongated grains and SEM examinations are being conducted to investigate this possibility.
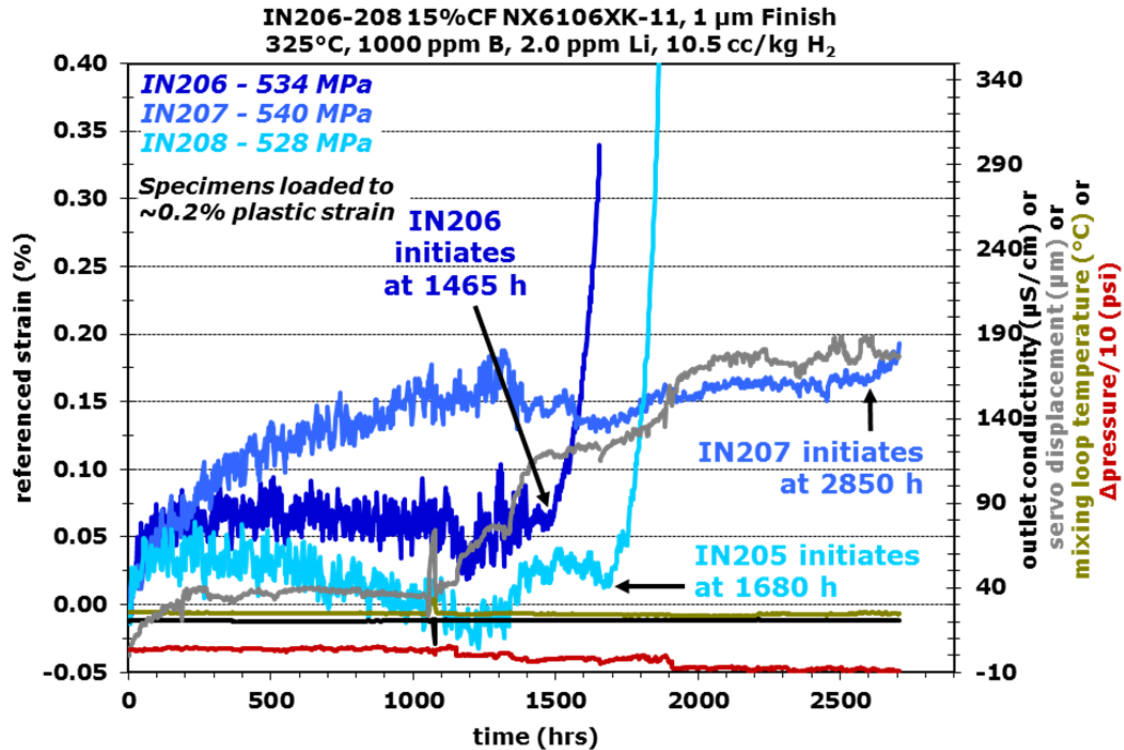
Figure 57. Referenced DCPD strain response for the 15%CF specimens IN206-208 from the MA Alloy 600 plate heat NX6106XK-11 tested at their yield stress at 325°C.

SEM surface examinations were performed on all three specimens at 1150 h and again on IN206 and IN208 after SCC initiation detected by DCPD. The evolution of gauge surface morphology is summarized for IN206 and IN208 in Figures 58 and 59, respectively. Neither IGA nor small cracks were observed in any specimen at 1150 h mainly due to a thick spinel-type oxide layer formed on the gauge surface obscuring a clear view of the surface microstructure. Similar to the typical SCC initiation morphology of CW specimens as discussed in the previous section, only three obvious cracks were observed in IN206 with the largest one exhibiting a surface length of ~600 μm. More significant cracking was observed in IN208 which is reasonable because test has been continued for longer time after SCC initiation was detected in this specimen. Nevertheless, three large cracks can be identified and possibly the longest one is the primary crack that led to SCC initiation detection. Unfortunately, due to the thick spinel oxide layer on the surface of these specimens, it was not possible to examine whether the primary cracks are associated with large elongated grains. Currently, methods to remove the surface spinel oxides are under evaluation in the hope that this can clear up the surface and enable a clearer view on IGA and grain boundaries. If no satisfying method could be found, the specimens will be cross-sectioned or opened in fatigue to cracking characteristics. Since the IN207 specimen recently initiated, information on the gauge surface cracking is not yet available.

73

Figure 58.  Post-test SEM-BSE montage image of the MA+15%CF alloy 600 plate heat NX6106XK-11 specimen IN206.

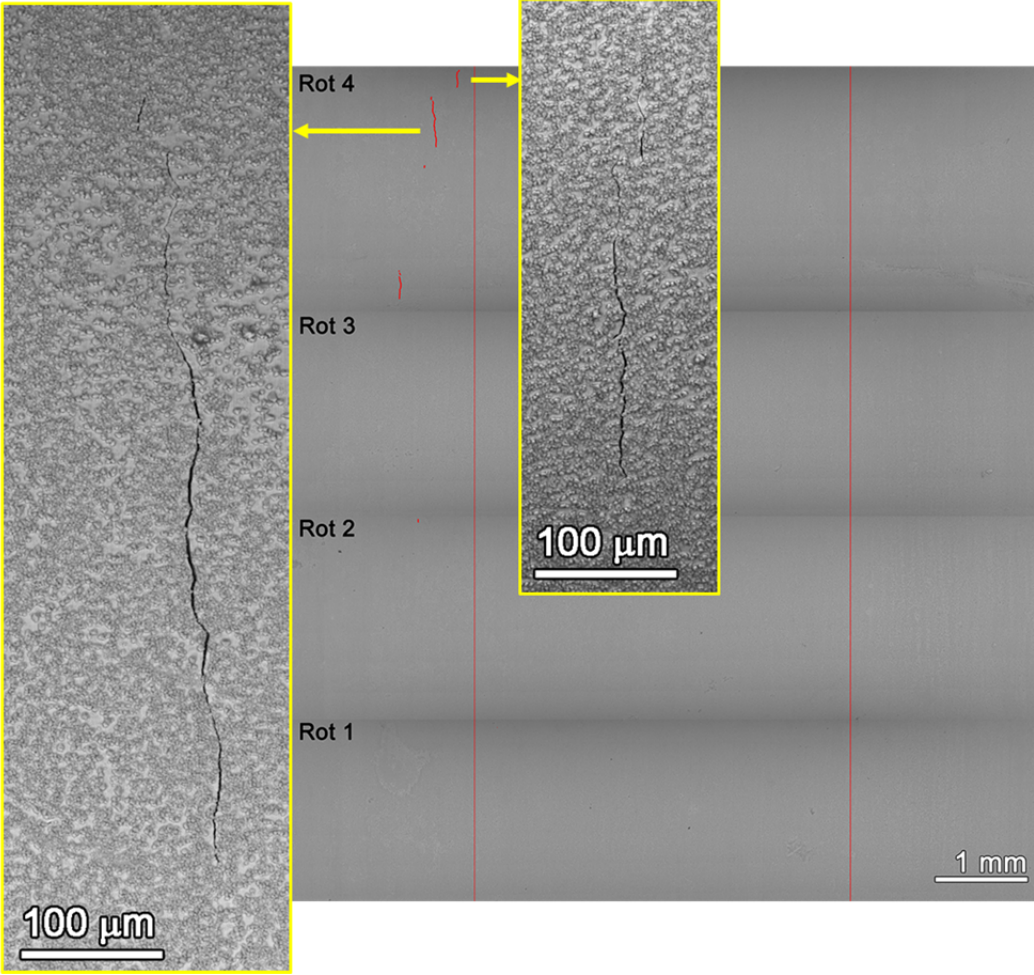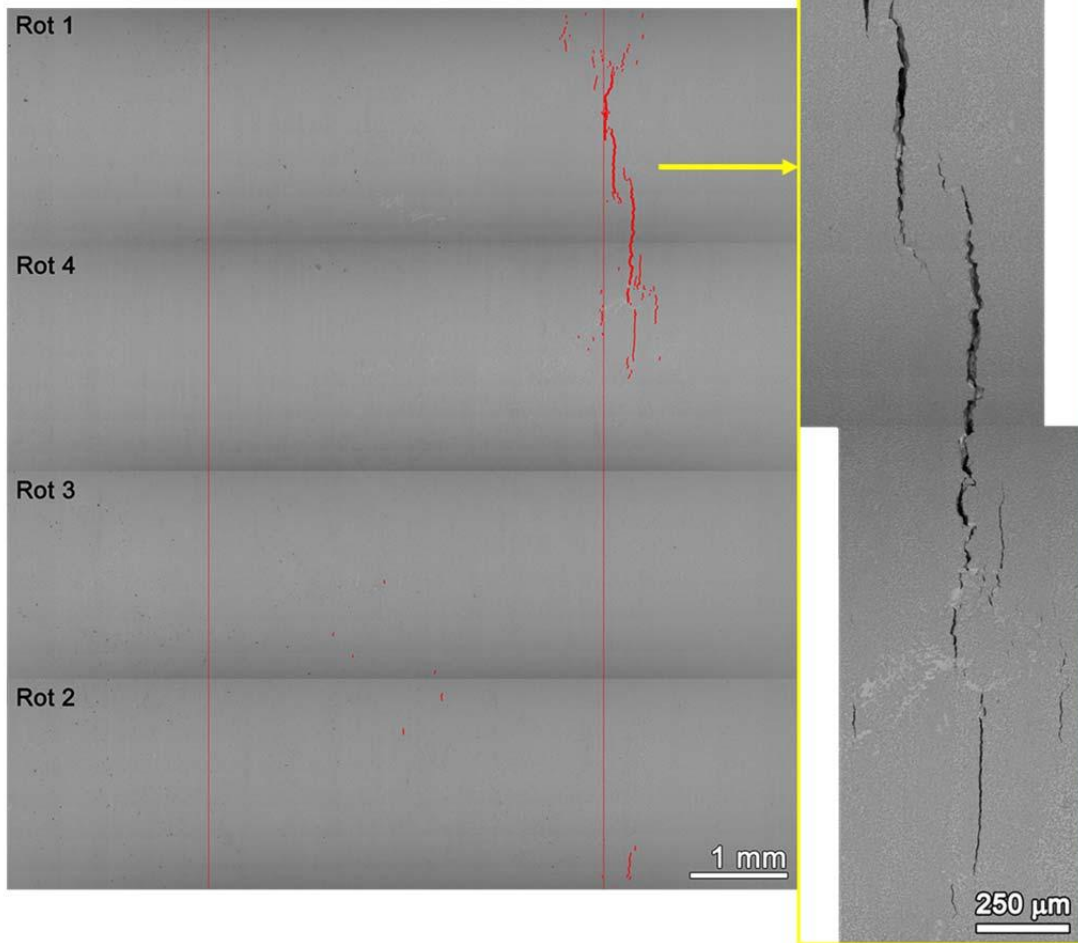Figure 59. Post-test SEM-BSE montage image of the MA+15%CF alloy 600 plate heat NX6106XK-11 specimen IN208.

SA+15%CF Alloy 600 Plate Heat 31907

The overall referenced DCPD strain evolution for the three SA+15%CF Foroni specimens IN209-211 is shown in Figure 60. Similar to the three specimens tested at 360°C, these three specimens also exhibited very consistent SCC initiation times ranging from ~1000-1350 h. SCC initiation first occurred in IN211 at 1040 hours and the test was interrupted at 1150 h to remove this specimen. As shown in Figure 61, only one large crack was found in this specimen. This crack extended to a surface length of ~800 μm and seems to have been created by coalescence of two smaller IG cracks as indicated in the image.
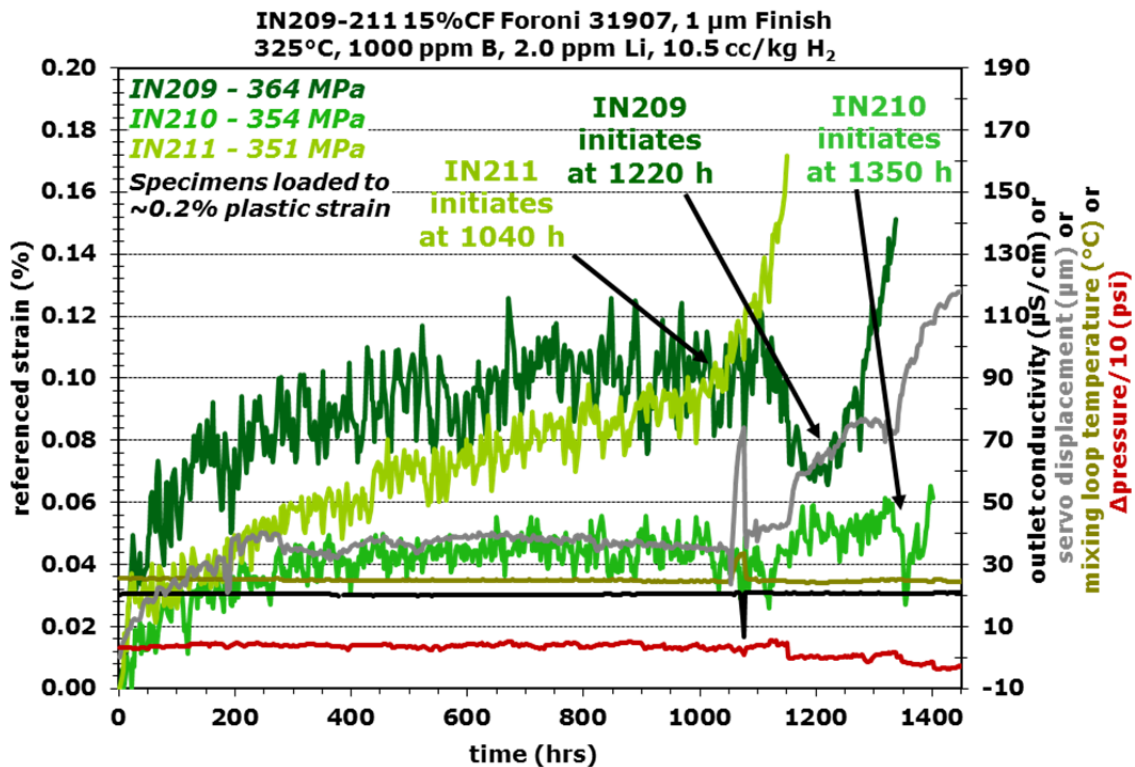


Figure 60. Referenced DCPD strain response for the 15%CF specimens IN206-208 from the MA Alloy 600 plate heat NX6106XK-11 tested at their yield stress at 325°C.
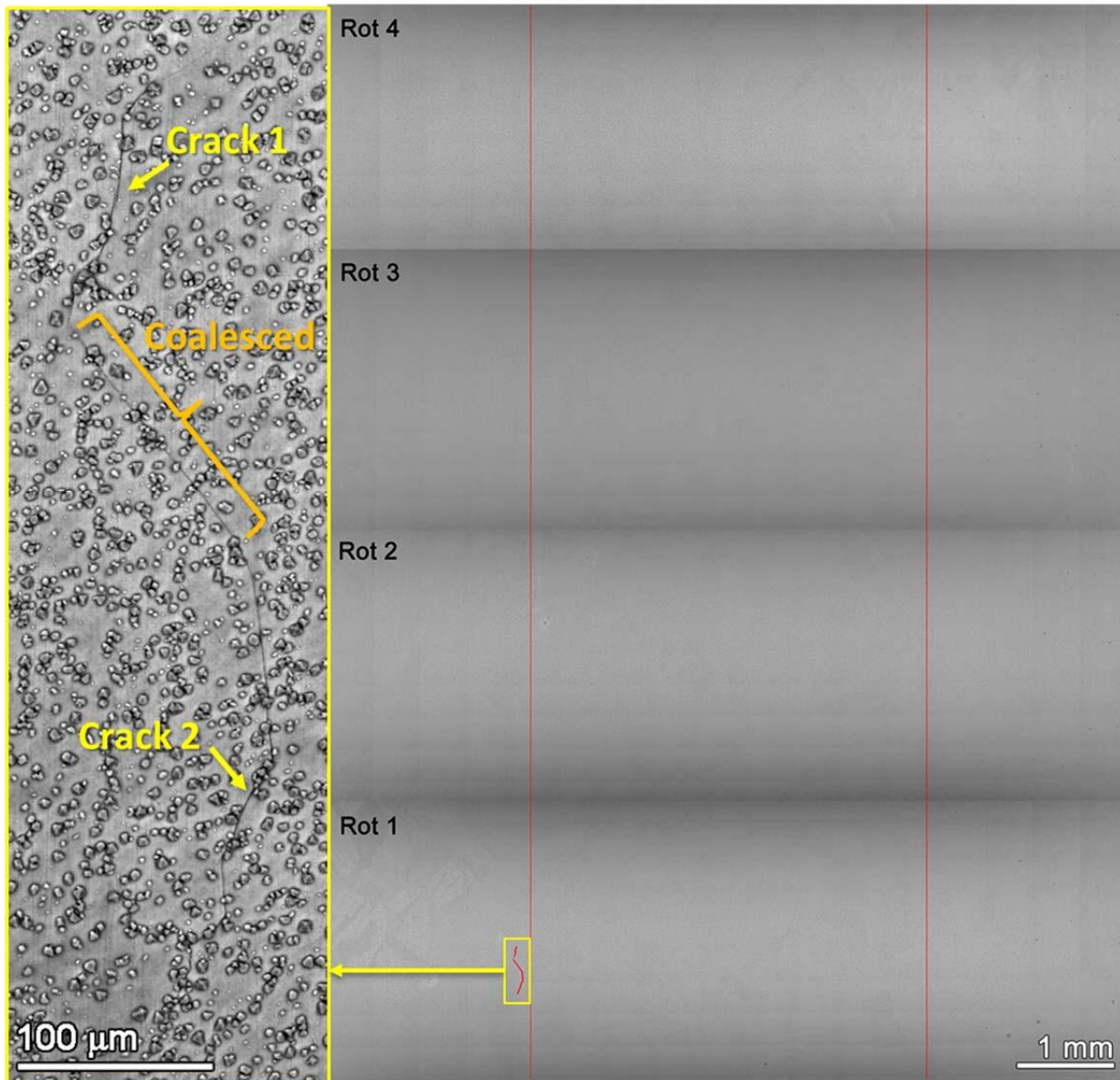
Figure 61. Post-test SEM-BSE montage image of the SA+15%CF alloy 600 plate heat 31907 specimen IN211.

SEM examinations were also performed on IN209 and IN210 after the test was interrupted at 1150 h and again shortly after SCC initiation was detected in each specimen, enabling evolution of surface morphology to be viewed over time. As shown in Figures 62 and 64, these two specimens didn't exhibit any obvious cracks at the test interruption after 1150 h of exposure, but both initiated within 100-200 h soon after the test was restarted. Closer examinations on surface morphology evolution were performed at selected sites in both specimens as shown in Figures 63 and 65. Relatively large cracks (surface length of 300-400 μm) were discovered after 1338-1400 hours, while no evidence for IGA or small cracks could be identified in these same locations during the 1150-h examinations. This indicates that the transition from IGA to short cracks then to macroscopic SCC initiation is very fast in this material. While high susceptibility of SCC initiation at certain large grains might played an important role, further investigation is needed to better elucidate the mechanisms controlling the transition to SCC initiation.
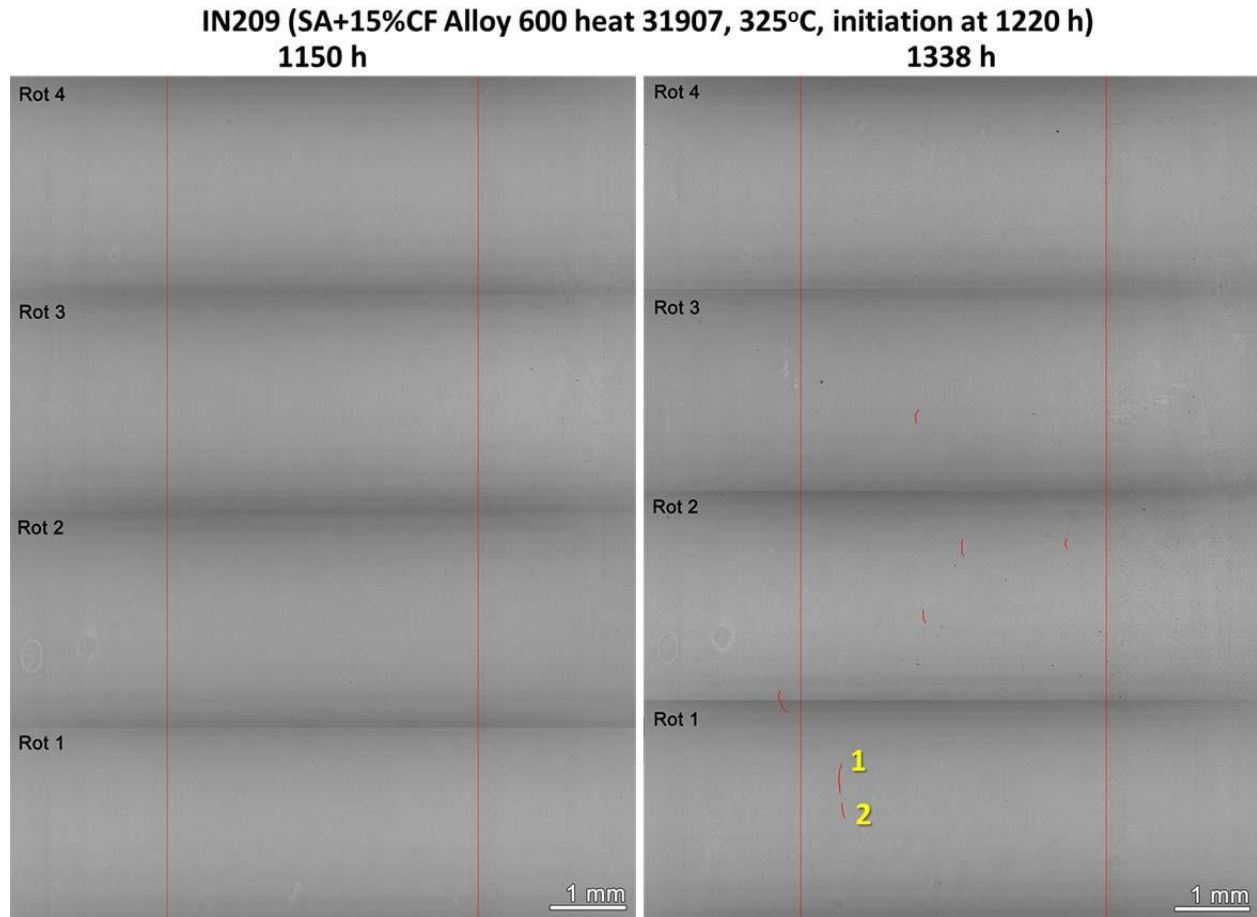


Figure 62. SEM-BSE montage image of the SA+15%CF alloy 600 plate heat 31907 specimen IN209 after test interruption at 1150 h (left) and after being removed from the system at 1338 hours after detection of SCC initiation (right).

Figure 63.  SEM-BSE montage image of surface morphology evolution at Sites 1 and 2 marked in Figure 62 in the SA+15%CF alloy 600 plate heat 31907 specimen IN209 at test interruption and after SCC initiation was detected by DCPD.

Figure 64.  SEM-BSE montage image of the SA+15%CF alloy 600 plate heat 31907 specimen IN210 after test interruption at 1150 h (left) and after being removed from the system at 1400 h upon detection of SCC initiation (right).
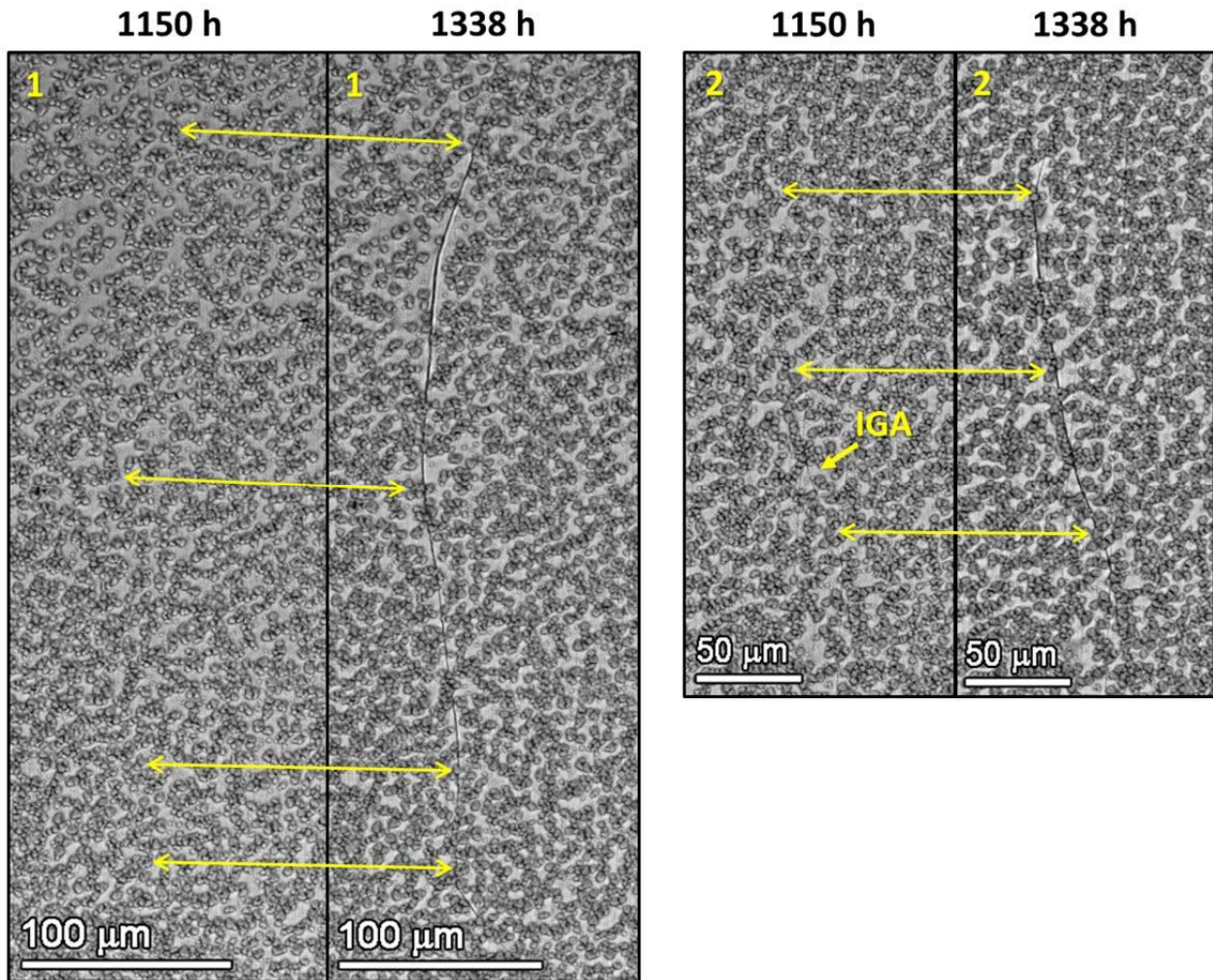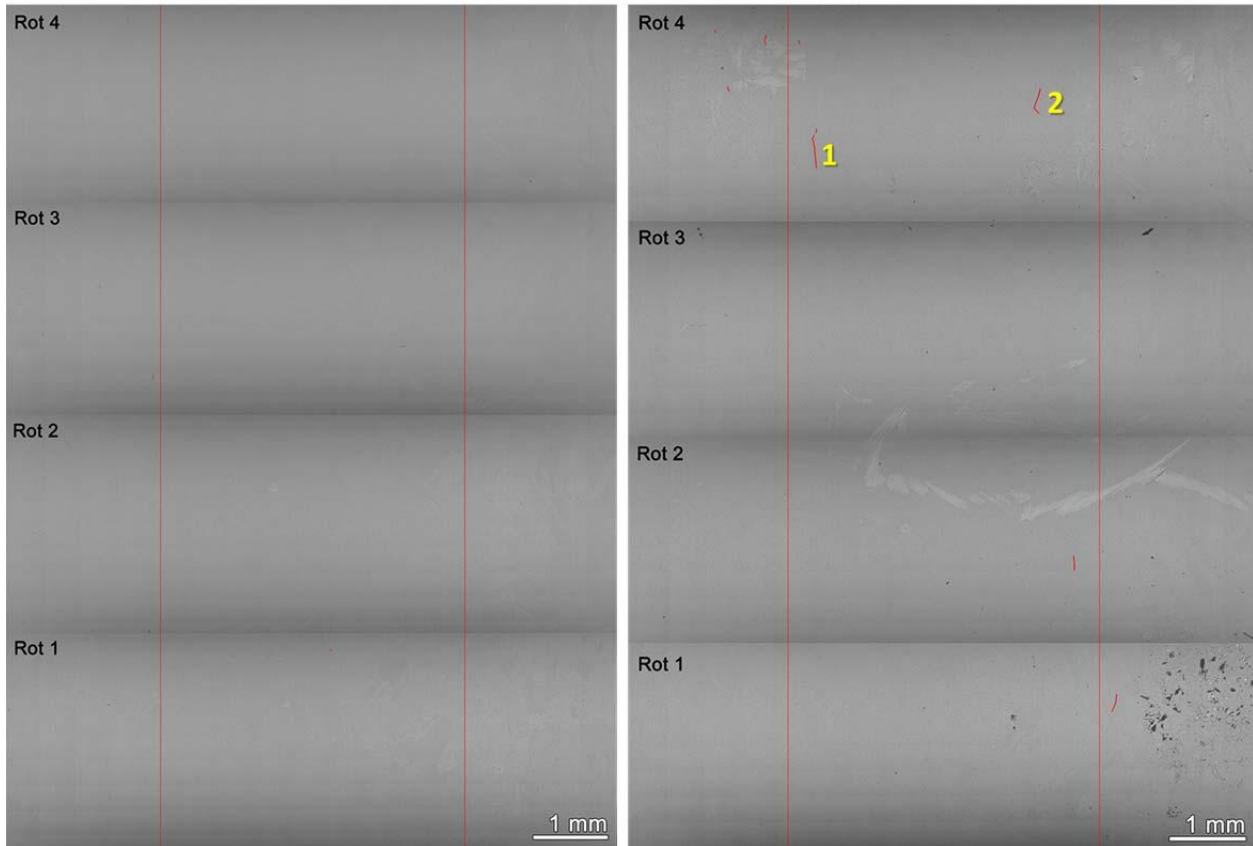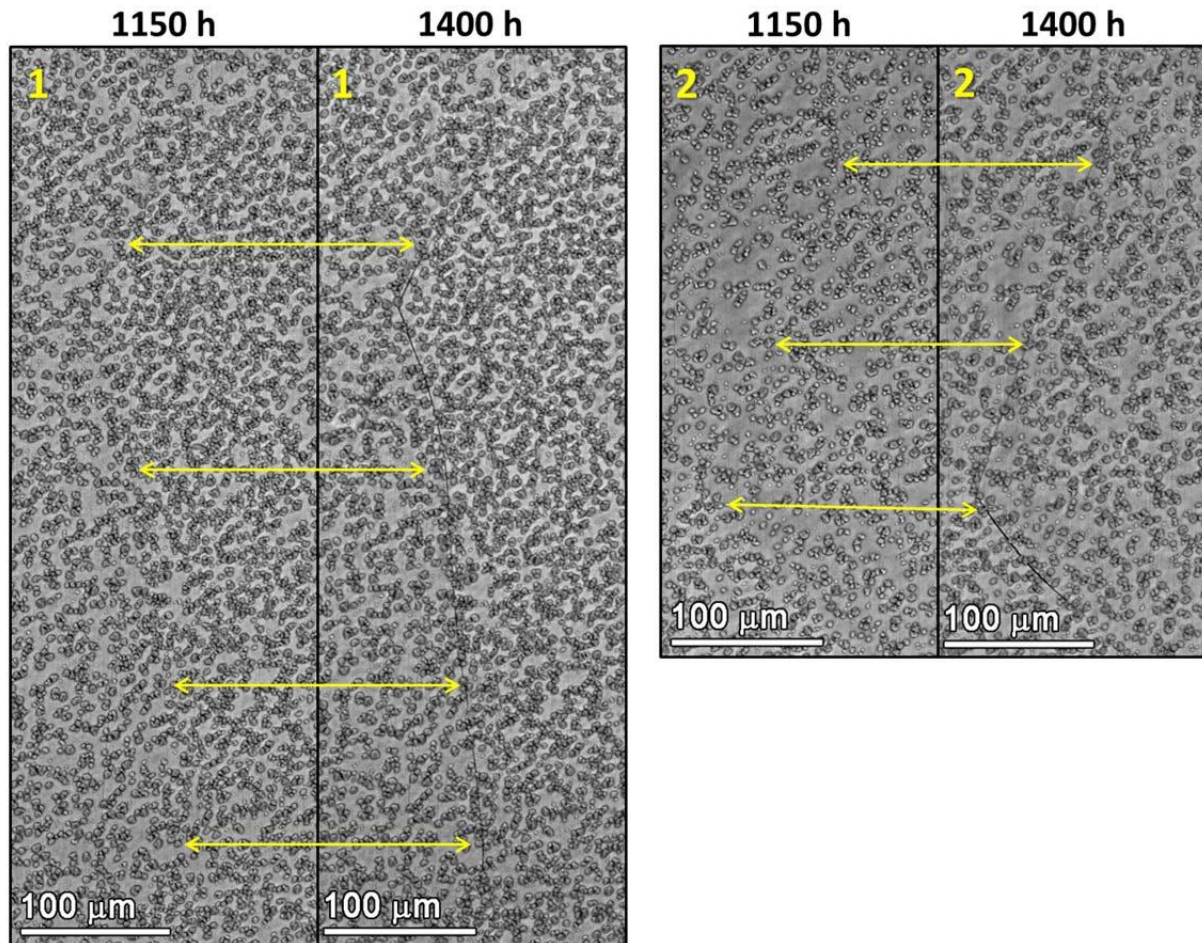
Figure 65.  SEM-BSE montage image of surface morphology evolution at Sites 1 and 2 marked in Figure 64 in the SA+15%CF alloy 600 plate heat 31907 specimen IN211 at test interruption and after SCC initiation was detected by DCPD.

The thermal activation energy for SCC initiation was estimated from data obtained on the SA+15%CF plate heat 31907 and the MA+15%CF plate heat NX6106XK-11 at 360$^{\circ}$C and 325$^{\circ}$C.  As shown in Figure 66, SCC initiation results revealed a thermal activation energy of ~116 kJ/mol for the SA heat and ~142 kJ/mol for the MA heat, which is in good agreement with prior data reported by KAPL [35].  It should be noted that for the MA+15%CF plate heat NX6106XK-11, only the specimens that showed early SCC initiation at both 360$^{\circ}$C (IN146-IN148) and 325$^{\circ}$C (IN206 and IN208) were considered for the determination of thermal activation energy.  This is based on the assumption that the early initiation of the two specimens IN206 and IN208 tested at 325$^{\circ}$C can also be associated with large elongated grains similar to IN146-148.  In addition, the specimens IN146-148 (360$^{\circ}$C) and IN206-208 (325$^{\circ}$C) were extracted from the same region of the PNNL plate and may have a similar microstructure. Detailed characterizations will be performed on the IN206-208 specimens to determine whether

the behavior of the 15%CF NX6106XK-11 specimens can be adequately explained.  At this point, the only valid assessment of activation energy should be based on the data for the 15%CF plate heat 31907 where consistent SCC initiation response was obtained at both temperatures. Depending on funding availability, SCC initiation data will be obtained at one additional temperature to enable a more accurate determination of the thermal activation energy.
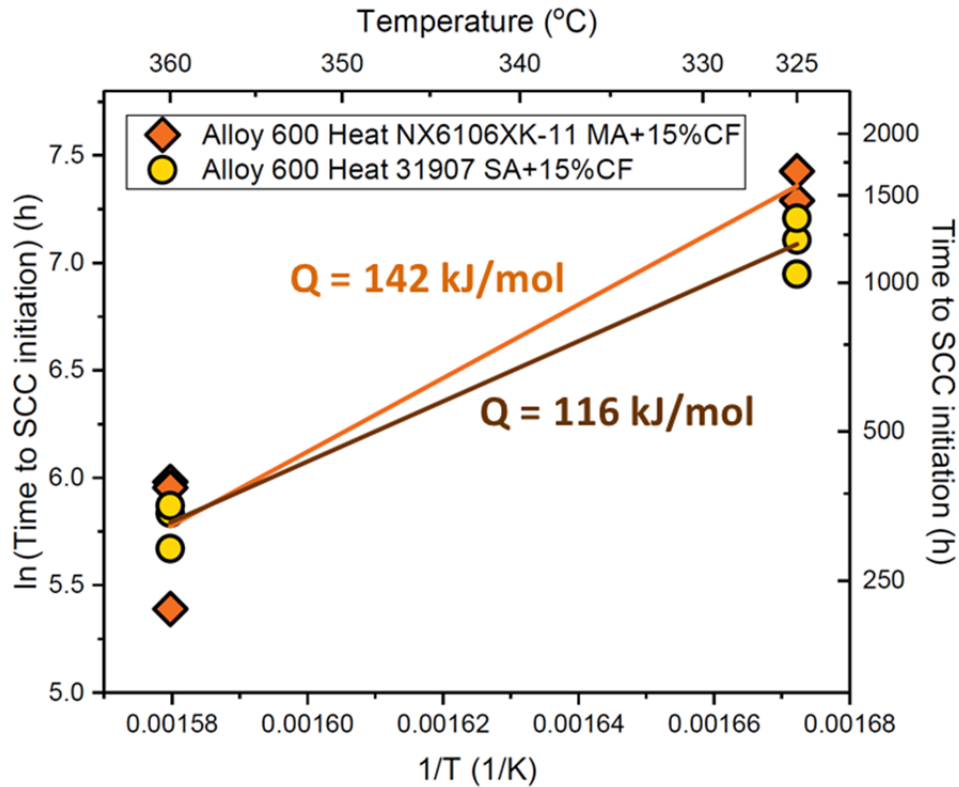


Figure 66.  Extrapolated thermal activation energy for the SA+15%CF plate heat 31907 and the MA+15%CF plate heat NX6106XK-11 tested at 360$^{o}$C and 325$^{o}$C with a dissolved H$_2$ concentration corresponding to the Ni/NiO stability line.

## Summary and Conclusions

Extensive SCC testing has now been completed on 7 different alloy 600 heats helping define the key aspects controlling precursor evolution and the transition to macroscopic SCC initiation. As shown in Figures 67 and 68, the plots of the time to SCC initiation as a function of applied stress and plastic strain have been updated with new results obtained from 27 new 15%CF specimens in addition to earlier data presented in Figures 36 and 37. In general, the time to SCC initiation measured by DCPD of these 15%CF specimens loaded at yield stress all fall below 3000 h, which is consistent with earlier data on specimens with either lower or higher cold work levels. This again demonstrated that a small amount of cold work can significantly reduce SCC initiation time, but additional cold work appears to have only a small effect.

Preliminary examinations of cracks suggest that the initiation time detected by DCPD represents a transition to rapid crack growth that occurs after the formation and coalescence of short cracks, which can be considered "practical" SCC initiation. As shown in Figures 32 and 33, the onset of SCC initiation in CW specimens appears to correspond to the primary crack reaching a surface length of ~250 μm and a depth of ~100 μm. This was further correlated to a $K$ level of ~10 MPa√m (Table 5) that is believed to trigger sustained crack growth at engineering relevant rates. While serial polishing and detailed examinations were not performed on crack shapes for the 21 new specimens, the cracking morphology on gauge surfaces is in agreement with the previous findings. The primary cracks found after SCC initiation in the SA+15%CF Foroni 31907 (Figures 50-52) and SA+15%CF Rolls Royce 11415 (Figure 56) normally have a surface length of 250-300 μm. As shown in Figure 50, these cracks tend to have a much greater depth than their surface length, confirming rapid crack propagation took place after SCC initiation. It should also be noted that based on surface morphology recorded at test interruptions and at the conclusion of the tests, the transition from shallow IGA to practical SCC initiation in the 15%CF specimens takes place within a very short time period relative to the total exposure time before crack initiation is detected by DCPD. This is evidenced in Figures 43, 52, 58-59, and 62-65 where IG cracks were not observed during examinations immediately before SCC initiation was detected by DCPD in multiple specimens from different heats and tested at different temperatures. While earlier results have shown a much more gradual and identifiable transition from shallow IGA to small cracks then to stable crack growth in the non-CW specimens, the new results suggest that this process was greatly shortened due to cold work.
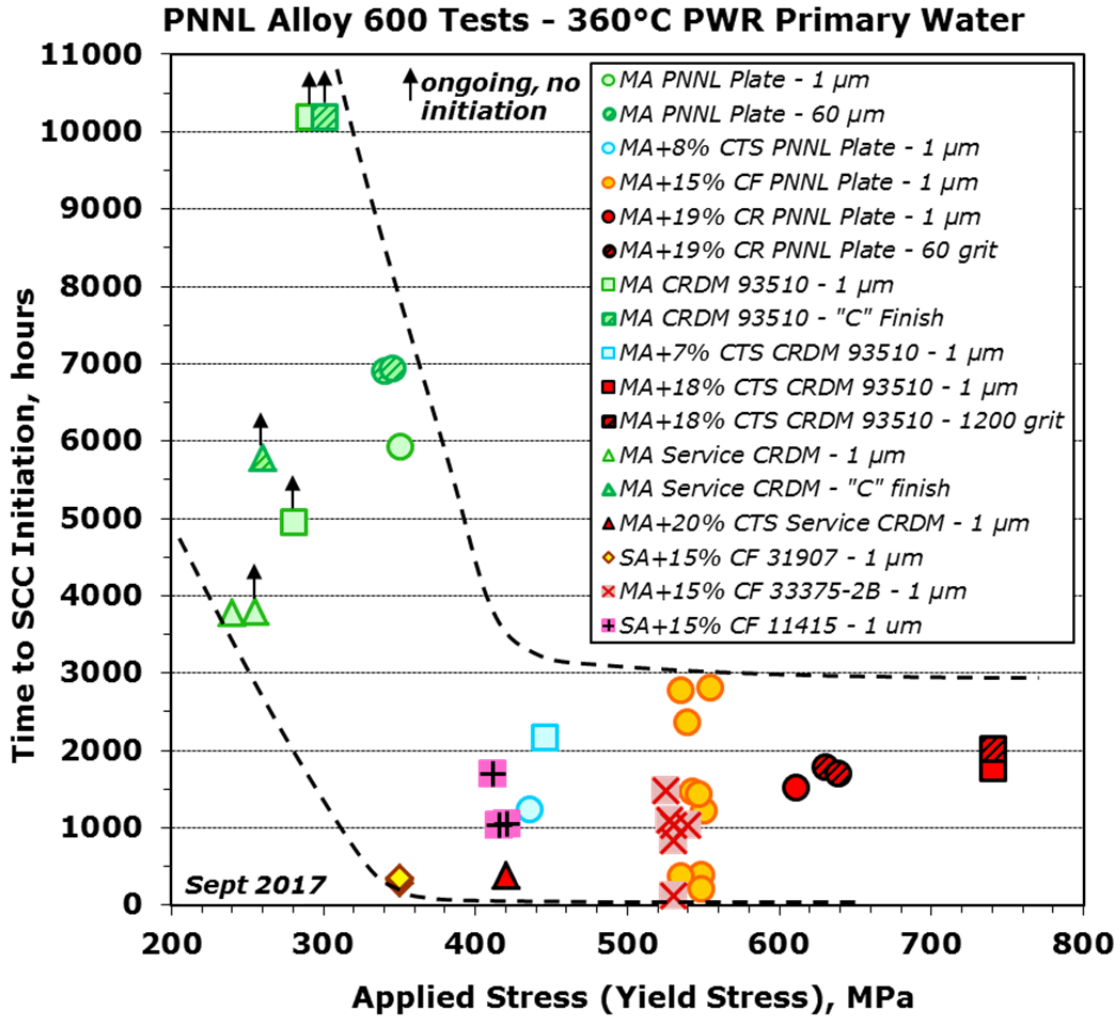
Figure 67. Update of measured SCC initiation time as a function of applied stress based on Figure 36. Dashed lines are meant to bound the data and aid in visualization of the initiation response. The data for six MA+15% CF 33375-2B specimens and six MA+15%CF PNNL plate specimens were obtained as part of a collaboration with a joint NRC/EPRI program.
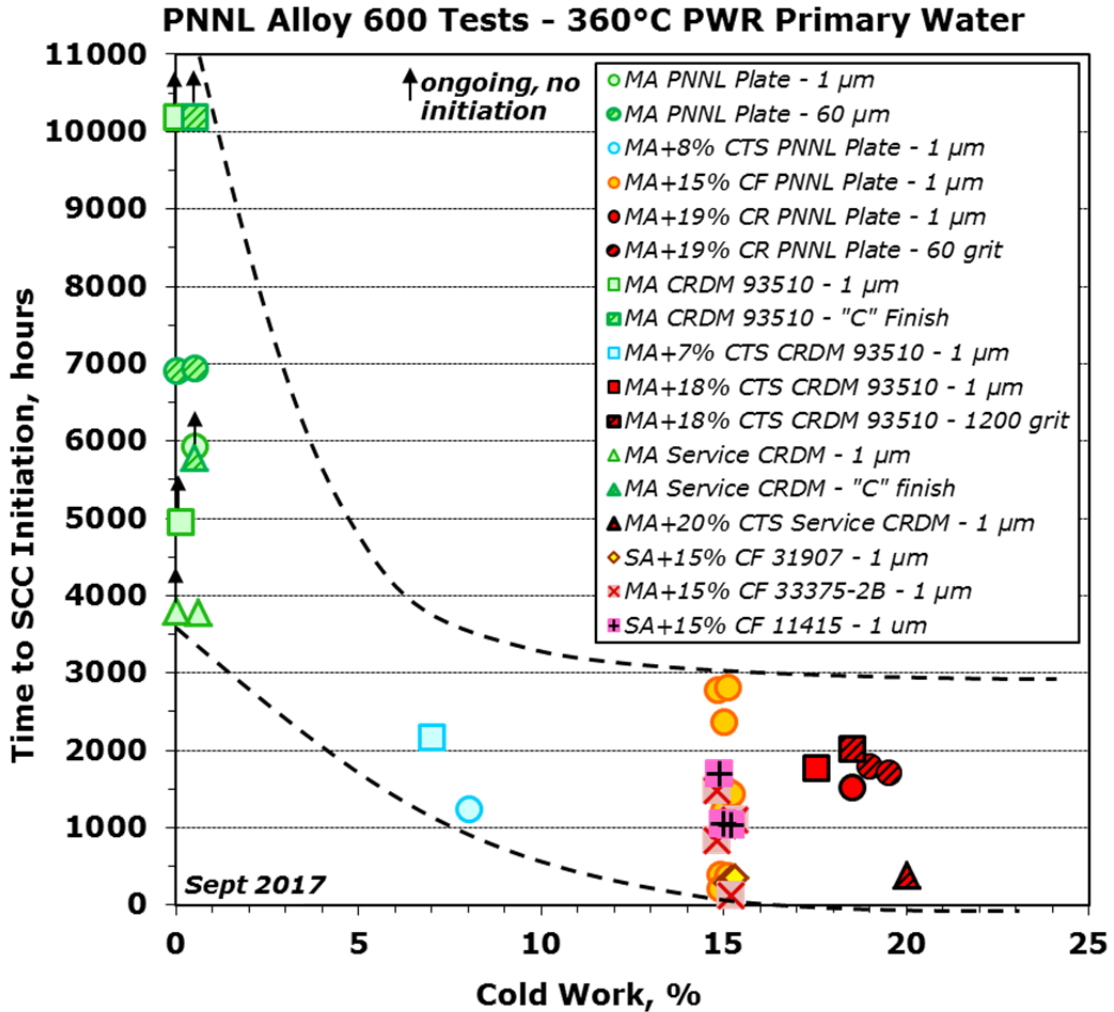
Figure 68. Update of measured SCC initiation time as a function of % cold work based on Figure 37. Dashed lines are meant to bound the data and aid in visualization of the initiation response. The data for six MA+15% CF 33375-2B specimens and six MA+15%CF PNNL plate specimens were obtained as part of a collaboration with a joint NRC/EPRI program.

While SCC initiation time were consistent with previous results for most of the new 15%CF alloy 600 specimens tested in 360°C simulated PWR primary water, unexpected short SCC initiation times were measured between 220 and 400 h for three 15%CF PNNL plate specimens (IN146-148). In comparison, ten other similar CW specimens all initiated after 1200 h of exposure (Figure 38). Detailed microstructural characterizations revealed that the inhomogeneous microstructure appears to promote differences in SCC initiation response. Early crack initiation was found to preferentially occur at sporadic large elongated grains in the banded plate especially when it protruded deep into the gauge. This is consistent with the findings in SCC crack growth tests on CW Ni-base alloys with inhomogeneous microstructures, where higher propagation rates have been reported when aligning the cold work and crack growth directions with the banded microstructure [31-33].

Although data is still limited, the tests performed on the SA+15%CF plate heat 31907 and the MA+15%CF plate heat NX6106XK-11 at 360 and 325°C have enabled the thermal activation energy for SCC initiation to be estimated at 116-142 kJ/mol for CW alloy 600 materials. This relationship will be useful for the extrapolation of accelerated test data generated at higher temperatures to reactor-relevant service conditions and improve predictions of behavior in PWR primary water systems.

In summary, considerable information has been collected on the effect of material heat and condition, degree of bulk cold work, surface condition, microstructural inhomogeneity and test temperature on SCC initiation of alloy 600. Nevertheless, more data is needed for a comprehensive understanding on the role of these influencing factors, and to clarify the rate controlling mechanism at the early stages encompassing IGA and short crack growth. Targeted investigations are continuing to better understand this process and establish the framework for quantitative modeling of SCC initiation for alloy 600 in PWR primary water environments.

**Acknowledgments**

## References

[1] M. B. Toloczko, M. J. Olszta, D. K. Schreiber and S. M. Bruemmer, *Stress Corrosion Crack Initiation of Alloy 600 in PWR Primary Water Environments*. Technical Milestone Report M3LW-13OR0403032, Light Water Reactor Sustainability Program, DOE Office of Nuclear Energy, March 2013.

[2] M. B. Toloczko, M. J. Olszta, D. K. Schreiber and S. M. Bruemmer, *Corrosion and Stress Corrosion Crack Initiation of Cold-Worked Alloy 690 in PWR Primary Water Environments*. Technical Milestone Report M2LW-13OR0402035, Light Water Reactor Sustainability Program, DOE Office of Nuclear Energy, September 2013.

[3] S. M. Bruemmer, M. J. Olszta, D. K. Schreiber and M. B. Toloczko, *Corrosion and Stress Corrosion Crack Initiation of Cold Worked Alloy 600 and Alloy 690 in PWR Primary Water Environments*. Technical Milestone Report M2LW-13OR0402035, Light Water Reactor Sustainability Program, DOE Office of Nuclear Energy, September 2014.

[4] Z. Zhai, M. J. Olszta, M. B. Toloczko and S. M. Bruemmer, *Summary of Stress Corrosion Crack Initiation Measurements and Analyses on Alloy 600 and Alloy 690*. Pacific Northwest National Laboratory: Technical Milestone Report M2LW-15OR0402034, Light Water Reactor Sustainability Program, DOE Office of Nuclear Energy, September 2015.

[5] Z. Zhai, M. B. Toloczko, K. Kruska, D. K. Schreiber, M. J. Olszta, N. R. Overman and S. Bruemmer, *Precursor damage evolution and stress corrosion crack initiation of cold-worked alloy 690 in PWR primary water*. Pacific Northwest National Laboratory: Technical Milestone Report M2LW-16OR0402034, Light Water Reactor Sustainability Program, DOE Office of Nuclear Energy, September 2016.

[6] R. A. Etien, E. Richey, D. S. Morton and J. Eager, "SCC initiation testing of alloy 600 in high temperature water", in *15th International Conference on Environmental Degradation of Materials in Nuclear Power Systems - Water Reactors*, 2011, Colorado Springs, CO, USA: The Minerals, Metals & Materials Society.

[7] M. J. Olszta, D. K. Schreiber, M. B. Toloczko and S. M. Bruemmer, *Microstructure, Corrosion and Stress Corrosion Crack Initiation of Alloy 600 in PWR Primary Water Environments*. Technical Milestone Report M3LW-13OR0403032, Light Water Reactor Sustainability Program, DOE Office of Nuclear Energy, March 2013.

[8] S. M. Bruemmer and M. B. Toloczko, *Pacific Northwest National Laboratory Investigation of Stress Corrosion Cracking in Nickel-Base Alloys*. NUREG/CR-7103, Volume 1, Nuclear Regulatory Commission, Office of Nuclear Regulatory Research, May 2011.

[9] S. M. Bruemmer and M. B. Toloczko, *Pacific Northwest National Laboratory Investigation of Stress Corrosion Cracking in Nickel-Base Alloys*. NUREG/CR-7103 Vol. 2, Nuclear Regulatory Commission, Office of Nuclear Regulatory Research, November 2011.

[10] Z. Zhai, M. J. Olszta, M. B. Toloczko and S. M. Bruemmer, "Precursor corrosion damage and stress corrosion crack initiation in alloy 600 during exposure to PWR primary water", in

*17th International Conference on Environmental Degradation of Materials in Nuclear Power Systems - Water Reactors,* 2015, Ottawa, ON, Canada: Canadian Nuclear Society.

[11] M. B. Toloczko, M. J. Olszta, Z. Zhai and S. M. Bruemmer, "Stress corrosion crack initiation measurements of alloy 600 in PWR primary water", in *17th International Conference on Environmental Degradation of Materials in Nuclear Power Systems - Water Reactors,* 2015, Ottawa, ON, Canada: Canadian Nuclear Society.

[12] Z. Zhai, M. B. Toloczko, M. J. Olszta and S. M. Bruemmer, "Stress corrosion crack initiation of alloy 600 in PWR primary water", *Corrosion Science*, Vol.

[13] D. S. Dunn, J. Collins, D. Alley, B. Alexandreanu, M. B. Toloczko and S. M. Bruemmer, "Primary Water Stress Corrosion Cracking Tests and Metallurgical Analysis of Davis Besse Control Rod Drive Mechanism Nozzle #4", in *16th International Conference on Environmental Degradation of Materials in Nuclear Power Systems - Water Reactors,* 2014, Asheville, NC, USA: NACE International.

[14] P. Scott, P. Combrade, R. Kilian, A. Roth, P. Andresen and Y. Kim, *Status Review of Initiation of Environmentally Assisted Cracking and Short Crack Growth*. EPRI, Palo Alto, CA: 1011788, 2005.

[15] R. L. Klueh, "Discontinuous creep in short-range order alloys", *Materials Science and Engineering*, Vol.54, Iss.1, 1982, pp. 65-80.

[16] M. A. Astiz, "An incompatible singular elastic element for two- and three-dimensional crack problems", *International Journal of Fracture*, Vol.31, Iss.2, 1986, pp. 105-124.

[17] A. Carpinteri, "Elliptical-arc surface cracks in round bars", *Fatigue & Fracture of Engineering Materials & Structures*, Vol.15, Iss.11, 1992, pp. 1141-1153.

[18] C. S. Shin and C. Q. Cai, "Experimental and finite element analyses on stress intensity factors of an elliptical surface crack in a circular shaft under tension and bending", *International Journal of Fracture*, Vol.129, Iss.3, 2004, pp. 239-264.

[19] P. M. Scott, "An analysis of primary water stress corrosion cracking in PWR steam generators", in *NEA/CSNI-UNIPEDE Specialist Meeting on Operating Experience with Steam Generators,* September 16-20, 1991, Brussels, Belgium.

[20] J. M. Boursier, D. Desjardins and F. Vaillant, "The influence of the strain-rate on the stress corrosion cracking of alloy 600 in high temperature primary water", *Corrosion Science*, Vol.37, Iss.3, 1995, pp. 493-508.

[21] S. Le Hong, C. Amzallag and A. Gelpi, "Modelling of stress corrosion cracking initiation of Alloy 600 in primary water of PWRs", in *9th International Symposium on Environmental Degradation of Materials in Nuclear Power Systems - Water Reactors,* August 1–5, 1999, Newport Beach, California.

[22] T. Cassagne and A. Gelpi, "Crack growth rate measurements on Alloy 600 steam generator tubing in primary and hydrogenated AVT water", in *6th international symposium on environmental degradation of materials in nuclear power systems - water reactors,* 1993, San Diego, CA, USA: Minerals, Metals and Materials Society.

[23] D. J. Paraventi and W. C. Moshier, "Assessment of the Interaction of Variables in the Intergranular Stress Corrosion Crack Growth Rate Behavior of Alloys 600, 82, and 182", in *13th International Conference on Environmental Degradation of Materials in Nuclear Power Systems - Water Reactors*, Whistler, BC, Canada.

[24] J. P. Berge, "Importance of surface preparation for corrosion control in nuclear power stations", *Materials Performance*, Vol.36, Iss.11, 1997, pp. 56-62.

[25] D. Deforege, L. Duisabeau, S. Miloudi, Y. Therbault, T. Couvant, F. Vaillant and E. Lemaire, "Learnings from EDF Investigation on SG Divider Plates and Vessel Head Nozzles: Evidence of Prior Deformation Effect on Stress Corrosion Cracking", in *Fontevraud 7 - Contribution of materials investigations to improve the safety and performance of LWRs*, 2011, Avignon, France: Société française d'énergie nucléaire.

[26] P. Scott, M. C. Meunier, F. Steltzlen, O. Calonne, M. Foucault, P. Combrade and C. Amzallag, "Comparison of laboratory and field experience of PWSCC in alloy 182 weld metal", in *13th International Conference on Environmental Degradation of Materials in Nuclear Power Systems - Water Reactors*, 2007, Whistler, BC, Canada: Canadian Nuclear Society, The Minerals, Metals & Materials Society.

[27] O. Raquet, D. Feron, G. Santarini and J. M. Boursier, "IGSCC of alloy 600 in PWR primary water influence of a cold worked layer on crack initiation", in *International Conference on Hydrogen Effects on Material Behaviour and Corrosion Deformation Interactions*, 2003, Moran, WY, USA.

[28] S. Le Hong, "Influence of Surface Condition on Primary Water Stress Corrosion Cracking Initiation of Alloy 600", *Corrosion*, Vol.57, Iss.4, 2001, pp. 323-333.

[29] R. A. Morris, N. Lewis and D. S. Morton, "3D Analysis of Surface Treatment Effect on the Oxidation of Grain Boundaries in Alloy 600", in *16th International Conference on Environmental Degradation of Materials in Nuclear Power Systems - Water Reactors*, 2013, Asheville, NC, USA: NACE International.

[30] F. Scenini, R. C. Newman, R. A. Cottis and R. J. Jacko, "Effect of Surface Preparation on Intergranular Stress Corrosion Cracking of Alloy 600 in Hydrogenated Steam", *Corrosion*, Vol.64, Iss.11, 2008, pp. 824-835.

[31] D. J. Paraventi and W. C. Moshier, "Alloy 690 SCC Growth Rate Testing", in *Workshop on Cold Work in Iron- and Nickel-Base Alloys*, 2007: EPRI.

[32] D. R. Tice, S. L. Medway, N. Platts and J. W. Startmand, "Crack Growth Testing on Cold Worked Alloy 690 in Primary Water Environment", in *15th International Conference on Environmental Degradation of Materials in Nuclear Power Systems - Water Reactors*, Colorado Springs, CO, USA.

[33] P. Andresen, M. M. Morra and A. Ahluwalia, "Effect of deformation temperature, orientation and carbides on SCC of Alloy 690", in *16th International Conference on Environmental Degradation of Materials in Nuclear Power Systems - Water Reactors*, 2013, Asheville, NC, USA: NACE International.

[34] R. Shen, "Review of the Effect of Cold Work on Stress Corrosion Cracking of Alloy 690", in *Materials Science and Technology - Nucelar Materials, Advanced Course*, H. Hanninen and T. Kiese, Editors. 2012, Helsinki University Press: Espoo, Finland, pp. 133-145.

[35] E. Richey, D. S. Morton and R. A. Etien, "SCC initiation testing of nickel-based alloys in high temperature water", in *13th International Conference on Environmental Degradation of Materials in Nuclear Power Systems - Water Reactors*, 2007, Whistler, BC, Canada: Canadian Nuclear Society, The Minerals, Metals & Materials Society.